UNIVERSITY OF CALIFORNIA, SAN DIEGO

Resting State Magnetoencephalography: Methods and Applications

A dissertation submitted in partial satisfaction of the requirements for the degree Doctor of Philosophy

in

Bioengineering

by

Omer Tal

Committee in charge:

Professor Thomas T. Liu, Chair
Professor Gert Cauwenberghs, Co-Chair
Professor Richard B. Buxton
Professor Todd P. Coleman
Professor Mingxiong Huang
Professor Gabriel A. Silva

2014

The Dissertation of Omer Tal is approved, and it is acceptable in quality and form for publication on microfilm and electronically:

_____

_____

_____

_____

_____
Co-Chair

_____
Chair

University of California, San Diego

2014

TABLE OF CONTENTS

LIST OF FIGURES

LIST OF TABLES

ACKNOWLEDGEMENTS

Chapter 1, in full, is a reprint of the material as it appears in Frontiers in Human Neuroscience 2013. Tal, Omer; Diwakar, Mithun; Wong, Chi-Wah; Olafsson, Valur; Lee, Ronald; Huang, Ming-Xiong; Liu, Thomas T., (2013). Caffeine-induced global reductions in resting-state BOLD connectivity reflect widespread decreases in MEG connectivity. Front. Hum. Neurosci. 7(63): 1-10. The dissertation author was the primary investigator and author of this paper.

Chapter 2, in full, is a reprint of the material as it appears in Neuroimage 2011. Diwakar, Mithun; Tal, Omer; Liu, Thomas T.; Harrington, Deborah L.; Srinivasan, Ramesh; Muzzatti, Laura; Song, Tao; Theilmann, Rebecca J.; Lee, Ronald R.; Huang, Ming-Xiong (2011). Accurate reconstruction of temporal correlation for neuronal sources using the enhanced dual-core MEG beamformer. NeuroImage 56: 1918-28. The dissertation author was a primary investigator and a co-author of this paper.

VITA

2006	Bachelor of Science, University of California, San Diego
2007-2010	Graduate Student Instructor, University of California, San Diego
2010	Master of Science, University of California, San Diego
2014	Doctor of Philosophy, University of California, San Diego

PUBLICATIONS

M. Diwakar*, O. Tal*, T.T. Liu, D.L. Harrington, R. Srinivasan, L. Muzzatti, T. Song, R.J. Theilmann, R.R. Lee, M.X. Huang. Accurate Reconstruction of Temporal Correlation for Neuronal Sources using the Enhanced Dual-Core MEG Beamformer. *Neuroimage* (56) 1918-28, June 2011.
* Dual First-Author Arrangement

C. W. Wong, V. Olafsson, O. Tal, and T.T. Liu. Anti-correlated Networks, Global Signal Regression, and the Effects of Caffeine in Resting-State Functional MRI. *Neuroimage* (63) 356-64, June 2012.

O. Tal, M. Diwakar, C. W. Wong, V. Olafsson, R.R. Lee, M.X. Huang and T.T. Liu. Caffeine-Induced Global Reductions in Resting-State BOLD Connectivity Reflect Widespread Decreases in MEG Connectivity. *Frontiers of Human Neuroscience* (7) Article #63, March 2013.

D. Heister, M. Diwakar, S. Nichols, A. Robb, A. Angeles, O. Tal, D.L. Harrington, T. Song, R.R. Lee, M.X. Huang. Resting-state neuronal oscillatory correlates of working memory performance. *PLOS One* 8(6), June 25 2013.

C. W. Wong, V. Olafsson, O. Tal, and T.T. Liu. The amplitude of resting-state fMRI global signal is related to EEG vigilance measures. *NeuroImage* (83) 983-90, Dec 2013.

FIELDS OF STUDY

Major field: Bioengineering

Studies in Functional MRI
Professor Thomas T. Liu

Studies in Magnetoencephalography
Professor Mingxiong Huang

ABSTRACT OF THE DISSERTATION

Resting State Magnetoencephalography: Methods and Applications

by

Omer Tal

Doctor of Philosophy in Bioengineering

University of California, San Diego, 2014

Professor Thomas T. Liu, Chair
Professor Gert Cauwenberghs, Co-Chair

In recent times, the study of functional connectivity (FC) between spatially distinct locations yet functionally related locations in the resting brain using functional magnetic resonance imaging (fMRI) has been on the rise. However, the interpretation of such functional measures is complicated by the complex hemodynamic nature of the blood oxygenation level dependent (BOLD) signal, which can be influenced by both neural as well as vascular factors. In this work, we employed a direct measure of

neuromagnetic activity, magnetoencephalography (MEG), to further validate the neural origin of caffeine-induced reductions in BOLD connectivity observed previously in our lab. Concerns regarding the performance of existing source reconstruction methods for MEG analysis motivated the development of an improved source reconstruction technique, a multi-core beamformer (MCBF), which was comprehensively tested with both simulations and neuromagnetic data. An iterative algorithm to be used in conjunction with the MCBF, allowing a solution to be obtained without any *a priori* knowledge about the underlying source configuration, was described and analyzed in detail. With the help of the new beamformer, the caffeine data were reexamined and the original findings were upheld. Preliminary investigation into resting-state networks by means of temporal independent component analysis (ICA) was also conducted.

INTRODUCTION

The field of resting-state functional connectivity was pioneered by Biswal et al. (1995), who was the first to employ functional magnetic resonance imaging (fMRI) to observe synchronous neurophysiological activity in the resting human brain. In particular, it was demonstrated that low frequency (<0.1 Hz) fluctuations in the blood oxygenation level-dependent (BOLD) signal were temporally correlated across spatially distinct regions (left and right motor cortices). As BOLD fluctuations are generally viewed to be reflections of underlying fluctuations in neural activity, the observed BOLD correlations between the two regions were believed to be manifestations of functional connectivity in the motor cortex at rest (Biswal et al., 1995). Later studies repeated the methodology to discover other functionally connected networks in the resting brain, such as the visual network (Lowe et al., 1998), the auditory network (Cordes et al., 2000) and the default mode network (Greicius et al., 2003; Raichle et al., 2001). Given the robust spatial consistency in networks across subjects (Beckmann et al., 2005; Damoiseaux et al., 2006), spatial independent component analysis (ICA) was applied by Smith et al. (2009) to help characterize the functional architecture of these resting-state networks (RSNs), resulting in a set of RSN maps that have become the standard reference for the resting-state connectivity community (cited over 850 times in the past 4.5 years). Advancing our knowledge of the fundamental nature and neurophysiological basis of the RSNs is essential as such fMRI studies have already helped us shed light on the brain's behavioral states (Fox et al., 2007; He et al., 2007) and development (Jolles et al., 2011), assess cognitive performance and intelligence (Hampson et al., 2006; Jolles et al., 2013; Song et

al., 2008) and better understand the neural pathology of disorders such as Alzheimer's disease (Greicius et al., 2004; Liu et al., 2013b), multiple sclerosis (Lowe et al., 2002), schizophrenia (Garrity et al., 2007), Parkinson's disease (Kwak et al., 2010; Liu et al., 2013a), epilepsy (Lui et al., 2008) and more.

Although resting-state fMRI is quickly becoming a popular approach for the study of brain function, caution must be exercised when interpreting the physiological mechanisms driving the observed connectivity results due to the BOLD signal's dependence on both vascular as well as neural factors. Resting-state neural fluctuations triggers changes in oxygen metabolism, cerebral blood volume and cerebral blood flow in a complex fashion, which collectively produce the measured hemodynamic response known as the BOLD signal (Buxton et al., 2004). Therefore, fMRI can provide only an indirect measure of the underlying neural dynamics. Furthermore, studies have repeatedly shown that non-neuronal elements (metabolic and vascular factors) can significantly affect BOLD measurements by altering the neurovascular coupling linking the neural activity and the hemodynamic response (Behzadi and Liu, 2005; Cohen et al., 2002; D'Esposito et al., 2003; Liau et al., 2008; Liu et al., 2004). This can unfortunately lead to the undesirable outcome of a false-positive assessment, where the detected BOLD signal connectivity fluctuations could be incorrectly misattributed to changes neural activity which did not actually take place (Liu, 2013). Matters could be further complicated in the scenario where the influencing factor is known to affect both the neural and the vascular systems. For example, caffeine, which stimulates neural activity via A_1 adenosine antagonism (Dunwiddie and Masino, 2001) as well as constricts the vasculature via A_2 adenosine antagonism (Fredholm et al., 1999), has been previously noted to significantly

reduce BOLD functional connectivity in the resting brain (Rack-Gomer et al., 2009; Wong et al., 2012), yet the true physiological origin of the observed reductions was not fully understood. Altogether, a better grasp of the electrophysiological basis of fMRI resting state connectivity findings would be valuable to ensure their correct interpretation.

Direct measures of neuro-electromagnetic activity could be extremely useful in elucidating fMRI observations as the hemodynamic confounds of the BOLD signal are bypassed. For example, magnetoencephalography (MEG), a non-invasive brain imaging modality, detects primarily the magnetic fields produced by the highly organized patches of post-synaptic neuronal currents in the cortical gray matter (Hamalainen et al., 1993). Such synchronized neuronal oscillations are believed to be more direct indicators of underlying cortical connectivity (Schnitzler and Gross, 2005; Singer, 1999). In addition, whereas fMRI's temporal resolution is considerably poor (>1s) due to the temporal characteristics of the hemodynamic response (Buxton et al., 2004), MEG offers data which matches the timescale of neural firing (on the order of 1ms), thereby allowing a wider, as well as more fitting, frequency range for data analysis of recorded neural activity. Although perhaps less recognized than its familiar counterpart, electroencephalography (EEG), MEG provides vastly improved spatial resolution as it is insensitive to the inhomogeneous conductivity profile of the head, includes a high number of sensors (~300), and is supported by more advanced reconstruction algorithms for source-space projection (Robinson, 1998; Sekihara, 2008; Zumer et al., 2007). Taking all these facts into consideration, MEG serves as a suitable choice for functional brain imaging studies. In fact, the use of MEG as an investigative tool for resting-state connectivity has been on the rise as of recent years, for the study of brain networks in

healthy subjects (Brookes et al., 2011a; de Pasquale et al., 2010; Hipp et al., 2012; Liu et al., 2010; Mantini et al., 2007) as well as in patients suffering from neurophysiological conditions such as autism, Alzheimer's disease, Parkinson's Disease, and stroke (Gomez et al., 2011; Schoonheim et al., 2011; Tarapore et al., 2012; Westlake et al., 2012; Zamrini et al., 2011). Several noteworthy resting-state fMRI findings were mirrored, thus helping establish their underlying electrophysiological basis, such as existence of the motor network (Brookes et al., 2011a), the default mode and attention networks (de Pasquale et al., 2010), the visual and auditory networks (Hipp et al., 2012) and other RSNs (Brookes et al., 2011b).

Typically, functional connectivity analyses of resting-state MEG recordings have estimated source time-courses and correlations utilizing adaptive spatial filters (beamformers) as their source-space projection tool of choice (Brookes et al., 2011a; Brookes et al., 2011b; Hall et al., 2013; Hillebrand et al., 2012; Hipp et al., 2012; Luckhoo et al., 2012; Mantini et al., 2011). Although most commonly used, the reconstructions using the conventional minimum-variance beamformer (Robinson, 1998; Sekihara et al., 2002; Van Drongelen, 1996; Van Veen et al., 1997) are highly susceptible to inter-source correlations, resulting in source amplitude suppression and time-course distortion (Sekihara, 2008). Considering that spontaneous neural activity is known to involve synchronous communication between multiple sources (Singer, 1999), the use of the conventional beamformer as a tool for FC analysis could be problematic (Moiseev and Herdman, 2013). Moreover, spurious connectivity introduced due to the ill-posed nature of the inverse (source-space projection) problem known as signal leakage, is thought to be a significant hindrance in assessing MEG functional connectivity and RSN

characterization (Brookes et al., 2011b; Brookes et al., 2012), further raising the question of the current practice.

The purpose of this dissertation is to further validate previous fMRI resting-state findings by probing the corresponding MEG connectivity observations as well as to help advance existing MEG source-space projection techniques to better suit the question at hand. In the first study, we examined and compared the effects of a pharmacological agent (caffeine) on fMRI and MEG resting-state global connectivity across a sample of 10 subjects (standard beamformer used for MEG source-space projection). We found that caffeine led to a significant and widespread reduction in both fMRI and MEG measures, suggesting that changes in neural connectivity played a substantial role in decreasing the BOLD connectivity. In our second study, we developed and tested a mathematical framework for an improved version of the conventional beamformer, which is insensitive to inter-source correlations. Simulations and real evoked neuromagnetic data were used to confirm theory. In our third study, we developed and tested an algorithm to help automate MEG resting-state data processing with the enhanced beamformer, helping to eliminate the concerns of signal leakage and the requirement of *a priori* knowledge of source location. Once more, complex simulations along with real evoked neuromagnetic measurements were used to confirm the potential of the proposed technique. In the final section, we compare the original and new beamformers by re-examining both the caffeine data as well as MEG resting-state networks in general. We demonstrate that although the different reconstructions methods exhibited significant differences when investigated with simulations and evoked data, the difference between methods were not significant when applied to resting-state measurements.

References

Beckmann, C.F., DeLuca, M., Devlin, J.T., Smith, S.M., 2005. Investigations into resting-state connectivity using independent component analysis. Philos Trans R Soc Lond B Biol Sci 360, 1001-1013.

Behzadi, Y., Liu, T.T., 2005. An arteriolar compliance model of the cerebral blood flow response to neural stimulus. Neuroimage 25, 1100-1111.

Biswal, B., Yetkin, F.Z., Haughton, V.M., Hyde, J.S., 1995. Functional connectivity in the motor cortex of resting human brain using echo-planar MRI. Magn Reson Med 34, 537-541.

Brookes, M.J., Hale, J.R., Zumer, J.M., Stevenson, C.M., Francis, S.T., Barnes, G.R., Owen, J.P., Morris, P.G., Nagarajan, S.S., 2011a. Measuring functional connectivity using MEG: methodology and comparison with fcMRI. Neuroimage 56, 1082-1104.

Brookes, M.J., Woolrich, M., Luckhoo, H., Price, D., Hale, J.R., Stephenson, M.C., Barnes, G.R., Smith, S.M., Morris, P.G., 2011b. Investigating the electrophysiological basis of resting state networks using magnetoencephalography. Proc Natl Acad Sci U S A 108, 16783-16788.

Brookes, M.J., Woolrich, M.W., Barnes, G.R., 2012. Measuring functional connectivity in MEG: a multivariate approach insensitive to linear source leakage. Neuroimage 63, 910-920.

Buxton, R.B., Uludag, K., Dubowitz, D.J., Liu, T.T., 2004. Modeling the hemodynamic response to brain activation. Neuroimage 23 Suppl 1, S220-233.

Cohen, E.R., Ugurbil, K., Kim, S.G., 2002. Effect of basal conditions on the magnitude and dynamics of the blood oxygenation level-dependent fMRI response. J Cereb Blood Flow Metab 22, 1042-1053.

Cordes, D., Haughton, V.M., Arfanakis, K., Wendt, G.J., Turski, P.A., Moritz, C.H., Quigley, M.A., Meyerand, M.E., 2000. Mapping functionally related regions of brain with functional connectivity MR imaging. AJNR Am J Neuroradiol 21, 1636-1644.

D'Esposito, M., Deouell, L.Y., Gazzaley, A., 2003. Alterations in the BOLD fMRI signal with ageing and disease: a challenge for neuroimaging. Nat Rev Neurosci 4, 863-872.

Damoiseaux, J.S., Rombouts, S.A., Barkhof, F., Scheltens, P., Stam, C.J., Smith, S.M., Beckmann, C.F., 2006. Consistent resting-state networks across healthy subjects. Proc Natl Acad Sci U S A 103, 13848-13853.

de Pasquale, F., Della Penna, S., Snyder, A.Z., Lewis, C., Mantini, D., Marzetti, L., Belardinelli, P., Ciancetta, L., Pizzella, V., Romani, G.L., Corbetta, M., 2010. Temporal

dynamics of spontaneous MEG activity in brain networks. Proc Natl Acad Sci U S A 107, 6040-6045.

Dunwiddie, T.V., Masino, S.A., 2001. The role and regulation of adenosine in the central nervous system. Annu Rev Neurosci 24, 31-55.

Fox, M.D., Snyder, A.Z., Vincent, J.L., Raichle, M.E., 2007. Intrinsic fluctuations within cortical systems account for intertrial variability in human behavior. Neuron 56, 171-184.

Fredholm, B.B., Battig, K., Holmen, J., Nehlig, A., Zvartau, E.E., 1999. Actions of caffeine in the brain with special reference to factors that contribute to its widespread use. Pharmacol Rev 51, 83-133.

Garrity, A.G., Pearlson, G.D., McKiernan, K., Lloyd, D., Kiehl, K.A., Calhoun, V.D., 2007. Aberrant "default mode" functional connectivity in schizophrenia. Am J Psychiatry 164, 450-457.

Gomez, C., Olde Dubbelink, K.T., Stam, C.J., Abasolo, D., Berendse, H.W., Hornero, R., 2011. Complexity analysis of resting-state MEG activity in early-stage Parkinson's disease patients. Ann Biomed Eng 39, 2935-2944.

Greicius, M.D., Krasnow, B., Reiss, A.L., Menon, V., 2003. Functional connectivity in the resting brain: a network analysis of the default mode hypothesis. Proc Natl Acad Sci U S A 100, 253-258.

Greicius, M.D., Srivastava, G., Reiss, A.L., Menon, V., 2004. Default-mode network activity distinguishes Alzheimer's disease from healthy aging: evidence from functional MRI. Proc Natl Acad Sci U S A 101, 4637-4642.

Hall, E.L., Woolrich, M.W., Thomaz, C.E., Morris, P.G., Brookes, M.J., 2013. Using variance information in magnetoencephalography measures of functional connectivity. Neuroimage 67, 203-212.

Hamalainen, M., Hari, R., Ilmoniemi, R.J., Knuutila, J., Lounasmaa, O.V., 1993. Magnetoencephalography - Theory, Instrumentation, and Applications to Noninvasive Studies of the Working Human Brain. Reviews of Modern Physics 65, 413-497.

Hampson, M., Driesen, N.R., Skudlarski, P., Gore, J.C., Constable, R.T., 2006. Brain connectivity related to working memory performance. J Neurosci 26, 13338-13343.

He, B.J., Snyder, A.Z., Vincent, J.L., Epstein, A., Shulman, G.L., Corbetta, M., 2007. Breakdown of functional connectivity in frontoparietal networks underlies behavioral deficits in spatial neglect. Neuron 53, 905-918.

Hillebrand, A., Barnes, G.R., Bosboom, J.L., Berendse, H.W., Stam, C.J., 2012. Frequency-dependent functional connectivity within resting-state networks: an atlas-based MEG beamformer solution. Neuroimage 59, 3909-3921.

Hipp, J.F., Hawellek, D.J., Corbetta, M., Siegel, M., Engel, A.K., 2012. Large-scale cortical correlation structure of spontaneous oscillatory activity. Nat Neurosci 15, 884-890.

Jolles, D.D., van Buchem, M.A., Crone, E.A., Rombouts, S.A., 2011. A comprehensive study of whole-brain functional connectivity in children and young adults. Cereb Cortex 21, 385-391.

Jolles, D.D., van Buchem, M.A., Crone, E.A., Rombouts, S.A., 2013. Functional brain connectivity at rest changes after working memory training. Hum Brain Mapp 34, 396-406.

Kwak, Y., Peltier, S., Bohnen, N.I., Muller, M.L., Dayalu, P., Seidler, R.D., 2010. Altered resting state cortico-striatal connectivity in mild to moderate stage Parkinson's disease. Front Syst Neurosci 4, 143.

Liau, J., Perthen, J.E., Liu, T.T., 2008. Caffeine reduces the activation extent and contrast-to-noise ratio of the functional cerebral blood flow response but not the BOLD response. Neuroimage 42, 296-305.

Liu, H., Edmiston, E.K., Fan, G., Xu, K., Zhao, B., Shang, X., Wang, F., 2013a. Altered resting-state functional connectivity of the dentate nucleus in Parkinson's disease. Psychiatry Res 211, 64-71.

Liu, T.T., 2013. Neurovascular factors in resting-state functional MRI. Neuroimage 80, 339-348.

Liu, T.T., Behzadi, Y., Restom, K., Uludag, K., Lu, K., Buracas, G.T., Dubowitz, D.J., Buxton, R.B., 2004. Caffeine alters the temporal dynamics of the visual BOLD response. Neuroimage 23, 1402-1413.

Liu, Y., Yu, C., Zhang, X., Liu, J., Duan, Y., Alexander-Bloch, A.F., Liu, B., Jiang, T., Bullmore, E., 2013b. Impaired Long Distance Functional Connectivity and Weighted Network Architecture in Alzheimer's Disease. Cereb Cortex.

Liu, Z., Fukunaga, M., de Zwart, J.A., Duyn, J.H., 2010. Large-scale spontaneous fluctuations and correlations in brain electrical activity observed with magnetoencephalography. Neuroimage 51, 102-111.

Lowe, M.J., Mock, B.J., Sorenson, J.A., 1998. Functional connectivity in single and multislice echoplanar imaging using resting-state fluctuations. Neuroimage 7, 119-132.

Lowe, M.J., Phillips, M.D., Lurito, J.T., Mattson, D., Dzemidzic, M., Mathews, V.P., 2002. Multiple sclerosis: low-frequency temporal blood oxygen level-dependent fluctuations indicate reduced functional connectivity initial results. Radiology 224, 184-192.

Luckhoo, H., Hale, J.R., Stokes, M.G., Nobre, A.C., Morris, P.G., Brookes, M.J., Woolrich, M.W., 2012. Inferring task-related networks using independent component analysis in magnetoencephalography. Neuroimage 62, 530-541.

Lui, S., Ouyang, L., Chen, Q., Huang, X., Tang, H., Chen, H., Zhou, D., Kemp, G.J., Gong, Q., 2008. Differential interictal activity of the precuneus/posterior cingulate cortex revealed by resting state functional MRI at 3T in generalized vs. partial seizure. J Magn Reson Imaging 27, 1214-1220.

Mantini, D., Della Penna, S., Marzetti, L., de Pasquale, F., Pizzella, V., Corbetta, M., Romani, G.L., 2011. A signal-processing pipeline for magnetoencephalography resting-state networks. Brain Connect 1, 49-59.

Mantini, D., Perrucci, M.G., Del Gratta, C., Romani, G.L., Corbetta, M., 2007. Electrophysiological signatures of resting state networks in the human brain. Proc Natl Acad Sci U S A 104, 13170-13175.

Moiseev, A., Herdman, A.T., 2013. Multi-core beamformers: derivation, limitations and improvements. Neuroimage 71, 135-146.

Rack-Gomer, A.L., Liau, J., Liu, T.T., 2009. Caffeine reduces resting-state BOLD functional connectivity in the motor cortex. Neuroimage 46, 56-63.

Raichle, M.E., MacLeod, A.M., Snyder, A.Z., Powers, W.J., Gusnard, D.A., Shulman, G.L., 2001. A default mode of brain function. Proc Natl Acad Sci U S A 98, 676-682.

Robinson, S., Vrba, J., 1998. Functional neuroimaging by synthetic aperture magnetometry. Tohoku Univ. Press, Sendai.

Schnitzler, A., Gross, J., 2005. Functional connectivity analysis in magnetoencephalography. Int Rev Neurobiol 68, 173-195.

Schoonheim, M.M., Geurts, J.J., Landi, D., Douw, L., van der Meer, M.L., Vrenken, H., Polman, C.H., Barkhof, F., Stam, C.J., 2011. Functional connectivity changes in multiple sclerosis patients: A graph analytical study of MEG resting state data. Hum Brain Mapp.

Sekihara, K., Nagarajan, S.S., Poeppel, D., Marantz, A., 2002. Performance of an MEG adaptive-beamformer technique in the presence of correlated neural activities: effects on signal intensity and time-course estimates. IEEE Trans Biomed Eng 49, 1534-1546.

Sekihara, K., Nagarajan, S.S., 2008. Adaptive Spatial Filters for Electormagnetic Brain Imaging. SpringerLink, Berlin.

Singer, W., 1999. Neuronal synchrony: a versatile code for the definition of relations? Neuron 24, 49-65, 111-125.

Smith, S.M., Fox, P.T., Miller, K.L., Glahn, D.C., Fox, P.M., Mackay, C.E., Filippini, N., Watkins, K.E., Toro, R., Laird, A.R., Beckmann, C.F., 2009. Correspondence of the brain's functional architecture during activation and rest. Proc Natl Acad Sci U S A 106, 13040-13045.

Song, M., Zhou, Y., Li, J., Liu, Y., Tian, L., Yu, C., Jiang, T., 2008. Brain spontaneous functional connectivity and intelligence. Neuroimage 41, 1168-1176.

Tarapore, P.E., Martino, J., Guggisberg, A.G., Owen, J., Honma, S.M., Findlay, A., Berger, M.S., Kirsch, H.E., Nagarajan, S.S., 2012. Magnetoencephalographic Imaging of Resting-State Functional Connectivity Predicts Postsurgical Neurological Outcome in Brain Gliomas. Neurosurgery 71, 1012-1022.

Van Drongelen, W., Yuchtman, M., Van Veen, B.D., Van Huffelen, A.C., 1996. A spatial filtering technique to detect and localize multiple sources in the brain. Brain Topogr 9, 39-49.

Van Veen, B.D., van Drongelen, W., Yuchtman, M., Suzuki, A., 1997. Localization of brain electrical activity via linearly constrained minimum variance spatial filtering. IEEE Trans Biomed Eng 44, 867-880.

Westlake, K.P., Hinkley, L.B., Bucci, M., Guggisberg, A.G., Findlay, A.M., Henry, R.G., Nagarajan, S.S., Byl, N., 2012. Resting state alpha-band functional connectivity and recovery after stroke. Exp Neurol 237, 160-169.

Wong, C.W., Olafsson, V., Tal, O., Liu, T.T., 2012. Anti-correlated networks, global signal regression, and the effects of caffeine in resting-state functional MRI. Neuroimage 63, 356-364.

Zamrini, E., Maestu, F., Pekkonen, E., Funke, M., Makela, J., Riley, M., Bajo, R., Sudre, G., Fernandez, A., Castellanos, N., Del Pozo, F., Stam, C.J., van Dijk, B.W., Bagic, A., Becker, J.T., 2011. Magnetoencephalography as a putative biomarker for Alzheimer's disease. Int J Alzheimers Dis 2011, 280289.

Zumer, J.M., Attias, H.T., Sekihara, K., Nagarajan, S.S., 2007. A probabilistic algorithm integrating source localization and noise suppression for MEG and EEG data. Neuroimage 37, 102-115.

CHAPTER 1

frontiers in
HUMAN NEUROSCIENCE

ORIGINAL RESEARCH ARTICLE
published: 04 March 2013
doi: 10.3389/fnhum.2013.00063

Caffeine-induced global reductions in resting-state BOLD connectivity reflect widespread decreases in MEG connectivity

Omer Tal[1,2]*, Mithun Diwakar[2,3], Chi-Wah Wong[1,3], Valur Olafsson[1,3], Roland Lee[3], Ming-Xiong Huang[3,4] and Thomas T. Liu[1,2,3]*

[1] Center for Functional MRI, University of California San Diego, La Jolla, CA, USA
[2] Department of Bioengineering, University of California San Diego, La Jolla, CA, USA
[3] Department of Radiology, University of California San Diego, La Jolla, CA, USA
[4] Research and Radiology Services, VA San Diego Healthcare System, San Diego, CA, USA

Edited by:
Matthew J. Brookes, University of Nottingham, UK

Reviewed by:
Stephen E. Robinson, National Institutes of Health, USA
Joanne Hale, University of Birmingham, UK

***Correspondence:**
Omer Tal and Thomas T. Liu, Center for Functional MRI, University of California San Diego, 9500 Gilman Drive, #0677, La Jolla, CA 92093, USA.
e-mail: otal@ucsd.edu; ttliu@ucsd.edu

In resting-state functional magnetic resonance imaging (fMRI), the temporal correlation between spontaneous fluctuations of the blood oxygenation level dependent (BOLD) signal from different brain regions is used to assess functional connectivity. However, because the BOLD signal is an indirect measure of neuronal activity, its complex hemodynamic nature can complicate the interpretation of differences in connectivity that are observed across conditions or subjects. For example, prior studies have shown that caffeine leads to widespread reductions in BOLD connectivity but were not able to determine if neural or vascular factors were primarily responsible for the observed decrease. In this study, we used source-localized magnetoencephalography (MEG) in conjunction with fMRI to further examine the origins of the caffeine-induced changes in BOLD connectivity. We observed widespread and significant ($p < 0.01$) reductions in both MEG and fMRI connectivity measures, suggesting that decreases in the connectivity of resting-state neuro-electric power fluctuations were primarily responsible for the observed BOLD connectivity changes. The MEG connectivity decreases were most pronounced in the beta band. By demonstrating the similarity in MEG and fMRI based connectivity changes, these results provide evidence for the neural basis of resting-state fMRI networks and further support the potential of MEG as a tool to characterize resting-state connectivity.

Keywords: magnetoencephalography, fMRI, BOLD, resting-state, functional connectivity, caffeine

INTRODUCTION

The temporal correlation between spontaneous low-frequency fluctuations in the blood oxygenation level dependent (BOLD) signal measured using functional magnetic resonance imaging (fMRI) is being increasingly used to characterize functional connectivity (FC) in the brain. Functional connectivity MRI (fcMRI) was first demonstrated by Biswal et al. (1995), who observed synchronous BOLD fluctuations within the motor cortex during rest. Subsequent studies found additional resting-state networks such as the visual network (Lowe et al., 1998), the default mode network (Raichle et al., 2001), the task positive network (Fox et al., 2005), and a number of task-related networks (Smith et al., 2009). fcMRI studies are advancing our understanding of the brain's behavioral states (Fox et al., 2007; He et al., 2007) and pathology (Lowe et al., 2002; Greicius et al., 2004; Lui et al., 2008; Kwak et al., 2010), and have also proven to be useful for the assessment of cognitive performance (Hampson et al., 2006; Song et al., 2008a).

In most fcMRI studies, changes in FC measures are interpreted as evidence of underlying changes in neuronal connectivity. However, as the BOLD signal reflects both vascular and neural factors, the interpretation of resting-state FC observations can be challenging. The BOLD response is a complex function (known as the hemodynamic response) of changes in oxygen metabolism ($CMRO_2$), cerebral blood flow (CBF) and blood volume, and thus provides an indirect measure of the underlying neuro-electrical activity (Buxton et al., 2004). Other non-neuronal confounds, such as metabolic and vascular factors rising from differences in age, diet, medications, and pathology, can alter the neurovascular coupling linking neural activity to the observed hemodynamic changes (Cohen et al., 2002; D'Esposito et al., 2003; Liu et al., 2004; Behzadi and Liu, 2005; Liau et al., 2008) and thus affect the BOLD signal. Hence, changes in metabolic and vascular factors can give rise to changes in FC measures even when there is no underlying change in neural connectivity.

Magnetoencephalography (MEG) is a non-invasive brain imaging modality which can aid in the interpretation of fcMRI measures (Hamalainen et al., 1993). MEG avoids the hemodynamic confounds of the BOLD signal by providing a direct measure of neuro-electromagnetic activity. Furthermore, the temporal resolution of the MEG signal is on the timescale of neural firing events, permitting a substantially wider frequency range for activity analysis than the fMRI signal, whose temporal resolution is limited by the temporal broadening inherent in the hemodynamic

response (Buxton et al., 2004). Compared to electroencephalography (EEG), MEG provides superior spatial resolution, due in large part to its robustness to the conductivity profile of the human head. In addition, the high number of sensors and availability of advanced reconstruction algorithms (Robinson and Vrba, 1998; Wipf et al., 2010) have enabled more accurate characterization of the underlying neuro-electromagnetic sources. In recent years, MEG has emerged as a valuable tool in the investigation of connectivity and power fluctuations in both studies of healthy volunteers (de Pasquale et al., 2010; Liu et al., 2010; Brookes et al., 2011a; Mantini et al., 2011) and patients suffering from neurophysiological disorders such as autism, Alzheimer's disease, Parkinson's disease, and stroke (Gomez et al., 2011; Schoonheim et al., 2011; Zamrini et al., 2011; Tarapore et al., 2012a,b; Westlake et al., 2012). Perhaps most notably, Brookes et al. (2011b) recently used MEG and beamforming algorithms to validate the electrophysiological basis of the resting-state fcMRI networks.

In order to compare changes in fMRI and MEG FC, it is useful to have a pharmacological agent that can alter the state of connectivity in healthy subjects for a period of time (e.g., an hour or more) that is sufficiently long to facilitate experimental measurements. Caffeine is a widely used stimulant that reliably perturbs the neural and vascular systems of the brain for several hours or more (Fredholm et al., 1999). We have previously shown that a 200-mg dose of caffeine significantly reduced resting-state BOLD connectivity in the motor cortex (Rack-Gomer et al., 2009) as well as in a global fashion across the brain (Wong et al., 2012). Caffeine constricts the vascular system and decreases CBF by antagonizing adenosine A_2 receptors (Fredholm et al., 1999) and stimulates the neural system through antagonism of adenosine A_1 receptors (Dunwiddie and Masino, 2001). Both pathways can alter the measured BOLD signal, where the vascular pathway does so by modifying the mechanisms of neurovascular coupling and thus the overall hemodynamic response function, while the neural pathway can modulate the input to the response function. It has been demonstrated that caffeine significantly reduces baseline CBF (Liau et al., 2008; Rack-Gomer et al., 2009) and increases baseline $CMRO_2$ (Griffeth et al., 2011), a combination which tends to increase the BOLD response to an arbitrary neural input. On the other hand, it has also been shown that caffeine tightens the coupling between CBF and $CMRO_2$, reducing the BOLD sensitivity to neural activity (Chen and Parrish, 2009; Griffeth et al., 2011). These two effects tend to cancel out, resulting in little or no impact on the task-related BOLD response (Laurienti et al., 2002; Liau et al., 2008; Chen and Parrish, 2009; Griffeth et al., 2011). As task-related and resting-state BOLD responses are likely to share the same underlying hemodynamic pathways, it is unlikely that vascular and metabolic changes are the primary mechanisms behind the observed reductions in BOLD connectivity. With regards to caffeine's effect on neural activity, several studies find that caffeine reduces EEG power (Dimpfel et al., 1993; Siepmann and Kirch, 2002) and may also decrease inter-hemispheric coherence (Reeves et al., 2002). Based on these prior findings, we hypothesized that the caffeine-induced reductions in BOLD connectivity are mainly driven by decreases in neural connectivity, and that MEG measures of FC would show a similar caffeine-related decrease. To test our hypothesis, we conducted a double-blind placebo-controlled study with a repeated measures design in which MEG and fMRI resting-state data were collected on subjects both prior to and after the ingestion of caffeine (or placebo). At present, there is not a clear consensus among resting-state FC studies with respect to the state of the eyes during the experiment, with some studies employing an eyes closed (EC) protocol while others use an eyes open (EO) with fixation protocol (Liu et al., 2010; Van Dijk et al., 2010). In light of this situation, we chose to compare the effects of caffeine on fMRI and MEG connectivity in both states.

MATERIALS AND METHODS

EXPERIMENTAL PROTOCOL

Twelve healthy volunteers were initially enrolled in this study after providing informed consent. Two subjects were not able to complete the study due to excessive motion and dental artifacts, resulting in a final sample size of 10 subjects (four males and six females; ages 21–33 years; mean of 25.6 years). To minimize potential confounds due to differing levels of caffeine consumption (Jones et al., 2000; Reeves et al., 2002), we recruited subjects with low levels of caffeine usage (<50 mg/day). Participants were instructed to abstain from caffeine for 24 h prior to being scanned, as well as to maintain low caffeine consumption for a 2-month period prior to the beginning of the study and throughout the entire duration of the study.

The study employed a double-blind, placebo-controlled, repeated measures design. For each modality (MEG and fMRI), each subject participated in two independent imaging sessions, a control session and a caffeine session, where the order of the two sessions was random. Each of the four imaging sessions (MEG control and caffeine; fMRI control and caffeine) was separated from the other sessions by at least 2 weeks. Half the subjects started with MEG sessions while the other half started with fMRI sessions. Each session consisted of a pre-dose section and a post-dose section, with each MEG and fMRI section lasting about 30 and 60 min, respectively. After the pre-dose section, subjects were taken out of the MEG or MRI scanner and asked to ingest a capsule containing 200 mg of caffeine or placebo. A 40-min period was allotted between capsule ingestion and the first functional scan of the post-dose section, as previous studies have shown that the absorption of caffeine from the gastrointestinal tract reaches 99% about 45 min post ingestion (Fredholm et al., 1999).

Each MEG scan section consisted of four 5 min resting-state scans, two with EC and two with EO, in the following order: EC, EO, EC, and EO. Subjects were instructed to stay awake, relax, and think of nothing in particular (Stamatakis et al., 2010; van den Heuvel and Hulshoff Pol, 2010) while keeping their hands open, laying flat. During EO resting-state scans, participants were asked to visually fixate on a black cross placed on a white screen, while during the EC resting-state scans they were asked to keep their eyes closed and to imagine the black cross. Each fMRI scan section included a high-resolution anatomical scan, two 5 min resting-state scans, one EO scan and one EC scan, and additional scans described below and in Wong et al. (2012). The instructions given to the subjects for the resting-state scans were the same as those used for the MEG sessions. The order of the EC and EO fMRI resting-state scans was randomized.

DATA ACQUISITION

Magnetoencephalography

Magnetoencephalography data were measured using an Elekta/Neuromag™ whole-head MEG system with 204 gradiometers and 102 magnetometers in a magnetically shielded room (IMEDCO-AG, Switzerland). Electro-oculogram (EOG) electrodes were used to record eye blinks and movements. Data were sampled at 1000 Hz and pre-processed using MaxFilter (Neuromag™) to detect and correct for saturated and spurious channels, suppress magnetic interference from inside and outside the sensor array, and compensate for disturbances due to magnetic material in the region of the head (Taulu et al., 2004; Taulu and Simola, 2006; Song et al., 2008b, 2009). As MaxFilter is limited in certain artifact-removal tasks (e.g., eye movement), we also applied temporal independent components analysis (ICA) to the data using the fast ICA algorithm (Hyvarinen, 1999) to remove notable residual artifacts due to eye movements, eye blinks, and cardiac activity. The independent components to be removed were selected by visual inspection of their temporal and spatial signatures (e.g., the EOG time-course was used for visual comparison), typically removing one to three components in a given dataset.

Functional magnetic resonance imaging

A detailed description of the acquisition and analysis of the fMRI data was previously provided in Wong et al. (2012). For convenience, we restate the relevant details in this and subsequent sections. Imaging data were acquired using a 3-T GE Discovery MR750 whole body system with an eight-channel receiver coil. High-resolution anatomical data were collected using a magnetization prepared 3D fast spoiled gradient (FSPGR) sequence (TI = 600 ms, TE = 3.1 ms, FOV = 25.6 cm, $256 \times 256 \times 176$ matrix, slice thickness = 1 mm, and flip angle = 8°). Whole brain BOLD resting-state data were acquired using an echo planar imaging (EPI) sequence (TR = 1.8 s, TE = 30 ms, FOV = 24 cm, 64×64 matrix, slice thickness = 4 mm, slice gap = 1 mm, # of slices = 30, and flip angle = 70°). Field maps were acquired using a gradient recalled acquisition in steady state (GRASS) sequence ($TE_1 = 6.5$ ms, $TE_2 = 8.5$ ms), with equivalent in-plane parameters and slice coverage as in the BOLD data, and the phase difference between the two echoes was used to correct the BOLD data for magnetic field inhomogeneities (Jenkinson, 2003; Fessler et al., 2005). Cardiac pulse and respiratory data were monitored using a pulse oximeter (InVivo Corp.) which was placed on the subject's finger and a respiratory effort transducer (BIOPAC) placed around the abdomen. The physiological data were sampled at 40 Hz using a multi-channel data acquisition board (National Instruments).

DATA PROCESSING

Magnetoencephalography

Using the high-resolution anatomical data obtained in the MRI scan, a boundary element based triangular mesh of 5-mm mesh size was generated for each subject from their inner-skull surface. FreeSurfer was used to define a fixed source grid (7 mm spacing) on the brain's gray–white matter boundary, which was then divided into cortical regions of interest (ROI) using the FreeSurfer computed parcellations (Desikan et al., 2006). With the inner-skull triangular mesh and gray matter source grid, the MEG forward model calculation for the lead-field (gain) matrix was performed using a boundary element model (Mosher et al., 1999; Huang et al., 2007). Registration of MRI and MEG data was performed using positioning information obtained with a Polhemus Isotrak system prior to each MEG session.

In our analysis, we considered MEG data both within a wide-band range of 1–50 Hz and within the following bands: delta (δ) – 1–4 Hz, theta (θ) – 4–8 Hz, alpha (α) – 8–13 Hz, low and high beta (β) – 13–20 and 20–30 Hz, respectively, and low gamma (γ) – 30–50 Hz. The frequency filtered MEG data were then projected into source space using the array-gain constraint minimum-variance regularized vector beamformer (van Drongelen et al., 1996; Van Veen et al., 1997; Robinson and Vrba, 1998; Sekihara and Nagarajan, 2008), yielding a set of band-limited time-courses for each source location. Covariance matrices were generated independently for each frequency band and experimental run using all 300 s of the recorded data from each run. The regularization level was set uniquely for each individual MEG recording by utilizing a modified "broken-stick" model as described in Behzadi et al. (2007), which helps to identify the meaningful (data-related) principal components. A statistical distribution of expected eigenvalues, derived from random normally distributed data with rank and Frobenius norm equal to that of the MEG data of interest, was used for comparison and determination of the noise level [i.e., the number of significant ($p < 0.05$) modes]. The value of the first non-significant (noise) component then represented the cut-off and was used as the regularization parameter. For each frequency band of interest, the source time-courses were Hilbert transformed to construct the corresponding analytic signals. The envelope of oscillatory power fluctuations (also referred to as the "Hilbert envelope") was obtained via computation of the amplitude of the analytic signal (Brookes et al., 2004, 2012a). Temporal smoothing was applied following the approach of Brookes et al. (2011a) where an "average Hilbert envelope" time-course was obtained by dividing the envelope time-course into 500 ms blocks and averaging the envelope within each block. These average Hilbert envelope time-courses were then used for the connectivity computations described below, yielding the Correlation of Average Envelopes as defined in Brookes et al. (2011a).

Functional magnetic resonance imaging

Anatomical data were skull-stripped and segmented into white matter, gray matter, and cerebral spinal fluid using FSL (Smith et al., 2004). The post-dose anatomical volume was registered to the pre-dose volume using AFNI (Cox, 1996), and the resulting rotation and shift parameters were applied to the post-dose functional data. A binary brain mask was created using the skull-stripped anatomical data. For each slice, the mask was eroded by two voxels along the border to eliminate voxels at the edge of the brain (Rack-Gomer and Liu, 2012). The first six time points of fMRI data were discarded to allow magnetization to reach steady state. Nuisance terms were removed from fMRI data by means of multiple linear regression using the following regressors: linear and quadratic trends, six motion parameters, RETROICOR (Glover et al., 2000) and RVHRCOR (Chang and Glover, 2009) regressors, and the mean BOLD signal calculated from WM and CSF voxels (partial volume threshold of 0.99 for each tissue type).

BOLD data were then low pass filtered with a cut-off frequency of 0.08 Hz (Biswal et al., 1997; Cordes et al., 2001; Fox et al., 2005).

CONNECTIVITY MEASURES

For each subject, we used the FreeSurfer cortical parcellations (Desikan et al., 2006) to define anatomical ROIs. As described in Wong et al. (2012), we discarded ROIs for which any subject had less than five voxels within a region, resulting in a total of 40 ROIs (20 per hemisphere). For fMRI data, an average BOLD time-course was calculated for each ROI using all voxels within the region. To reduce spatial leakage effects on the ROI-to-ROI MEG connectivity estimates that are inherent to the beamforming process (Brookes et al., 2012b), we defined a smaller MEG source region within each larger anatomical ROI. A central source for each of the cortical ROIs was defined as the source with the smallest mean path length to all the other sources within the ROI. Next, a sphere-shaped region was defined to include every source that was both within 12 mm of the central source and contained within the same ROI. The average Hilbert envelopes within this region were then averaged to provide a mean MEG time-course for each ROI.

To assess connectivity, we computed the Pearson correlation coefficient (r) between the average time-courses for each pair of ROIs (780 pairs). For each modality, the correlation coefficient was computed for each of the four acquisition sections (pre-dose and post-dose sections of both the Control and Caffeine sessions). For the MEG data, the correlation coefficients from repeated scans (e.g., the two pre-dose EC scans) were averaged. For quantitative assessments, the Pearson correlation scores were converted to the Fisher z-scores using the Fisher transformation (Luckhoo et al., 2012). The change in the z-score metric (Δz = post-dose z-score minus pre-dose z-score) in each session (caffeine and control) was calculated, and a repeated measures two-way analysis of variance (ANOVA) (Keppel and Wickens, 2004) was then used to examine the effects of two factors on the measured connectivity: (1) the effect of caffeine/control and (2) the effect of ROI pair (Wong et al., 2012).

RESULTS

WHOLE BRAIN CONNECTIVITY

For a representative subject, Pearson correlation coefficient matrices indicating the degree of connectivity in the EC condition for all ROI pairs are displayed in **Figure 1** for each of the four scan sections (pre-dose and post-dose sections of the caffeine and control sessions). The MEG and fMRI connectivity matrices are shown in the left and the right hand sides of the figure, respectively, and the fMRI matrices are similar to those previously presented in Wong et al. (2012). The MEG connectivity metrics were obtained using the wide-band frequency range (1–50 Hz). MEG correlations in the post-dose caffeine data are visibly lower than in the pre-dose caffeine data, indicating a caffeine-induced global decrease in this subject's connectivity, while there is not a widespread difference between the pre-dose and post-dose MEG correlations in the control session. A similar qualitative assessment can be made about the fMRI data, where the connectivity in the post-dose section of the caffeine session shows a widespread decrease as compared to the pre-dose condition.

Figure 2 shows the changes in z-score (post-dose minus pre-dose) averaged across subjects for both conditions (EC and EO) and sessions (control and caffeine), with the changes for MEG and fMRI shown in the left and the right hand sides of the figure, respectively. The upper triangle of each matrix shows the mean changes in the z-score metric (across subjects) for all ROI pairs, while the lower triangle shows the t-statistics of those ROI pairs

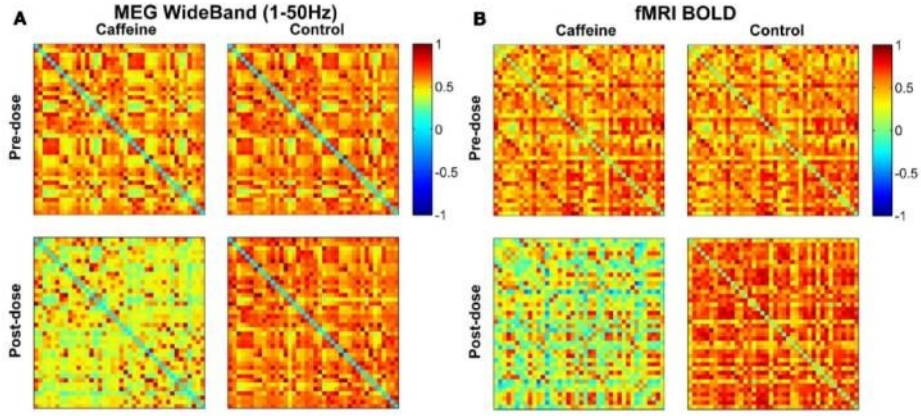

FIGURE 1 | Connectivity matrices for a representative subject in the eyes closed condition showing Pearson correlations between all pairs of ROIs for the (A) MEG wide-band (1–50 Hz) data and the (B) fMRI BOLD data. Each entry corresponds to the correlation between one pair of ROIs, with the axes corresponding to the ROI indices (1–40). Both MEG and fMRI connectivity are visibly lower in the post-dose caffeine section than in the pre-dose caffeine section, while no change is apparent in the control session for either modality. ROI labels (1–20 left hemisphere; 21–40 right hemisphere): anterior cingulate, middle frontal, cuneus, fusiform, inferior parietal, isthmus cingulate, lateral orbitofrontal, medial orbitofrontal, pars opercularis, post central, posterior cingulate, precentral, precuneus, rostral anterior cingulate, rostral middle frontal, superior frontal, superior parietal, superior temporal, supramarginal, insula.

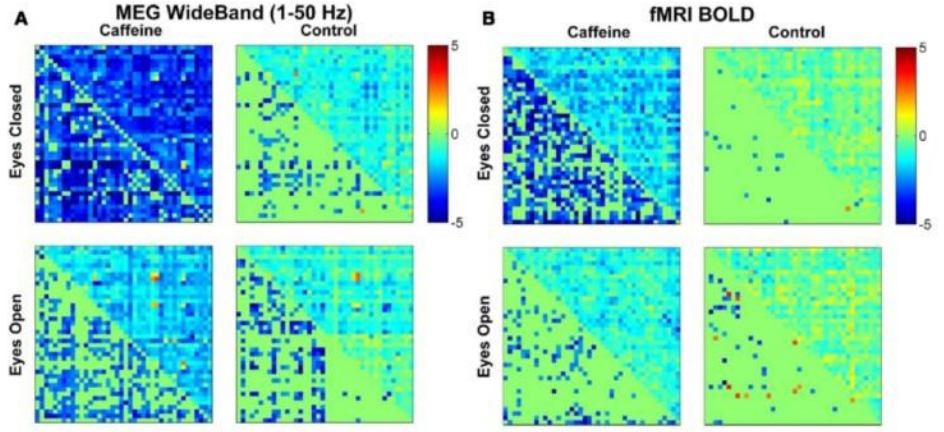

FIGURE 2 | Changes in mean connectivity between all ROI pairs averaged across the subject group for both the (A) MEG wide-band (1–50 Hz) data and the (B) fMRI BOLD data. The results from the eyes closed condition are shown in the top row, while the bottom row corresponds to the results from the eyes open condition. Each subplot is divided into an upper triangle which shows the mean change in *z*-scores for each ROI pair and a lower triangle displaying the corresponding *t*-statistic for each ROI pair (in a mirrored fashion where only significant ($p < 0.05$) entries are filled in). A negative value (blue color) corresponds to a caffeine-induced decrease in connectivity, while a positive value (red) corresponds to an increase in connectivity. Qualitative assessment shows broad decreases in connectivity due to caffeine for the eyes closed condition and to a lesser extent in the eyes open condition, for both modalities.

that exhibited a significant ($p < 0.05$) change in connectivity across the sample. Decreases and increases in *z*-scores and *t*-statistics are indicated by blue and red hues, respectively. From a qualitative perspective, broad decreases in MEG and fMRI connectivity can be observed for the EC caffeine data and to a lesser extent in the EO data. The control data for both conditions (EC and EO) shows fewer significant changes than the caffeine data, with the MEG data showing only significant decreases and the fMRI data showing a nearly even mix of increases and decreases.

As a quantitative assessment of the data, **Table 1** summarizes the results provided by the two-way repeated measures ANOVA. For the EC condition, the caffeine/control factor showed a significant effect for both MEG and fMRI ($p \leq 0.01$), indicating that the change in correlation was significantly different between the caffeine and control sessions in both modalities. *Post hoc* two-tailed *t*-tests showed a significant decrease in mean *z*-score averaged across ROI pairs for the caffeine session [$t(9) = -4.43$, $p = 1.7e{-}3$ for MEG; $t(9) = -5.63$, $p = 3e{-}4$ for fMRI] whereas significant changes were not observed for the control session [$t(9) = -1.96$, $p = 0.08$ for MEG; $t(9) = -0.69$, $p = 0.51$ for fMRI]. The interaction terms between the factors were not significant for either modality, suggesting that the effect of the caffeine/control factor was largely independent of ROI pair. For both modalities, the effect of the caffeine/control factor did not reach significance in the EO condition. As a result, we will focus on the EC condition for the remainder of the analysis.

MEG BAND-SPECIFIC ACTIVITY

To provide further insight into the global MEG connectivity reductions observed in the EC condition, **Figure 3** shows the mean connectivity changes across all ROIs for each of the frequency bands defined in the Section "Materials and Methods" (displayed in the same manner as the wide-band MEG data in **Figure 2**). Widespread decreases in *z*-scores are evident in the caffeine data across all bands, with the strongest reductions appearing in the α, low β, and high β bands. The data from these three bands also showed connectivity decreases in the control session. A quantitative assessment using the two-way repeated measures ANOVA (**Table 2**) indicates that only the θ, low β, and high β bands showed a significant main effect ($p \leq 0.0165$) of the caffeine/control factor. The interaction term was not significant ($p \geq 0.58$) for these bands. Although the α band exhibited qualitatively large reductions in connectivity as well, the effect of the caffeine/control factor was not significant ($p = 0.085$).

To gain a better understanding of the contribution of different bands to the wide-band MEG connectivity changes, we computed the Pearson correlation between the mean Δz-scores (averaged across all ROIs for each subject) for the wide-band and band-limited MEG data. As shown in **Table 3**, significant correlations were observed for the α, low β, and high β bands in the caffeine session and for the α, low β, and low γ bands in the control session.

COMPARING fMRI AND MEG GLOBAL EFFECTS

To estimate each subject's mean global correlation, we averaged the correlation values across all ROI pairs from their respective connectivity matrix. The mean global correlations for the fMRI and MEG caffeine sessions (pre-dose and post-dose section) for all 10 subjects are plotted in the top panel of **Figure 4**. The bar graph in the bottom panel of **Figure 4** summarizes the caffeine-induced changes (post-dose minus pre-dose) in the MEG and fMRI mean global correlations for each subject. While all subjects exhibited a decrease in their overall connectivity regardless of modality, there

Table 1 | Quantitative assessment of the group data for both modalities (fMRI and wide-band MEG) and both conditions (eyes closed and open) using repeated measures two-way analysis of variance (ANOVA) to examine the effects of (1) caffeine/control and (2) ROI pair on the measured connectivity changes.

Factor	Dof	Eyes closed				Eyes open			
		MEG		fMRI		MEG		fMRI	
		F	*p*	*F*	*p*	*F*	*p*	*F*	*p*
Caffeine/control	(1, 9)	11.89	<0.01	10.45	0.01	1.38	0.27	2.70	0.13
ROI pairs	(779, 7011)	1.21	<1e−4	1.41	<1e−6	1.87	<1e−6	1.44	<1e−6
Interaction	(779, 7011)	0.85	0.99	1.04	0.23	1.07	0.10	0.99	0.60

The caffeine/control factor showed a significant ($p \leq 0.01$) effect in the eyes closed condition but not in eyes open condition (for both modalities). Interaction terms were non-significant, suggesting caffeine/control factor was largely independent of ROI pair.

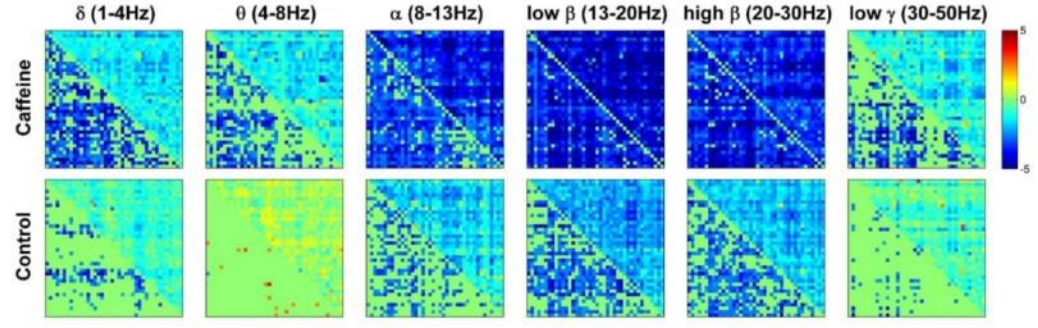

FIGURE 3 | Changes in mean connectivity (eyes closed condition) between all ROI pairs averaged across the subject group for each of the six MEG frequency bands of interest: δ (1–4 Hz), θ (4–8 Hz), α (8–13 Hz), low β (13–20 Hz), high β (20–30 Hz), and low γ (30–50 Hz). Each subplot is created in the same manner as was described in the caption of **Figure 2**. Widespread decreases in connectivity (*z*-scores) are evident in the caffeine data across all bands, with the strongest reductions appearing in the α and β bands.

Table 2 | Quantitative assessment of the group data for each of the six MEG frequency bands of interest (eyes closed condition) using repeated measures two-way analysis of variance (ANOVA) to examine the effects of (1) caffeine/control and (2) ROI pair on the measured connectivity changes.

Factor	δ		θ		α		Low β		High β		Low γ	
	F	*p*	*F*	*p*	*F*	*p*	*F*	*p*	*F*	*p*	*F*	*p*
Caffeine/control	1.72	0.22	14.38	<0.01	3.8	0.085	9.67	0.012	8.64	0.016	1.32	0.28
ROI pairs	0.80	1.00	1.23	<1e−4	2.08	<1e−6	1.66	<1e−6	1.26	<1e−6	1.45	<1e−6
Interaction	0.90	0.98	0.80	1.00	0.92	0.93	0.99	0.58	0.94	0.85	0.87	0.99

The caffeine/control factor showed a significant ($p \leq 0.0165$) effect in both the θ and β bands (interaction terms were non-significant; $p \geq 0.58$).

was not a significant relation between the magnitude of the MEG and fMRI changes [Pearson correlation coefficient $(r) = -0.18$, $p = 0.62$; Spearman's rank correlation $\rho = -0.12$, $p = 0.73$]. Further examination of **Figure 4** reveals that 8 out of the 10 subjects showed a larger decrease in correlation in the fMRI data as compared to the MEG data, while the remaining two subjects (numbers 1 and 6) showed a smaller correlation decrease in the fMRI data. These two subjects also exhibited the lowest overall fMRI pre-dose global connectivity (solid red curve in top panel) and the smallest changes in the fMRI mean global correlation when compared to the rest of the group (red bars in bottom panel). Recomputing the correlation between the magnitudes of connectivity changes for the remaining eight subjects results in a larger (although not significant) correlation (Pearson's $r = 0.62$, $p = 0.09$; Spearman's

Table 3 | Correlation (Pearson) of the connectivity changes in the wide-band MEG to the connectivity changes in each of the six MEG frequency bands of interest (eyes closed condition).

		δ	θ	α	Low β	High β	Low γ
Pearson correlation of Δz across all subjects	Caffeine	0.22	0.47	0.84*	0.79*	0.72*	0.40
	Control	0.42	0.57	0.96*	0.76*	0.56	0.67*

Connectivity changes were quantified for each subject by averaging the change in the z-score metric across all ROI pairs. Significant ($p < 0.05$) correlations are noted with a star.

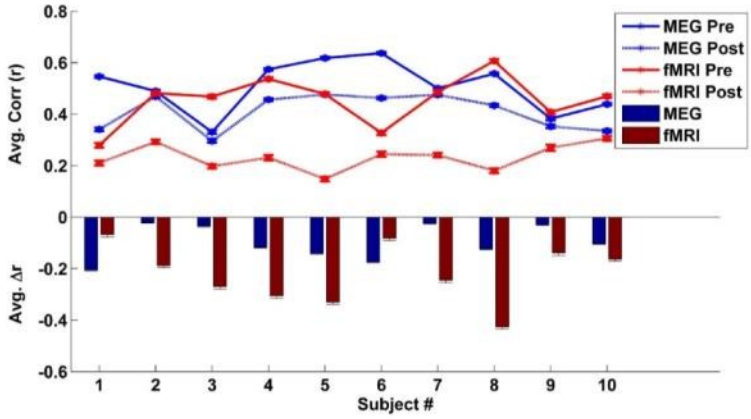

FIGURE 4 | Top panel – individual mean global correlations (averaged across all ROI pairs) are plotted for the MEG (blue lines) and fMRI (red line) eyes closed caffeine scans. The solid lines represent the mean global correlation from the pre-dose section while the dotted lines correspond to the post-dose section connectivity. **Bottom panel –** individual caffeine-induced changes in mean global correlation (post-dose section minus pre-dose section) for the MEG (blue) and the fMRI (red) caffeine sessions. Although all subjects exhibited a decrease in overall connectivity for both modalities, the magnitudes of the MEG and fMRI decreases were not significantly related. Error bars represent the standard error across regions.

$\rho = 0.71$, $p = 0.06$). The relation between MEG and fMRI measures was similar for the bands which were found in the previous section to have the strongest similarity to the wide-band MEG changes. For example, in the low-beta band, we found Pearson's $r = 0.72$, $p = 0.04$ and Spearman's $\rho = 0.69$, $p = 0.07$.

DISCUSSION

Caffeine has been previously shown to reduce the connectivity of spontaneous BOLD fluctuations across the brain (Rack-Gomer et al., 2009; Wong et al., 2012). Given the BOLD signal's complex dependence on both neural and vascular factors, it is not straightforward to assess how caffeine's modulation of these factors contributes to the observed changes in BOLD connectivity when only fMRI measures are available. In this study, we utilized MEG measures to better determine the contribution of neural changes in connectivity to the observed reductions in BOLD connectivity. We found that caffeine led to a significant and widespread reduction in both fMRI and MEG measures of resting-state connectivity in the EC condition. Neither modality revealed a significant change in connectivity for the EO condition. While our prior study (Wong et al., 2012) suggests that the lack of pronounced connectivity changes in the EO state may reflect a smaller additive global signal component (as compared to the EC state), further studies are needed to determine why both fMRI and MEG connectivity changes are more evident in the EC versus EO state. Overall, our results indicate that caffeine-related changes in neural connectivity (as assessed with MEG) play a substantial role in decreasing BOLD connectivity. In addition, as the widespread decreases in BOLD connectivity have been shown to be related to a decrease in the resting-state fMRI global signal, the concomitant decreases in MEG connectivity provide further evidence for a neural basis to the global signal (Scholvinck et al., 2010; Wong et al., 2012). In this study, we focused on the global nature of the caffeine-induced changes in connectivity. Future studies comparing changes in specific functional networks as well as differences in complex network measures of connectivity (Rubinov and Sporns, 2010) may provide deeper insights into the nature of the caffeine-induced effects and the relation between fMRI and MEG connectivity measures.

While all subjects showed a decrease in both global fMRI and MEG connectivity measures, we did not find a significant relation between the magnitude of the decreases. Because the fMRI and MEG measures cannot be obtained in a simultaneous fashion, this finding partly reflects the presence of inter-subject and inter-session variability in resting-state brain connectivity. Differences

in the experimental settings may have also been a factor (e.g., subjects were supine for the fMRI experiments but sat in a reclining chair for the MEG experiments). Prior work has demonstrated that there can be considerable variability across subjects and scans in the amplitude of the resting-state fMRI global signal, which is proportional to the average global connectivity (He and Liu, 2012; Wong et al., 2012). Variability in the degree of connectivity in the pre-dose state can alter the observed changes in connectivity. For example, if a subject has a typical level of resting-state connectivity (as compared to the rest of the sample) in the pre-dose MEG scan on one day but a lower relative level of connectivity in the pre-dose fMRI scan on another day, these differences in pre-dose connectivity will tend to lead to a relatively smaller reduction in this subject's fMRI connectivity, as compared to the decrease in their MEG connectivity. Indeed, in the current study, we find that the relation between fMRI and MEG connectivity measures is considerably weakened by the relatively low pre-dose fMRI connectivity levels in two of the subjects. When considering the measures from the remaining eight subjects, we find a stronger (and nearly significant) relation between the fMRI and wide-band MEG connectivity measures.

As prior work has shown that fMRI fluctuations reflect a complex interaction of neuronal processing across different frequency bands (Mantini et al., 2007), we also examined the contribution of different bands to the observed wide-band MEG connectivity changes. We found that connectivity changes in the β band (both low and high) exhibited a significant effect of the caffeine/control factor and that changes in these bands were significantly correlated with the connectivity changes observed in the wide-band MEG signal. This finding is consistent with the growing body of resting-state literature which has shown a close relationship between β band oscillations and the BOLD signal in the motor cortex, visual cortex, and other resting-state networks (Brookes et al., 2011b; Stevenson et al., 2011). Furthermore Liu et al. (2010) found the large-scale synchrony of MEG power fluctuations (assessed at the sensor level) to be strongest in the β band and proposed that this finding suggested a neural basis for the global signal observed in resting-state fMRI.

Although considerably more informative then sensor measurements, the MEG beamformer approach used in this study has some potential limitations. Due to overlapping lead fields, signal leakage can occur and MEG time-courses from separate locations may appear to be correlated even though no true underlying FC exists (Brookes et al., 2011a). In this study, signal leakage effects were reduced by forming average time-courses from dipoles located within a sphere of 12 mm radius at the center of each ROI, thus minimizing the inclusion of physically adjacent dipoles from different ROIs. Prior work has shown that leakage is influenced by the choice of regularization as well as preprocessing artifact reduction steps (Brookes et al., 2008a,b). We verified that the degree of regularization performed in this study was consistent with that used in prior resting-state MEG connectivity studies (Brookes et al., 2011a,b; Luckhoo et al., 2012). Future connectivity studies could perhaps better address the leakage issue by applying techniques insensitive to leakage (Brookes et al., 2012b). Furthermore, an inherent limitation of the beamformer approach is its inability to resolve correlated sources, resulting in source suppression and time-course distortion (Sekihara et al., 2002). However, these limitations may be less pronounced in this study as the beamforming is performed on the filtered MEG time series while the correlation is computed using the MEG power fluctuations (Brookes et al., 2011a,b). Nevertheless, future implementation of techniques which have addressed the issue of correlated source suppression could be beneficial (Wipf et al., 2010; Diwakar et al., 2011).

In conclusion, this study demonstrates the similarity in caffeine-induced changes as assessed with both fMRI and MEG, supporting the neural origins of the BOLD connectivity decreases. This finding serves to provide a firmer basis for the use of fMRI as a tool for the evaluation of FC at the neural level. In addition, our results further demonstrate the utility of source-localized MEG measures for the assessment of resting-state connectivity.

ACKNOWLEDGMENTS

This work was supported by NIH Grants R01NS051661 and R21MH096495, ONR MURI award no. N00014-10-1-0072, and VA Grant NURC-022-10F.

REFERENCES

Behzadi, Y., and Liu, T. T. (2005). An arteriolar compliance model of the cerebral blood flow response to neural stimulus. *Neuroimage* 25, 1100–1111.

Behzadi, Y., Restom, K., Liau, J., and Liu, T. T. (2007). A component based noise correction method (CompCor) for BOLD and perfusion based fMRI. *Neuroimage* 37, 90–101.

Biswal, B., Yetkin, F. Z., Haughton, V. M., and Hyde, J. S. (1995). Functional connectivity in the motor cortex of resting human brain using echo-planar MRI. *Magn. Reson. Med.* 34, 537–541.

Biswal, B. B., Van Kylen, J., and Hyde, J. S. (1997). Simultaneous assessment of flow and BOLD signals in resting-state functional connectivity maps. *NMR Biomed.* 10, 165–170.

Brookes, M. J., Gibson, A. M., Hall, S. D., Furlong, P. L., Barnes, G. R., Hillebrand, A., et al. (2004). A general linear model for MEG beamformer imaging. *Neuroimage* 23, 936–946.

Brookes, M. J., Hale, J. R., Zumer, J. M., Stevenson, C. M., Francis, S. T., Barnes, G. R., et al. (2011a). Measuring functional connectivity using MEG: methodology and comparison with fcMRI. *Neuroimage* 56, 1082–1104.

Brookes, M. J., Woolrich, M., Luckhoo, H., Price, D., Hale, J. R., Stephenson, M. C., et al. (2011b). Investigating the electrophysiological basis of resting state networks using magnetoencephalography. *Proc. Natl. Acad. Sci. U.S.A.* 108, 16783–16788.

Brookes, M. J., Liddle, E. B., Hale, J. R., Woolrich, M. W., Luckhoo, H., Liddle, P. F., et al. (2012a). Task induced modulation of neural oscillations in electrophysiological brain networks. *Neuroimage* 63, 1918–1930.

Brookes, M. J., Woolrich, M. W., and Barnes, G. R. (2012b). Measuring functional connectivity in MEG: a multivariate approach insensitive to linear source leakage. *Neuroimage* 63, 910–920.

Brookes, M. J., Mullinger, K. J., Stevenson, C. M., Morris, P. G., and Bowtell, R. (2008a). Simultaneous EEG source localisation and artifact rejection during concurrent fMRI by means of spatial filtering. *Neuroimage* 40, 1090–1104.

Brookes, M. J., Vrba, J., Robinson, S. E., Stevenson, C. M., Peters, A. M., Barnes, G. R., et al. (2008b). Optimising experimental design for MEG beamformer imaging. *Neuroimage* 39, 1788–1802.

Buxton, R. B., Uludag, K., Dubowitz, D. J., and Liu, T. T. (2004). Modeling the hemodynamic response to brain activation. *Neuroimage* 23(Suppl. 1), S220–S233.

Chang, C., and Glover, G. H. (2009). Effects of model-based physiological noise correction on default mode network anti-correlations and correlations. *Neuroimage* 47, 1448–1459.

Chen, Y., and Parrish, T. B. (2009). Caffeine dose effect on activation-induced BOLD and CBF responses. *Neuroimage* 46, 577–583.

Cohen, E. R., Ugurbil, K., and Kim, S. G. (2002). Effect of basal conditions on the magnitude and dynamics of the blood oxygenation level-dependent fMRI response. *J. Cereb. Blood Flow Metab.* 22, 1042–1053.

Cordes, D., Haughton, V. M., Arfanakis, K., Carew, J. D., Turski, P. A., Moritz, C. H., et al. (2001). Frequencies contributing to functional connectivity in the cerebral cortex in "resting-state" data. *AJNR Am. J. Neuroradiol.* 22, 1326–1333.

Cox, R. W. (1996). AFNI: software for analysis and visualization of functional magnetic resonance neuroimages. *Comput. Biomed. Res.* 29, 162–173.

de Pasquale, F., Della Penna, S., Snyder, A. Z., Lewis, C., Mantini, D., Marzetti, L., et al. (2010). Temporal dynamics of spontaneous MEG activity in brain networks. *Proc. Natl. Acad. Sci. U.S.A.* 107, 6040–6045.

Desikan, R. S., Segonne, F., Fischl, B., Quinn, B. T., Dickerson, B. C., Blacker, D., et al. (2006). An automated labeling system for subdividing the human cerebral cortex on MRI scans into gyral based regions of interest. *Neuroimage* 31, 968–980.

D'Esposito, M., Deouell, L. Y., and Gazzaley, A. (2003). Alterations in the BOLD fMRI signal with ageing and disease: a challenge for neuroimaging. *Nat. Rev. Neurosci.* 4, 863–872.

Dimpfel, W., Schober, F., and Spuler, M. (1993). The influence of caffeine on human EEG under resting conditions and during mental loads. *Clin. Investig.* 71, 197–207.

Diwakar, M., Tal, O., Liu, T. T., Harrington, D. L., Srinivasan, R., Muzzatti, L., et al. (2011). Accurate reconstruction of temporal correlation for neuronal sources using the enhanced dual-core MEG beamformer. *Neuroimage* 56, 1918–1928.

Dunwiddie, T. V., and Masino, S. A. (2001). The role and regulation of adenosine in the central nervous system. *Annu. Rev. Neurosci.* 24, 31–55.

Fessler, J. A., Lee, S., Olafsson, V. T., Shi, H. R., and Noll, D. C. (2005). Toeplitz-based iterative image reconstruction for MRI with correction for magnetic field inhomogeneity. *IEEE Trans. Signal Process.* 53, 3393–3402.

Fox, M. D., Snyder, A. Z., Vincent, J. L., Corbetta, M., Van Essen, D. C., and Raichle, M. E. (2005). The human brain is intrinsically organized into dynamic, anticorrelated functional networks. *Proc. Natl. Acad. Sci. U.S.A.* 102, 9673–9678.

Fox, M. D., Snyder, A. Z., Vincent, J. L., and Raichle, M. E. (2007). Intrinsic fluctuations within cortical systems account for intertrial variability in human behavior. *Neuron* 56, 171–184.

Fredholm, B. B., Battig, K., Holmen, J., Nehlig, A., and Zvartau, E. E. (1999). Actions of caffeine in the brain with special reference to factors that contribute to its widespread use. *Pharmacol. Rev.* 51, 83–133.

Glover, G. H., Li, T. Q., and Ress, D. (2000). Image-based method for retrospective correction of physiological motion effects in fMRI: RETROICOR. *Magn. Reson. Med.* 44, 162–167.

Gomez, C., Olde Dubbelink, K. T., Stam, C. J., Abasolo, D., Berendse, H. W., and Hornero, R. (2011). Complexity analysis of resting-state MEG activity in early-stage Parkinson's disease patients. *Ann. Biomed. Eng.* 39, 2935–2944.

Greicius, M. D., Srivastava, G., Reiss, A. L., and Menon, V. (2004). Default-mode network activity distinguishes Alzheimer's disease from healthy aging: evidence from functional MRI. *Proc. Natl. Acad. Sci. U.S.A.* 101, 4637–4642.

Griffeth, V. E., Perthen, J. E., and Buxton, R. B. (2011). Prospects for quantitative fMRI: investigating the effects of caffeine on baseline oxygen metabolism and the response to a visual stimulus in humans. *Neuroimage* 57, 809–816.

Hamalainen, M., Hari, R., Ilmoniemi, R. J., Knuutila, J., and Lounasmaa, O. V. (1993). Magnetoencephalography – theory, instrumentation, and applications to noninvasive studies of the working human brain. *Rev. Mod. Phys.* 65, 413–497.

Hampson, M., Driesen, N. R., Skudlarski, P., Gore, J. C., and Constable, R. T. (2006). Brain connectivity related to working memory performance. *J. Neurosci.* 26, 13338–13343.

He, B. J., Snyder, A. Z., Vincent, J. L., Epstein, A., Shulman, G. L., and Corbetta, M. (2007). Breakdown of functional connectivity in frontoparietal networks underlies behavioral deficits in spatial neglect. *Neuron* 53, 905–918.

He, H., and Liu, T. T. (2012). A geometric view of global signal confounds in resting-state functional MRI. *Neuroimage* 59, 2339–2348.

Huang, M. X., Song, T., Hagler, D. J. Jr., Podgorny, I., Jousmaki, V., Cui, L., et al. (2007). A novel integrated MEG and EEG analysis method for dipolar sources. *Neuroimage* 37, 731–748.

Hyvarinen, A. (1999). Fast and robust fixed-point algorithms for independent component analysis. *IEEE Trans. Neural Netw.* 10, 626–634.

Jenkinson, M. (2003). Fast, automated, N-dimensional phase-unwrapping algorithm. *Magn. Reson. Med.* 49, 193–197.

Jones, H. E., Herning, R. I., Cadet, J. L., and Griffiths, R. R. (2000). Caffeine withdrawal increases cerebral blood flow velocity and alters quantitative electroencephalography (EEG) activity. *Psychopharmacology (Berl.)* 147, 371–377.

Keppel, G., and Wickens, T. D. (2004). *Design and Analysis: A Researcher's Handbook.* Upper Saddle River: Pearson Prentice Hall.

Kwak, Y., Peltier, S., Bohnen, N. I., Muller, M. L., Dayalu, P., and Seidler, R. D. (2010). Altered resting state cortico-striatal connectivity in mild to moderate stage Parkinson's disease. *Front. Syst. Neurosci.* 4:143. doi:10.3389/fnsys.2010.00143

Laurienti, P. J., Field, A. S., Burdette, J. H., Maldjian, J. A., Yen, Y. F., and Moody, D. M. (2002). Dietary caffeine consumption modulates fMRI measures. *Neuroimage* 17, 751–757.

Liau, J., Perthen, J. E., and Liu, T. T. (2008). Caffeine reduces the activation extent and contrast-to-noise ratio of the functional cerebral blood flow response but not the BOLD response. *Neuroimage* 42, 296–305.

Liu, T. T., Behzadi, Y., Restom, K., Uludag, K., Lu, K., Buracas, G. T., et al. (2004). Caffeine alters the temporal dynamics of the visual BOLD response. *Neuroimage* 23, 1402–1413.

Liu, Z., Fukunaga, M., de Zwart, J. A., and Duyn, J. H. (2010). Large-scale spontaneous fluctuations and correlations in brain electrical activity observed with magnetoencephalography. *Neuroimage* 51, 102–111.

Lowe, M. J., Mock, B. J., and Sorenson, J. A. (1998). Functional connectivity in single and multislice echoplanar imaging using resting-state fluctuations. *Neuroimage* 7, 119–132.

Lowe, M. J., Phillips, M. D., Lurito, J. T., Mattson, D., Dzemidzic, M., and Mathews, V. P. (2002). Multiple sclerosis: low-frequency temporal blood oxygen level-dependent fluctuations indicate reduced functional connectivity initial results. *Radiology* 224, 184–192.

Luckhoo, H., Hale, J. R., Stokes, M. G., Nobre, A. C., Morris, P. G., Brookes, M. J., et al. (2012). Inferring task-related networks using independent component analysis in magnetoencephalography. *Neuroimage* 62, 530–541.

Lui, S., Ouyang, L., Chen, Q., Huang, X., Tang, H., Chen, H., et al. (2008). Differential interictal activity of the precuneus/posterior cingulate cortex revealed by resting state functional MRI at 3T in generalized vs. partial seizure. *J. Magn. Reson. Imaging* 27, 1214–1220.

Mantini, D., Della Penna, S., Marzetti, L., de Pasquale, F., Pizzella, V., Corbetta, M., et al. (2011). A signal-processing pipeline for magnetoencephalography resting-state networks. *Brain Connect.* 1, 49–59.

Mantini, D., Perrucci, M. G., Del Gratta, C., Romani, G. L., and Corbetta, M. (2007). Electrophysiological signatures of resting state networks in the human brain. *Proc. Natl. Acad. Sci. U.S.A.* 104, 13170–13175.

Mosher, J. C., Leahy, R. M., and Lewis, P. S. (1999). EEG and MEG: forward solutions for inverse methods. *IEEE Trans. Biomed. Eng.* 46, 245–259.

Rack-Gomer, A. L., Liau, J., and Liu, T. T. (2009). Caffeine reduces resting-state BOLD functional connectivity in the motor cortex. *Neuroimage* 46, 56–63.

Rack-Gomer, A. L., and Liu, T. T. (2012). Caffeine increases the temporal variability of resting-state BOLD connectivity in the motor cortex. *Neuroimage* 59, 2994–3002.

Raichle, M. E., Macleod, A. M., Snyder, A. Z., Powers, W. J., Gusnard, D. A., and Shulman, G. L. (2001). A default mode of brain function. *Proc. Natl. Acad. Sci. U.S.A.* 98, 676–682.

Reeves, R. R., Struve, F. A., and Patrick, G. (2002). Topographic quantitative EEG response to acute caffeine withdrawal: a comprehensive analysis of multiple quantitative variables. *Clin. Electroencephalogr.* 33, 178–188.

Robinson, S., and Vrba, J. (1998). *Functional Neuroimaging by Synthetic Aperture Magnetometry.* Sendai: Tohoku University Press.

Rubinov, M., and Sporns, O. (2010). Complex network measures of brain connectivity: uses and interpretations. *Neuroimage* 52, 1059–1069.

Scholvinck, M. L., Maier, A., Ye, F. Q., Duyn, J. H., and Leopold, D. A. (2010). Neural basis of global resting-state fMRI activity. *Proc. Natl. Acad. Sci. U.S.A.* 107, 10238–10243.

Schoonheim, M. M., Geurts, J. J., Landi, D., Douw, L., van der Meer, M. L.,

Vrenken, H., et al. (2011). Functional connectivity changes in multiple sclerosis patients: a graph analytical study of MEG resting state data. *Hum. Brain Mapp.* 34, 52–61.

Sekihara, K., and Nagarajan, S. S. (2008). *Adaptive Spatial Filters for Electromagnetic Brain Imaging.* Berlin: Springer.

Sekihara, K., Nagarajan, S. S., Poeppel, D., and Marantz, A. (2002). Performance of an MEG adaptive-beamformer technique in the presence of correlated neural activities: effects on signal intensity and time-course estimates. *IEEE Trans. Biomed. Eng.* 49, 1534–1546.

Siepmann, M., and Kirch, W. (2002). Effects of caffeine on topographic quantitative EEG. *Neuropsychobiology* 45, 161–166.

Smith, S. M., Fox, P. T., Miller, K. L., Glahn, D. C., Fox, P. M., Mackay, C. E., et al. (2009). Correspondence of the brain's functional architecture during activation and rest. *Proc. Natl. Acad. Sci. U.S.A.* 106, 13040–13045.

Smith, S. M., Jenkinson, M., Woolrich, M. W., Beckmann, C. F., Behrens, T. E., Johansen-Berg, H., et al. (2004). Advances in functional and structural MR image analysis and implementation as FSL. *Neuroimage* 23(Suppl. 1), S208–S219.

Song, M., Zhou, Y., Li, J., Liu, Y., Tian, L., Yu, C., et al. (2008a). Brain spontaneous functional connectivity and intelligence. *Neuroimage* 41, 1168–1176.

Song, T., Gaa, K., Cui, L., Feffer, L., Lee, R. R., and Huang, M. (2008b). Evaluation of signal space separation via simulation. *Med. Biol. Eng. Comput.* 46, 923–932.

Song, T., Cui, L., Gaa, K., Feffer, L., Taulu, S., Lee, R. R., et al. (2009). Signal space separation algorithm and its application on suppressing artifacts caused by vagus nerve stimulation for magnetoencephalography recordings. *J. Clin. Neurophysiol.* 26, 392–400.

Stamatakis, E. A., Adapa, R. M., Absalom, A. R., and Menon, D. K. (2010). Changes in resting neural connectivity during propofol sedation. *PLoS ONE* 5:e14224. doi:10.1371/journal.pone.0014224

Stevenson, C. M., Brookes, M. J., and Morris, P. G. (2011). Beta-band correlates of the fMRI BOLD response. *Hum. Brain Mapp.* 32, 182–197.

Tarapore, P. E., Martino, J., Guggisberg, A. G., Owen, J., Honma, S. M., Findlay, A., et al. (2012a). Magnetoencephalographic imaging of resting-state functional connectivity predicts postsurgical neurological outcome in brain gliomas. *Neurosurgery* 71, 1012–1022.

Tarapore, P. E., Tate, M. C., Findlay, A. M., Honma, S. M., Mizuiri, D., Berger, M. S., et al. (2012b). Preoperative multimodal motor mapping: a comparison of magnetoencephalography imaging, navigated transcranial magnetic stimulation, and direct cortical stimulation. *J. Neurosurg.* 117, 354–362.

Taulu, S., Kajola, M., and Simola, J. (2004). Suppression of interference and artifacts by the Signal Space Separation Method. *Brain Topogr.* 16, 269–275.

Taulu, S., and Simola, J. (2006). Spatiotemporal signal space separation method for rejecting nearby interference in MEG measurements. *Phys. Med. Biol.* 51, 1759–1768.

van den Heuvel, M. P., and Hulshoff Pol, H. E. (2010). Exploring the brain network: a review on resting-state fMRI functional connectivity. *Eur. Neuropsychopharmacol.* 20, 519–534.

Van Dijk, K. R., Hedden, T., Venkataraman, A., Evans, K. C., Lazar, S. W., and Buckner, R. L. (2010). Intrinsic functional connectivity as a tool for human connectomics: theory, properties, and optimization. *J. Neurophysiol.* 103, 297–321.

van Drongelen, W., Yuchtman, M., van Veen, B. D., and van Huffelen, A. C. (1996). A spatial filtering technique to detect and localize multiple sources in the brain. *Brain Topogr.* 9, 39–49.

Van Veen, B. D., van Drongelen, W., Yuchtman, M., and Suzuki, A. (1997). Localization of brain electrical activity via linearly constrained minimum variance spatial filtering. *IEEE Trans. Biomed. Eng.* 44, 867–880.

Westlake, K. P., Hinkley, L. B., Bucci, M., Guggisberg, A. G., Findlay, A. M., Henry, R. G., et al. (2012). Resting state alpha-band functional connectivity and recovery after stroke. *Exp. Neurol.* 237, 160–169.

Wipf, D. P., Owen, J. P., Attias, H. T., Sekihara, K., and Nagarajan, S. S. (2010). Robust Bayesian estimation of the location, orientation, and time course of multiple correlated neural sources using MEG. *Neuroimage* 49, 641–655.

Wong, C. W., Olafsson, V., Tal, O., and Liu, T. T. (2012). Anti-correlated networks, global signal regression, and the effects of caffeine in resting-state functional MRI. *Neuroimage* 63, 356–364.

Zamrini, E., Maestu, F., Pekkonen, E., Funke, M., Makela, J., Riley, M., et al. (2011). Magnetoencephalography as a putative biomarker for Alzheimer's disease. *Int. J. Alzheimers Dis.* 2011, 280289.

Conflict of Interest Statement: The authors declare that the research was conducted in the absence of any commercial or financial relationships that could be construed as a potential conflict of interest.

Received: 30 November 2012; accepted: 16 February 2013; published online: 04 March 2013.

Citation: Tal O, Diwakar M, Wong C-W, Olafsson V, Lee R, Huang M-X and Liu TT (2013) Caffeine-induced global reductions in resting-state BOLD connectivity reflect widespread decreases in MEG connectivity. Front. Hum. Neurosci. 7:63. doi: 10.3389/fnhum.2013.00063

Acknowledgements

Chapter 1, in full, is a reprint of the material as it appears in Frontiers in Human Neuroscience 2013. Tal, Omer; Diwakar, Mithun; Wong, Chi-Wah; Olafsson, Valur; Lee, Ronald; Huang, Ming-Xiong; Liu, Thomas T., (2013). Caffeine-induced global reductions in resting-state BOLD connectivity reflect widespread decreases in MEG connectivity. Front. Hum. Neurosci. 7(63): 1-10. The dissertation author was the primary investigator and author of this paper.

CHAPTER 2

Contents lists available at ScienceDirect

NeuroImage

journal homepage: www.elsevier.com/locate/ynimg

Accurate reconstruction of temporal correlation for neuronal sources using the enhanced dual-core MEG beamformer

Mithun Diwakar [a,b,1], Omer Tal [a,b,1], Thomas T. Liu [a,b], Deborah L. Harrington [a,c], Ramesh Srinivasan [d,e], Laura Muzzatti [a], Tao Song [a], Rebecca J. Theilmann [a], Roland R. Lee [a,c], Ming-Xiong Huang [a,c,*]

[a] Department of Radiology, University of California, San Diego, La Jolla, CA, USA
[b] Department of Bioengineering, University of California, San Diego, La Jolla, CA, USA
[c] Research and Radiology Services, VA San Diego Healthcare System, San Diego, CA, USA
[d] Department of Cognitive Sciences, University California, Irvine, Irvine, CA, USA
[e] Department of Biomedical Engineering, University California, Irvine, Irvine, CA, USA

ARTICLE INFO

Article history:
Received 2 November 2010
Revised 16 February 2011
Accepted 16 March 2011
Available online xxxx

ABSTRACT

Beamformer spatial filters are commonly used to explore the active neuronal sources underlying magnetoencephalography (MEG) recordings at low signal-to-noise ratio (SNR). Conventional beamformer techniques are successful in localizing uncorrelated neuronal sources under poor SNR conditions. However, the spatial and temporal features from conventional beamformer reconstructions suffer when sources are correlated, which is a common and important property of real neuronal networks. Dual-beamformer techniques, originally developed by Brookes et al. to deal with this limitation, successfully localize highly-correlated sources and determine their orientations and weightings, but their performance degrades at low correlations. They also lack the capability to produce individual time courses and therefore cannot quantify source correlation. In this paper, we present an enhanced formulation of our earlier *dual-core beamformer* (DCBF) approach that reconstructs individual source time courses and their correlations. Through computer simulations, we show that the enhanced DCBF (eDCBF) consistently and accurately models dual-source activity regardless of the correlation strength. Simulations also show that a multi-core extension of eDCBF effectively handles the presence of additional correlated sources. In a human auditory task, we further demonstrate that eDCBF accurately reconstructs left and right auditory temporal responses and their correlations. Spatial resolution and source localization strategies corresponding to different measures within the eDCBF framework are also discussed. In summary, eDCBF accurately reconstructs source spatio-temporal behavior, providing a means for characterizing complex neuronal networks and their communication.

Introduction

Magnetoencephalography (MEG) is a functional imaging modality that directly detects neuronal activity with millisecond temporal resolution. Reconstruction of source space neural activity requires an adequate forward model based on the sensor and conductivity distribution (related to head geometry) and subsequent inverse modeling with the actual neuromagnetic recordings. Since the MEG inverse problem does not have a unique solution, assumptions about the sources (i.e. source modeling) must be made to properly localize and reconstruct sources of neuronal activity (Hamalainen and Ilmoniemi, 1994). The *conventional single beamformer* (SBF), a type of adaptive spatial filter, reconstructs sources with high spatial accuracy under poor signal-to-noise ratio (SNR) conditions, but assumes that the neuronal sources are uncorrelated (Robinson and Vrba, 1998; Sekihara et al., 2002; Van Drongelen et al., 1996; Van Veen et al., 1997). This assumption is not ideal since neural responses commonly involve communication between multiple sources within the same or across different neuronal networks. Many modified beamformer approaches have been proposed to overcome this limiting assumption.

The *nulling beamformer* (NB) and the *coherent source suppression model* (CSSM) seek to deal with correlated sources by constraining the beamformer gain for a single source to zero at pre-determined interfering locations (Dalal et al., 2006; Hui and Leahy, 2006; Hui et al., 2010; Quuran and Cheyne, 2010). While the NB and CSSM can successfully handle correlated sources individually given the appropriate nulling constraints (location of interfering sources), multiple computations of source beamformer weights are still required to determine source correlation. The *array-gain constraint minimum-norm filter with recursively-updated gram matrix* (AGMN-RUG) spatial filter seeks to improve the spatial reconstruction of both uncorrelated

* Corresponding author at: Radiology Imaging Laboratory, Department of Radiology, University of California, San Diego, 3510 Dunhill Street, San Diego, CA92121, USA.
E-mail address: mxhuang@ucsd.edu (M.-X. Huang).
[1] Dual-first author arrangement—both authors contributed equally to the work.

and correlated sources by optimizing the gram matrix with the actual biomagnetic measurements (Kumihashi and Sekihara, 2010). Though the AGMN-RUG spatial filter does not require *a priori* information and is quite powerful with only a few iterations of the recursive algorithm, measurements with high SNR are necessary for it to perform effectively. Thus, the beamformer is well-suited to study neural response to evoked stimulation, but is not ideal for studying brain activities that are not time- or phase-locked to stimuli.

The *dual-source beamformer* (DSBF) seeks to reconstruct correlated sources by using spatial filters formulated from a linear combination of two sources' lead-field vectors. The technique requires non-linear optimization of source orientation angles and source amplitude weighting, in addition to a brute-force search across all possible source dipole combinations. This approach has a high computational cost, which greatly limits its application in practice. Furthermore, source time course retrieval yields only a single, combined waveform for both sources. Also, the output from the DSBF spatial filter is compromised when sources are poorly correlated, while its inability to produce individual source time courses limits the quantitative measurement of source correlation (Brookes et al., 2007).

Our recently developed *dual-core beamformer* (DCBF) addresses many of the limitations of the DSBF developed by Brookes et al. (Diwakar et al., 2011). The DCBF implements the DSBF with a vector description, eliminating the need for non-linear searches of source orientations and source weighting. Furthermore, pairing the DCBF with a Powell search optimization algorithm allows quick localization of the correlated source pairs. However, our simulations demonstrated that the estimation of source amplitudes with DCBF grows inaccurate as correlation values decrease since time course reconstruction only generates a single signal (scaled accordingly for each source). Though DCBF provides an effective way to identify source pairs, the measurement statistic (pseudo-Z-score) obtained is dependent on both source power and source correlation and does not exclusively quantify correlation between sources.

Ideally, in addition to localizing active sources, a quantitative measure of correlation is desired to obtain a more complete understanding of neuronal networks. Such a measure (e.g. power correlation) would more completely characterize highly sophisticated networks. In this manuscript, we propose an *enhanced dual-core beamformer* (eDCBF), which is capable of accurately estimating the source covariance matrix from multiple sources, providing a proper measure of correlation in addition to individual source time courses without amplitude suppression. Once sources are localized, their correlation can be found *without time course reconstruction*, allowing the eDCBF to handle large datasets quickly and requiring little memory. If desired, the eDCBF also provides a simple way of computing correlations in frequency bands of interest. Moreover, eDCBF's improved design offers robustness to a wide range of both source correlations and SNR. Finally, the eDCBF framework may be generalized to effectively account for the presence of multiple sources.

The mathematical formulation of the eDCBF and extension to the *multi-core beamformer* (MCBF) are first presented to fully demonstrate the design of the new spatial filter. In simulations we demonstrate that the eDCBF spatial filter is robust to a wide range of correlations, SNRs, source locations, and various source temporal dynamics. Using a three-core MCBF filter, we further demonstrate how additional sources of interference can be accounted for once source localization is performed. Finally, we cross-validate our findings from the simulations in an analysis of a human MEG recording during a stereo auditory stimulation task, showing that the eDCBF produces meaningful correlation estimations and accurate time courses.

Methods

General lead-field model

Let $b(t)$ be an $m\times 1$ vector of sensor measurements at time t, $n(t)$ be an $m\times 1$ vector of sensor noise measurements, and $s(t)$ be a $2p\times 1$ matrix of vector source amplitudes, where m is the number of sensors and p is the number of pre-defined dipolar sources. Let the lead-field matrix defined in two directions θ and ϕ for the ith source be denoted by the $m\times 2$ matrix $L_i = [\,l_{\theta,i} \quad l_{\phi,i}\,]$. In the spherical MEG forward head model, θ and ϕ represent the two tangential orientations for each dipole location, whereas in a realistic MEG forward model using the boundary element method (BEM), the θ and ϕ orientations are obtained as the two dominant orientations from the singular value decomposition (SVD) of the $m\times 3$ lead-field matrix for each dipole, as previously documented (Huang et al., 2006). The composite lead-field matrix or gain matrix is defined as the $m\times 2p$ matrix $L = [\,L_1 \quad L_2 \quad L_3 \quad \cdots \quad L_p\,]$. The MEG signal equation can be written as:

$$b(t) = Ls(t) + n(t) \tag{1}$$

Taking the covariance of Eq. (1) and assuming that the noise and signal are uncorrelated leads to the covariance relationship:

$$R_b = LR_s^pL^T + R_n \tag{2}$$

R_b is the $m\times m$ sensor covariance matrix, R_s^p is the $2p\times 2p$ source covariance matrix, and R_n is the $m\times m$ noise covariance matrix.

Previous dual-core beamformer formulation (Diwakar et al., 2011)

The DCBF was developed assuming the presence of two sources. Let L_1 and L_2 define the lead-field matrices of the two sources of interest. The dual-core lead-field matrix is expressed as the $m\times 4$ matrix $L_d = [\,L_1 \quad L_2\,]$. The DCBF weighting matrix is then defined as the $m\times 1$ vector W_d designed such that:

$$\hat{s}(t) = \nu_1 W_d^T b(t) \tag{3}$$

where $\hat{s}(t)$ represents the 4×1 vector of estimated source time courses in both the θ and ϕ directions. ν_1 is defined as a 4×1 vector containing both optimal non-normalized 2×1 source orientations η_1 and η_2:

$$\nu_1 = \begin{pmatrix} \eta_1 \\ \eta_2 \end{pmatrix} \tag{4}$$

ν_1 is obtained by computing the eigenvector associated with the weakest eigenvalue of $Q_{dual} = L_d^T R_b^{-1} L_d$, where the dual-source power P_{opt} is represented by the inverse of the eigenvalue. The DCBF solution for the weighting matrix was shown to be (Diwakar et al., 2011):

$$W_d = P_{opt} R_b^{-1} L_d \nu_1 \tag{5}$$

The DCBF orientations from Eq. (4) reduce L_d to a rank 1 scalar lead-field matrix leading to an $m\times 1$ beamformer weight (Eq. (5)), resulting in scaled copies of a single time course to represent both sources. Furthermore, a single eigenvector of Q_{dual} (ν_1) can only capture either the correlated or uncorrelated part of the signal and is not sufficient to span the entire signal subspace, leading to incorrect estimates of source amplitude in the presence of non-highly correlated sources.

Enhanced dual-core beamformer formulation

The enhanced dual-core beamformer (eDCBF) offers a novel solution to overcome the deficits of the previous DCBF. The eDCBF dual-core lead-field matrix is expressed identically to the original DCBF (Diwakar et al., 2011). Instead of using the DCBF $m\times 1$ weighting vector, the eDCBF weighting matrix is defined as the $m\times 4$ matrix $W_d = [\,W_1 \quad W_2\,]$, where W_i are the individual weighting matrices for each source, ensuring no reduction in rank and enabling the

computation of unique source time courses and correlation. The eDCBF weighting matrix is designed such that:

$$\hat{s}(t) = W_d^T b(t) \tag{6}$$

$\hat{s}(t)$ is the 4×1 vector of unique estimated dual-source time courses in both the θ and ϕ directions. As a measure of source strength and activity, the 4×4 eDCBF estimated dual-source covariance matrix $R_{\hat{s}}$ is determined by taking the covariance of Eq. (6):

$$R_{\hat{s}} = \left\langle \hat{s}(t)\hat{s}(t)^T \right\rangle = W_d^T R_b W_d \tag{7}$$

The constraints of the vector minimum-variance beamformer, consistently shown to produce accurate beamformer reconstruction with single sources (Sekihara et al., 2004; Spencer et al., 1992; Van Veen et al., 1997), may be used to derive the eDCBF weighting matrix W_d:

$$W_d = \arg\min_{W_d} tr\left\{W_d^T R_b W_d\right\} \text{ subject to } W_d^T L_d = I \tag{8}$$

The matrix product $W_d^T L_d$ represents the spatial filter output from two unit-magnitude impulse currents. The linear constraint $W_d^T L_d = I$ ensures that each weighting vector W_i passes signal from its respective source while not passing signal from the second source. Furthermore, the trace of the beamformer output source power $W_d^T R_b W_d$ is minimized to suppress both noise and additional source contributions. However, no assumptions are made about the correlation between the two sources of interest. In fact, the correlation can take on any value from 0 for uncorrelated sources to 1 for completely synchronized sources. The solution for the minimization problem may be obtained by minimizing the Lagrangian with Lagrange multiplier κ:

$$\mathcal{L}(W_d, \kappa) = tr\left\{W_d^T R_b W_d + \left(W_d^T L_d - I\right)\kappa\right\} \tag{9}$$

The derivative of the Lagrangian may be computed using the matrix derivative identities $\frac{\partial}{\partial X} tr\{X^T A\} = A$ and $\frac{\partial}{\partial X} tr\{X^T A X\} = AX + A^T X$:

$$\frac{\partial \mathcal{L}(W_d, \kappa)}{\partial W_d} = 2R_b W_d + L_d \kappa = 0 \tag{10}$$

$$W_d = -R_b^{-1} L_d \kappa / 2 \tag{11}$$

Substituting the unit-gain constraint $W_d^T L_d = I$ into Eq. (11) yields:

$$\kappa = -2\left(L_d^T R_b^{-1} L_d\right)^{-1} \tag{12}$$

$$W_d = R_b^{-1} L_d \left(L_d^T R_b^{-1} L_d\right)^{-1} \tag{13}$$

The eDCBF estimated dual-source covariance matrix $R_{\hat{s}}$, which is equal to the inverse of the DCBF Q_{dual}, may be obtained by substituting the derived eDCBF beamformer weight from Eq. (13) into Eq. (7):

$$R_{\hat{s}} = W_d^T R_b W_d = \left(L_d^T R_b^{-1} L_d\right)^{-1} \tag{14}$$

The eDCBF time courses are obtained by substituting the derived eDCBF beamformer weight from Eq. (13) into Eq. (6):

$$\hat{s}(t) = W_d^T b(t) = \left(L_d^T R_b^{-1} L_d\right)^{-1} L_d^T R_b^{-1} b(t) = R_{\hat{s}} L_d^T R_b^{-1} b(t) \tag{15}$$

The eDCBF uses the full dual-source covariance matrix ($R_{\hat{s}}$ or Q_{dual}^{-1}) instead of a single eigenvector when determining the weighting matrix, preventing undesired amplitude suppression and allowing reconstruction of unique time courses. Thus, the eDCBF makes it possible to define and compute source correlation.

eDCBF estimated correlation reconstruction

The eDCBF estimated vector covariance matrix $R_{\hat{s}}$ can be expressed as:

$$R_{\hat{s}} = \begin{bmatrix} \left\langle \hat{s}_1(t)\hat{s}_1(t)\right\rangle \overline{\eta}_1 \overline{\eta}_1^T & \left\langle \hat{s}_1(t)\hat{s}_2(t)\right\rangle \overline{\eta}_1 \overline{\eta}_2^T \\ \left\langle \hat{s}_2(t)\hat{s}_1(t)\right\rangle \overline{\eta}_2 \overline{\eta}_1^T & \left\langle \hat{s}_2(t)\hat{s}_2(t)\right\rangle \overline{\eta}_2 \overline{\eta}_2^T \end{bmatrix} \tag{16}$$

where $\hat{s}_i(t)$ are the estimated scalar source time courses and $\overline{\eta}_i$ are the 2×1 normalized orientations for the two sources. The two diagonal 2×2 sub-matrices of $R_{\hat{s}}$ are of the same form as SBF vector covariance matrices (Sekihara et al., 2004). Thus, the eigenvectors corresponding to the maximum eigenvalues (signal-related) of these sub-matrices contain the source orientations, while the eigenvectors corresponding to the minimum eigenvalues (noise-related) contain the noise orientations. The 4×2 source orientation matrix ψ is used to reduce the 4×4 vector source covariance matrix to the 2×2 estimated dual-source scalar covariance matrix $\tilde{R}_{\hat{s}}$:

$$\psi = \begin{pmatrix} \overline{\eta}_1 & 0 \\ 0 & \overline{\eta}_2 \end{pmatrix} \tag{17}$$

$$\tilde{R}_{\hat{s}} = \psi^T R_{\hat{s}} \psi \tag{18}$$

The orientation matrix also allows scalar source time course recovery:

$$\tilde{s}(t) = \psi^T W_d^T b(t) \tag{19}$$

The estimated dual-source power correlation $\hat{\chi}_{12}$ may be computed from:

$$\hat{\chi}_{12} = \frac{\tilde{R}_{\hat{s}}(1,2)^2}{\tilde{R}_{\hat{s}}(1,1)\tilde{R}_{\hat{s}}(2,2)} \tag{20}$$

Amplitude correlation $\hat{\chi}_{12}^a$ can be computed as the square root of Eq. (20).

eDCBF transformed correlation reconstruction

Often, it is desirable to examine the source activity in a certain frequency band or envelope of the source signals. The eDCBF weighting matrix W_d can be derived from either the transformed or original sensor recordings. Use of the original recordings allows determination of source orientations and W_d based on the complete source power spectrum, which is more representative of true source activity. Furthermore, the eDCBF provides a straightforward way to compute correlations and time courses when W_d has been derived from the original signal. $\hat{s}_\xi(t)$, the transformed time courses of $\hat{s}(t)$, are defined by transforming Eq. (15) in the time domain:

$$\hat{s}_\xi(t) = \xi\left[\hat{s}(t)\right] = W_d^T \xi[b(t)] = W_d^T b_\xi(t) \tag{21}$$

where $b_\xi(t)$ are the transformed sensor time courses and ξ is the operator of the transformation. The transformed source covariance

matrix $R_{\hat{s}}^{\xi}$ may be computed with the transformed sensor covariance matrix $R_b^{\xi} = \langle b_{\xi}(t) b_{\xi}(t)^T \rangle$ without computation of source time courses:

$$R_{\hat{s}}^{\xi} = \left\langle \hat{s}_f(t) \hat{s}_f(t)^T \right\rangle = W_d^T R_b^{\xi} W_d \tag{22}$$

The estimated correlation may be computed from the transformed source covariance matrix in the same fashion as Eqs. (18) and (20). Furthermore, Eqs. (21) and (22) hold for any linear transformations in the time domain.

eDCBF regularized correlation reconstruction

Use of the regularized beamformer has greatly improved the quality of beamformer signal time course reconstruction (Robinson and Vrba, 1998; Van Veen et al., 1997; Hillebrand et al., 2005). The eDCBF beamformer weight can be reformulated to obtain the regularized beamformer weight W_d^r

$$W_d^r = (R_b + \gamma I)^{-1} L_d \left(L_d^T (R_b + \gamma I)^{-1} L_d \right)^{-1} \tag{23}$$

where γ is the regularization parameter that increases the full-width half-maximum of the beamformer point-spread function while reducing the amount of uncorrelated noise. Source time courses may be reconstructed as:

$$\hat{s}_r(t) = (W_d^r)^T b(t) \tag{24}$$

Source correlation may be computed from the regularized estimated source covariance matrix $R_{\hat{s}}^r$ without computation of time courses using Eqs. (18) and (20).

$$R_{\hat{s}}^r = \left\langle \hat{s}_r(t) \hat{s}_r(t)^T \right\rangle = (W_d^r)^T R_b W_d^r \tag{25}$$

Correlation and time courses in specific frequency bands may be computed by using the regularized beamformer weight W_d^r in conjunction with Eqs. (21) and (22).

eDCBF noise-corrected correlation reconstruction

The estimated dual-source covariance matrix can be heavily biased by the presence of noise, making true prediction of correlation difficult. Further investigation reveals that this bias can be corrected using the sensor noise covariance R_n. The expression for R_b from Eq. (2) may be equivalently written as $R_b = \tilde{L} \tilde{R}_s^p \tilde{L}^T + R_n$, where the scalar composite lead-field matrix is given by $\tilde{L} = [l_1 \quad l_2 \quad \cdots \quad l_p]$ and $\tilde{R}_s^p$ is the $p \times p$ scalar source covariance matrix. The $m \times 1$ vectors l_i that comprise $\tilde{L}$ are the scalar lead-fields for each source along its true orientation $\overline{\eta}_i$ where $l_i = L_i \overline{\eta}_i$. By substituting this expression for R_b into Eq. (7), it is evident that the estimated source covariance matrix $R_{\hat{s}}$ is composed of a noise-free component (first term on the right-hand-most side of Eq. (26)) and a noise-related component (second term on the right-hand-most side of Eq. (26)):

$$R_{\hat{s}} = \left\langle \hat{s}(t) \hat{s}(t)^T \right\rangle = W_d^T R_b W_d = W_d^T \tilde{L} \tilde{R}_s^p \tilde{L}^T W_d + W_d^T R_n W_d \tag{26}$$

The process of minimization and application of linear constraints result in weight vectors that satisfy $W_d^T l_i = 0$ for $i : 3 \rightarrow p$ by assuming that the corresponding sources are uncorrelated with each other as well as the two sources of interest (Sekihara et al., 2002). The noise-free component then reduces to the 4×4 true dual-source vector covariance matrix R_s:

$$W_d^T \tilde{L} \tilde{R}_s^p \tilde{L}^T W_d = R_s \tag{27}$$

Eq. (27) also remains valid when only two sources are present. When additional partially correlated sources exist, the multi-core extension presented in the next section must be used. Eq. (26) then simplifies to:

$$R_{\hat{s}} = R_s + W_d^T R_n W_d \tag{28}$$

Substituting the derived beamformer weight (Eq. (13)) into Eq. (28) and solving for R_s yields:

$$R_s = \left(I - R_{\hat{s}} L_d^T R_b^{-1} R_n R_b^{-1} L_d \right) R_{\hat{s}} \tag{29}$$

To obtain the noise-corrected correlation, an unbiased estimate of the noise covariance R_n is essential. The true dual-source vector covariance matrix can then be reduced using the derived orientations to the 2×2 true dual-source scalar covariance matrix $\tilde{R}_s$ to compute the noise-corrected correlation value χ_{12}:

$$\tilde{R}_s = \psi^T R_s \psi \tag{30}$$

$$\chi_{12} = \frac{\tilde{R}_s(1,2)^2}{\tilde{R}_s(1,1) \tilde{R}_s(2,2)} \tag{31}$$

Using the definition of the matrix $K = W_d^T R_n W_d (W_d^T R_b W_d)^{-1} = R_{\hat{s}} L_d^T R_b^{-1} R_n R_b^{-1} L_d$ from the original DCBF (Diwakar et al., 2011), Eq. (29) can be written as:

$$R_s = (I - K) R_{\hat{s}} \tag{32}$$

Thus, the relationship between the true dual-source vector covariance and the estimated dual-source vector covariance is dependent on the K matrix, which is inversely proportional to the source space SNR. As shown previously, the K-related dual-source pseudo-Z-score (Z^K)may be obtained by inverting the minimum eigenvalue of the K matrix (Robinson and Vrba, 1998; Vrba and Robinson, 2001; Sekihara et al., 2004; Diwakar et al., 2011):

$$Z^K = \min(eig(K))^{-1} \tag{33}$$

This pseudo-Z-score can be used as a measure of relative source activity. Alternatively, the power pseudo-Z-score may be computed by dividing the dual-source power by the noise power (Van Veen et al., 1997):

$$Z^P = tr\{R_{\hat{s}}\} / tr\left\{ \left(L_d^T R_n^{-1} L_d \right)^{-1} \right\} \tag{34}$$

The differences in the spatial profile of Z^K and Z^P will be investigated in Results.

Extension to multi-core beamformer (MCBF)

We previously demonstrated that using DCBF to model two sources is sufficient to reveal complex neuronal networks with many sources due to only partial suppression of the pseudo-Z-score (Diwakar et al., 2011). However, as shown by Eq. (27), the eDCBF can only account for two correlated sources in the presence of other uncorrelated sources. When multiple correlated sources exist, the correlation coefficient and time course reconstruction are affected severely. Therefore, the model needs to be expanded to handle such environments.

A *multi-core beamformer* (MCBF) can be developed to account for additional sources. The technique can be described by a straightforward extension of the eDCBF. Starting from Eq. (2), the multi-core lead-field vector is defined as the $m \times 2c$ matrix $L_m = [L_1 \quad L_2 \quad \cdots \quad L_c]$, where c is the desired number of sources to be modeled. The

corresponding multi-core weighting vector is then defined as the $m \times 2c$ matrix $W_m = [W_1 \quad W_2 \quad \cdots \quad W_c]$. The solution to the multi-core weighting vector, W_m, is derived in an equivalent manner to Eqs. (8) through (13):

$$W_m = R_b^{-1} L_m \left(L_m^T R_b^{-1} L_m \right)^{-1} \tag{35}$$

The derivations presented from Eqs. (14) to (31) can then be applied to the multi-core beamformer to obtain the $2c \times 2c$ estimated multi-core vector covariance matrix $R_{\hat{s}}$, the $2c \times 2c$ true multi-core vector covariance matrix R_s, the $c \times c$ estimated multi-core scalar covariance matrix $\tilde{R}_{\hat{s}}$, and the $c \times c$ true multi-core scalar covariance matrix $\tilde{R}_s$. The orientation vector ψ is defined as:

$$\psi = \begin{pmatrix} \overline{\eta}_1 & 0 & \cdots & 0 \\ 0 & \overline{\eta}_2 & \cdots & 0 \\ \vdots & \vdots & \ddots & \vdots \\ 0 & 0 & \cdots & \overline{\eta}_c \end{pmatrix} \tag{36}$$

The estimated pair-wise correlation $\hat{\chi}_{ij}$ and the noise-corrected pair-wise power correlation χ_{ij} between the ith and jth sources are given by:

$$\hat{\chi}_{ij} = \frac{\tilde{R}_{\hat{s}}(i,j)^2}{\tilde{R}_{\hat{s}}(i,i)\tilde{R}_{\hat{s}}(j,j)} \tag{37}$$

$$\chi_{ij} = \frac{\tilde{R}_s(i,j)^2}{\tilde{R}_s(i,i)\tilde{R}_s(j,j)} \tag{38}$$

Amplitude correlation can be computed as the square root of Eqs. (37) and (38). The formulation of the MCBF is similar to that of the NB and CSSM except that instead of deriving the beamformer weight for only one source of interest at a time, the MCBF applies additional constraints to simultaneously find weights for all modeled sources (Dalal et al., 2006; Hui and Leahy, 2006; Hui et al., 2010; Quuran and Cheyne, 2010). This feature allows correlation reconstruction of multiple interfering sources at the same time. The MCBF requires three degrees of freedom for spatial location and two degrees of freedom for orientation per core. Theoretically, if all signals from m sensors are linearly independent and signal-related (achieved at infinite SNR), the MCBF can model a maximum of $m/5$ sources. However, at the typical SNR of real measurements recorded on a modern MEG system, the number of signal-related independent spatial modes is approximately 40–50, allowing the MCBF to model a maximum of 8–10 sources. The MCBF is most appropriately used to determine source activity for a given set of sources that already have been accurately localized by methods utilizing a metric such as the DCBF pseudo-Z-score (Diwakar et al., 2011).

General setup for simulations

To measure the performance of the eDCBF spatial filter for both correlation and temporal reconstruction, a series of computer simulations was conducted with a simulator designed to allow variation of the sources present (number, location and orientation) and their corresponding waveforms (frequency, amplitude, lag, duration and SNR), thereby providing vast flexibility for simulation execution.

The source space was simulated with a grid covering the cortical gray matter with homogenous 5 mm spacing in the x, y, and z directions. The cortical boundaries were obtained from a healthy subject's T1-weighted anatomical MRI. The sensor configuration was based on the Elekta/Neuromag™ whole-head MEG system (Vector-View), in which 306 sensors are arranged on a helmet-shaped surface (204 gradiometers and 102 magnetometers). The source-sensor configuration is shown in Fig. 1 (inner-skull surface represented by gray mesh).

To compute the forward model, the boundary element method (BEM) was employed where the inner-skull surface (from MRI) served as the BEM mesh (size 5 mm). SNR levels were adjusted by adding uncorrelated random Gaussian noise to the sensor waveforms, where the SNR was defined as the ratio of the Frobenius norm of the signal vector to that of the noise vector calculated over the interval with signal. Using the simulator, eDCBF correlation and time course reconstruction were inspected over varying source coherence, SNRs, and temporal dynamics. Additional simulations were designed to test the eDCBF at various source separations as well as to investigate correlation estimation for the three-core MCBF.

Setup for SNR, correlation, and time course simulations

Two source dipoles were placed in the left and right hemisphere auditory cortices (Fig. 1). Their signals were composed of a 6-second inactive period followed by 6 s of a sinusoidal wave with amplitude of 5 nAm and frequency of 30 Hz (sampling rate 1000 Hz). The phase shift of the second source was varied from 0° to 90° in steps of 10° to test a wide range of correlations. Reconstruction of the estimated correlation and the noise-corrected correlation was carried out at SNRs of 4, 2, 1, 0.5, 0.25, and 0.167. Estimation of source amplitudes was carried out by FFT examination of extended length (50×) source time course reconstructions over all phase lags and SNRs. To test time course recovery of a more complicated signal, a linear chirp was utilized, wherein the frequency was varied from 5 to 10 Hz (and back) over a period of 5 s and the amplitude was modulated by a 0.1 Hz sinusoid. Noise-corrected correlation was computed for all SNRs and for source time lags of 0.05, 0.1, 0.4 and 1 s. Source time courses and RMS amplitudes were calculated at all time lags and at an SNR of 4. Finally, Monte Carlo methods were employed to properly quantify the results' probability distribution (1000 simulations unless otherwise noted).

Setup for location simulations

To test eDCBF reconstruction at varying source locations, the sinusoidal simulation from the previous section was performed for two additional sets of sources. Noise-corrected correlation values were computed for distantly-placed sources in the left and right

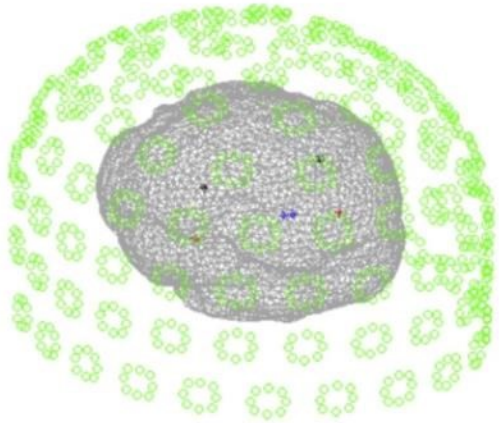

Fig. 1. Source and sensor model. Green—MEG sensor groups. Blue—posterior cingulate cortex dipoles. Black—motor cortex dipoles. Red—auditory cortex dipoles. (For interpretation of the references to colour in this figure legend, the reader is referred to the web version of this article.)

hemisphere primary motor cortices with a separation of 70 mm and for closely-placed sources in the left and right posterior cingulate cortices (PCC) with a separation of 5 mm (Fig. 1). A set of 1000 randomly chosen source pairs was also tested for noise-corrected correlation accuracy at a fixed SNR of 4.

Setup for three-core MCBF simulation

An additional simulation was designed to test MCBF performance for a core size of three. Sources were placed in the PCC and the left and right primary motor cortices. The right motor cortex source's phase lag ranged from 45° to 90° (in steps of 5°) whereas the PCC source's phase lag decreased from 45° to 0° (in steps of 5°), creating a variety of correlation conditions. The simulation was executed 1000 times to compute the noise-corrected correlation for the full SNR and correlation ranges.

Setup for human MEG auditory study

A stereo auditory test stimulus was designed to compare eDCBF correlation and time course reconstruction in actual MEG measurements (200 epochs of evoked responses) to reconstruction using two-dipole fit, a method known to adequately represent neuronal activity in the auditory cortices (Mosher et al., 1992; Mosher and Leahy, 1998; Mosher et al., 1999; Huang et al., 1998). The test sound file consisted of 1800 ms of pre-stimulus silence followed by a 2000 ms stereo stimulus period. The stimulus consisted of a 500-Hz pure tone with a 40-Hz envelope modulated at 100% level. The modulation envelopes between the left and right channels were designed to be fully correlated. The intensities of the left and right channels were balanced for equal sensitivity for the left and right ears. The start and end of the stimulus epochs were smoothed with a cosine roll-off to prevent any artifacts. Magnetic fields evoked by auditory stimulation were measured using an Elekta/Neuromag™ whole-head MEG system (VectorView) with 204 gradiometers and 102 magnetometers in a magnetically shielded room (IMEDCO-AG, Switzerland). EOG electrodes were used to detect eye blinks and eye movements.

Intervals of 1400 ms of post-stimulus data and 200 ms of pre-stimulus data were used for analysis. Data were sampled at 1000 Hz and processed by MaxFilter to remove environment noise (Taulu et al., 2004; Taulu and Simola, 2006; Song et al., 2008; Song et al., 2009). Artifact-free MEG responses ($n = 181$) were averaged with respect to the stimulus trigger. A BEM mesh of 5-mm size for the subject was generated from the inner-skull surface using a set of T1-weighted MRI images taken on a 1.5 T MRI scanner. Registration of MRI and MEG was performed using data obtained from the Polhemus Isotrak system prior to MEG scanning.

Reconstructions of MEG auditory recordings with the eDCBF, SBF, and dipole-fit modeling were compared to assess the accuracy and validity of the eDCBF reconstruction. SVD was used to separate the original sensor measurements into signal and noise components. The top eight singular modes were chosen as a conservative estimate of the noise-free signal based on manual inspection of the elbow-shaped region of the singular value spectrum. The remaining singular modes were considered to contain only the noise-related signal. The noise components were removed and replaced with white noise of the same power, resulting in an estimated SNR of 3.7 and allowing construction of a noise covariance matrix. A regularization parameter equal to 4% of the largest eigenvalue of R_b was used for reconstruction with both the eDCBF and the vector SBF (Van Veen et al., 1997; Sekihara et al., 2002; Sekihara et al., 2004).

Dual-source localization was performed with a Nelder–Mead downhill simplex search for the maximum power pseudo-Z-score. The eDCBF regularized beamformer weight W_d^r was computed and used with Eqs. (24), (21), and (19) to generate unfiltered and low-pass filtered (<50 Hz) regularized time courses for each source. Inter-hemispheric correlation values were computed from filtered time courses, from the source covariance matrix presented in Eq. (22), and from the noise-corrected source covariance matrix. Vector-based SBF was also used to reconstruct unfiltered and filtered regularized time courses for the source locations identified by the eDCBF. Inter-hemispheric correlations were computed with the reconstructed filtered regularized SBF time courses for comparison.

Localization was also performed using a multi-start downhill simplex dipole-fit algorithm with a spherical head model (Huang et al., 1998). The fitted locations were further refined with a BEM forward model. The dipole-fit source time course reconstruction was obtained by multiplying the pseudo-inverse of the gain matrix for the fitted dipoles and the sensor measurements. Inter-hemispheric correlations were computed with unfiltered and low-pass filtered dipole-fit source time courses (<50 Hz). Correlations were also computed between filtered regularized reconstructions (eDCBF and SBF) and filtered time courses obtained from dipole fit as a measure of time course similarity.

Results

Analysis of eDCBF across entire correlation range

To test the performance of eDCBF across the entire range of possible correlations, a phase lag was introduced to the sinusoid of the second source. The simulation was performed with an SNR of 4, minimizing noise effects so that the eDCBF's sensitivity to correlation was emphasized. Source reconstruction was completed using estimated correlation reconstruction. Table 1 shows that eDCBF estimates of the sources' time course correlations are highly accurate ($\varepsilon < 0.003$, $\sigma \leq 0.0013$, where ε is the error, and σ is the standard deviation across Monte Carlo iterations) regardless of the actual value of the correlation. In addition, the low standard deviation demonstrates eDCBF's exceptional stability. Accuracy of source localization was not examined here, as it was already confirmed with the original DCBF (Diwakar et al., 2011).

Examination of eDCBF performance across SNR range

Real-world noise commonly dominates the underlying signal, frequently posing a problem for beamformers. Therefore, we characterized eDCBF performance across a range of SNR values. The following simulation allowed comparison of the estimated and noise-corrected correlation reconstruction from Eqs. (20) and (31). We observed that even though the estimated correlation works well initially, as SNR drops below 1, the accuracy of eDCBF estimated correlations fell to unacceptable levels. By a SNR level of 0.167, the filter became practically ineffective and was unable to appropriately resolve the underlying signal ($\bar{\varepsilon} < 0.32$), where $\bar{\varepsilon}$ is the averaged correlation error over all phase shifts for a given SNR. From the noise time courses (added to sensor waveforms to create the desired SNR), an unbiased

Table 1
Estimated correlation reconstruction for auditory dipoles (SNR = 4). Correlation averages and standard deviations determined using 1000 Monte Carlo simulations.

θ Shift	χ (actual)	χ (estimated)	σ
0°	1.000	0.997	3.83E-05
10°	0.970	0.967	1.96E-04
20°	0.883	0.881	4.44E-04
30°	0.750	0.748	7.96E-04
40°	0.587	0.585	1.03E-03
50°	0.413	0.412	1.22E-03
60°	0.250	0.250	1.21E-03
70°	0.117	0.117	9.85E-04
80°	0.030	0.030	5.47E-04
90°	0.000	0.000	1.07E-04

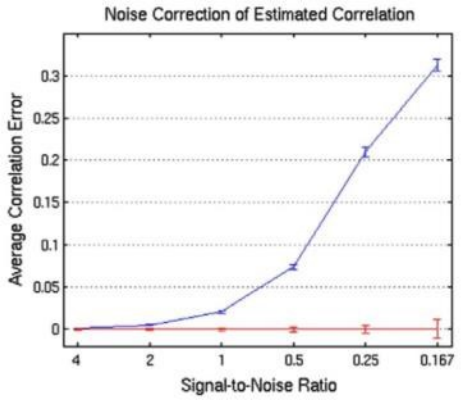

Fig. 2. Estimated (blue) and noise-corrected (red) correlation reconstruction errors and standard deviations (error bars) for auditory dipoles. Correlation values determined using 1000 Monte Carlo simulations. (For interpretation of the references to colour in this figure legend, the reader is referred to the web version of this article.)

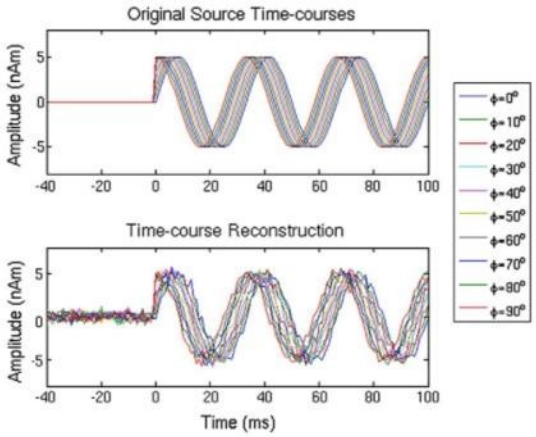

Fig. 4. Sinusoidal time course reconstruction at phase shifts ranging from 0 to 90°. Top panel—simulated source waveforms. Bottom panel—eDCBF time courses.

estimate of the noise covariance matrix was used to examine the noise-corrected correlation. The correction allowed the beamformer to perform successfully at the entire range of SNR and correlation values ($\varepsilon < 0.0008, \bar{\sigma} < 0.011$), where $\bar{\sigma}$ is the averaged Monte Carlo standard deviation across all phase shifts in a given SNR (Fig. 2), rendering eDCBF an extremely robust and flexible beamformer filter given a reasonably accurate estimation of the noise covariance.

Validation of eDCBF performance regardless of source location

The sensitivity of the eDCBF filter to the location of the two sources was investigated by examining three cases: a pair of distantly-spaced dipoles, a pair of closely spaced dipoles, and a pair of randomly placed dipoles. For distant dipoles, we observed that the correlation reconstruction worked precisely throughout the entire SNR and correlation ranges ($\bar{\varepsilon} < 0.0005, \bar{\sigma} < 0.009$). When dipoles were closely placed (PCC dipoles spaced only 5 mm apart), a hindrance for beamformer operation at low SNR, the eDCBF still performed effectively. At SNRs at or above 0.5, the eDCBF was reasonably accurate ($\bar{\varepsilon} < 0.005, \bar{\sigma} < 0.036$), while at SNRs of 0.25 or lower it slightly overestimated the correlation value ($\bar{\varepsilon} < 0.027, \bar{\sigma} < 0.11$)due to bias in the noise covariance estimate at very low SNRs (Fig. 3). Finally, the eDCBF filter still performed accurately when dipole pairs were chosen randomly ($\varepsilon < 0.0002$, $\sigma < 0.003$).

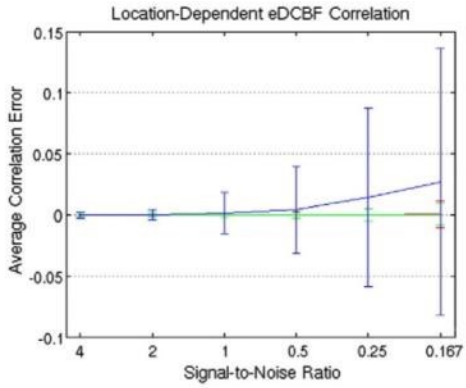

Fig. 3. Noise-corrected correlation reconstruction errors and standard deviations (error bars) for auditory cortex (red), motor cortex (green), and posterior cingulate cortex (blue) dipoles. Correlation values determined using 1000 Monte Carlo simulations. (For interpretation of the references to colour in this figure legend, the reader is referred to the web version of this article.)

Time course reconstruction — sinusoid/chirp source waveforms

For most of the simulations, a sinusoid wave was used to construct the source signal. To investigate the precision of the reconstructed waveform, we examined the accuracy of the reconstructed amplitude as the SNR and phase lag were varied, which is another concern associated with previous dual beamformers. Fig. 4 shows a set of reconstructed waveforms (for the entire range of phase shifts) at SNR of 4 computed from Eq. (19). As shown in Table 2, eDCBF reconstructed the amplitude with the same success regardless of SNR or correlation value, underestimating by more than 1% only in a single case. The small bias in amplitude estimation occurs due to a rank deficient sensor covariance matrix before the addition of noise. Amplitudes estimated from the eDCBF were far more accurate than those from the previous DCBF, which were suppressed by an average of 12.5% (Diwakar et al., 2011).

Since neuronal signals typically contain complex features, a more sophisticated waveform in the form of a linear chirp was also considered. To simulate various correlations, a series of time lags were introduced to the chirp present in the second source. Fig. 5 shows an example of the reconstructed waveform for a one-second time lag at a SNR of 4 for the sensor waveforms. To quantitatively asses the reconstruction, an RMS amplitude measure was employed. When comparing the original

Table 2
Amplitude values for left auditory cortex dipole (results equivalent for right dipole). Amplitude values determined using 100 Monte Carlo simulations.

θ shift	χ (actual)	SNR				
		4	2	1	0.5	0.25
		Amplitude				
0°	1.000	4.99	4.99	4.99	4.99	4.99
10°	0.970	4.99	5.00	4.99	4.99	4.99
20°	0.883	4.99	4.99	5.00	4.99	4.99
30°	0.750	4.99	5.00	5.00	4.99	4.99
40°	0.587	4.99	4.99	4.99	4.99	4.99
50°	0.413	4.99	4.99	5.00	4.99	4.99
60°	0.250	4.99	4.99	5.00	4.99	4.98
70°	0.117	4.99	5.00	4.99	4.99	4.98
80°	0.030	4.99	4.99	4.99	4.99	4.97
90°	0.000	4.99	4.99	4.99	4.99	4.93

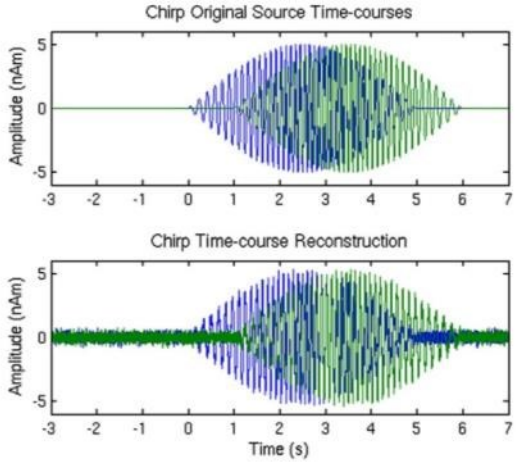

Fig. 5. Chirp time course reconstruction at 1 s time lag. Top panel—original source waveforms. Bottom panel—eDCBF time courses. Blue—left auditory cortex. Green—right auditory cortex. (For interpretation of the references to colour in this figure legend, the reader is referred to the web version of this article.)

waveform's amplitude with the reconstructed waveform (for the example above), it was accurate to 99.9%. The accuracy of the correlation computation was also tested (1000 Monte Carlo simulations). Fig. 6 shows that the eDCBF successfully estimates the correlation for any combination of SNR and time lag($\bar{\varepsilon} < 0.0004, \bar{\sigma} < 0.007$).

Three-source simulation with MCBF

The last simulation examined the performance of the MCBF filter when reconstructing three simultaneously-active correlated sources. Currently, no beamformer method is able to properly address this issue. MCBF performance in reconstructing the source correlation values for all three dipole combinations can be seen in Fig. 7. For any given condition, MCBF properly reconstructed all correlation values ($\bar{\varepsilon} < 0.005, \bar{\sigma} < 0.04$).

Human auditory reconstruction results

The two-dipole-fit reconstruction of the evoked MEG auditory response to the 500-Hz pure tone with a 40-Hz envelope (Fig. 8)

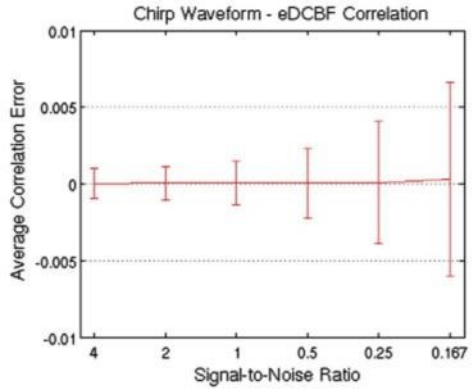

Fig. 6. Noise-corrected correlation reconstruction errors and standard deviations (error bars) for chirp waveforms at different time lags. Correlation values determined using 1000 Monte Carlo simulations.

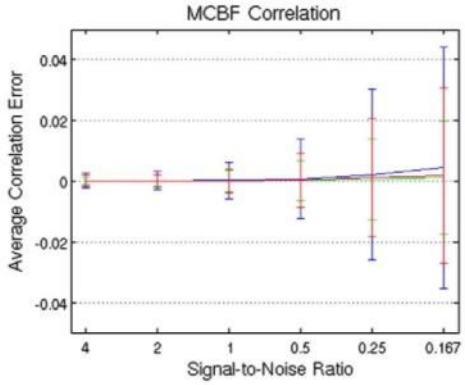

Fig. 7. Pair-wise three-core MCBF noise-corrected correlation reconstruction errors and standard deviations (error bars). Blue—left motor cortex and posterior cingulate cortex. Green—left motor cortex and right motor cortex. Red—right motor cortex and posterior cingulate cortex. Correlation values determined using 1000 Monte Carlo simulations. (For interpretation of the references to colour in this figure legend, the reader is referred to the web version of this article.)

showed bilateral activation of both the left and right auditory cortices. The left hemisphere neuronal source (blue) showed a large transient response followed by a steady-state response with a weak 40-Hz component. The right hemisphere neuronal source (green) revealed a slightly smaller transient response with strong 40-Hz steady-state oscillations from 500 ms to 1400 ms.

During eDCBF reconstruction of the auditory response, maximizing the power pseudo-Z-score (Eq. (34)) appropriately localized sources to the left and right auditory cortices (Fig. 9). Though the K-related pseudo-Z-score provides a valid method of localization at low SNRs as shown previously (Diwakar et al., 2011), its spatial distribution at high SNR is sharply peaked, rendering it unsuitable for grid spacing of a few millimeters. However, the power pseudo-Z-score provides a suitable measure of detection for high SNR recordings (Fig. 10). Localization of the auditory response found by dipole fit and the eDCBF differed by less than 2.5 mm for each hemisphere (Fig. 9).

The eDCBF regularized recovery of source time courses (Fig. 11—left panels) showed individual signals for the left (blue) and right (green) hemisphere neuronal sources. Furthermore, examination of both right and left source signals showed well-defined transient and steady-state

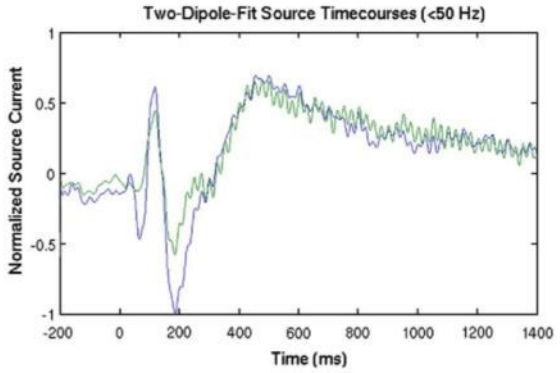

Fig. 8. Normalized dipole-fit source time course reconstruction. Reconstruction of time courses shows a transient and steady-state response in both left (blue) and right (green) auditory cortices. The left transient response is higher in amplitude, while the right 40-Hz steady-state oscillations are more pronounced. (For interpretation of the references to colour in this figure legend, the reader is referred to the web version of this article.)

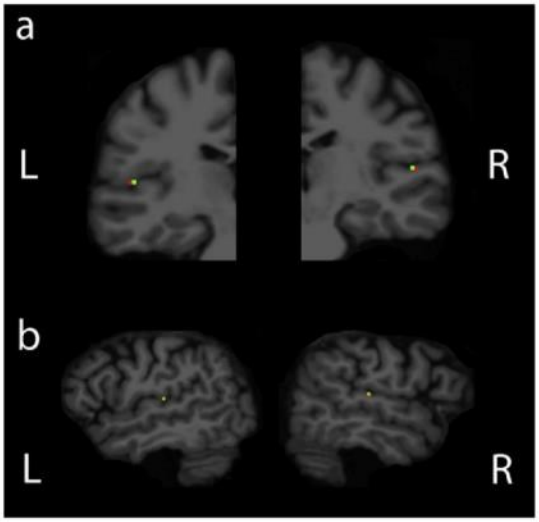

Fig. 9. a) Coronal view of left and right auditory response localizations. b) Sagittal view of left and right auditory response localizations. Green—eDCBF localization. Red—dipole-fit localization. (For interpretation of the references to colour in this figure legend, the reader is referred to the web version of this article.)

responses that closely resembled the time courses obtained from dipole fit as indicated by high correlations ($\chi^a_L = 0.9630$; $\chi^a_R = 0.9614$). In contrast, SBF regularized time courses (Fig. 11—right panels) correlated poorly with those obtained from dipole fit ($\chi^a_L = 0.5018$; $\chi^a_R = 0.4946$). In fact, even features such as the larger, left-sided transient response and the stronger, right-sided 40-Hz steady-state response were preserved with the eDCBF. The errors in the SBF reconstruction were due to inaccurate determination of source orientations and the false assumption that sources are uncorrelated.

Correlations for dipole-fit time courses showed strong coherence between the left and right auditory cortices ($\chi^a = 0.9535$, $\chi^a_{filt} = 0.9567$). The eDCBF noise-corrected correlation ($\chi^a_{reg} = 0.9349$) and the filtered eDCBF correlation ($\hat{\chi}^a_{reg.filt} = 0.9385$) agreed with these values ($\Delta\chi^a < 3\%$). However, the SBF-predicted correlation ($\hat{\chi}^a_{reg.filt} = 0.6119$) was quite poor ($\Delta\chi^a \approx 35\%$). Correlations computed from eDCBF time courses and from the appropriate source covariance matrices were identical.

Discussion

The present study provides an improved implementation of our previously introduced DCBF, which was unable to accurately estimate source amplitudes or produce unique time courses and correlations to characterize source activity (Diwakar et al., 2011). The eDCBF provides a novel approach designed to reconstruct the source power covariance matrix $R_{\hat{s}}$ between multiple sources. With this matrix, individual time courses and correlations for sources can be determined in low SNR conditions, overcoming the deficits of the DCBF.

Computationally, multiple source beamformers (e.g. DSBF, DCBF and eDCBF) require some searching for the optimum source configuration unlike traditional beamformers. Single beamformers may therefore appear more attractive as quick scanning methods but are less accurate due to the strict assumption of non-correlated sources (Robinson and Vrba, 1998; Sekihara et al., 2002; Van Drongelen et al., 1996; Van Veen et al., 1997). Furthermore, unlike beamformer spatial filters that are designed to work in a correlated environment (e.g. NB, CSSM, and AGMN-RUG), the eDCBF requires only a single computation of the weight matrix for accurate correlation determination (Dalal et al., 2006; Hui and Leahy, 2006; Hui et al., 2010; Quuran and Cheyne, 2010; Kumihashi and Sekihara, 2010).

For complex signals, the mathematical formulation of eDCBF flexibly enables examination of correlations in envelopes and frequency bands of interest without too much additional computational load, thereby permitting a more detailed investigation of neuronal communication. Moreover, the eDCBF correlation analysis can be naturally extended to the MCBF spatial filter to account for the presence of multiple correlated sources.

A variety of simulations were conducted to examine the performance of the eDCBF by quantifying the robustness of computed correlations across a range of SNRs (4 to 0.167), source locations, time lags, and waveform shape for two sources. The eDCBF reconstructed correlations with a high degree of accuracy even at a source spacing of only 5 mm. The results also showed that the eDCBF could handle both fully correlated and uncorrelated neuronal sources. Source time course reconstructions resulted in accurate and individual time courses regardless of the degree of correlation between sources. Furthermore, the amplitudes of time courses were accurately reproduced irrespective of the correlation between sources, which is a notable shortcoming of previous dual-beamformer approaches (Brookes et al., 2007; Diwakar et al., 2011). The spatial width of the eDCBF localization peaks using different measures (Z^K and Z^P) under different SNR conditions was also investigated. We observed that

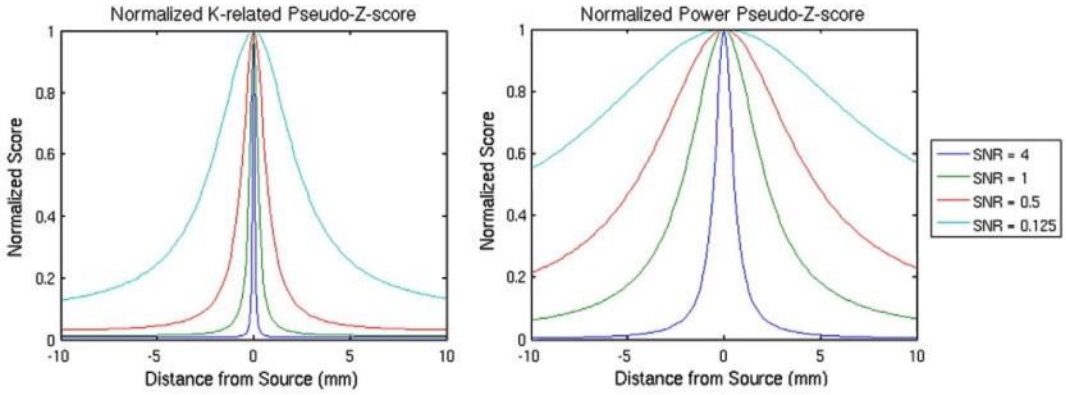

Fig. 10. SNR dependence of pseudo-Z-scores. Left panel—the K-related pseudo-Z-score peaks sharply at high SNR but provides a reasonable profile for localization at lower SNR. Right panel—the power pseudo-Z-score has much broader peaks, providing an appropriate tool for localization in evoked recordings.

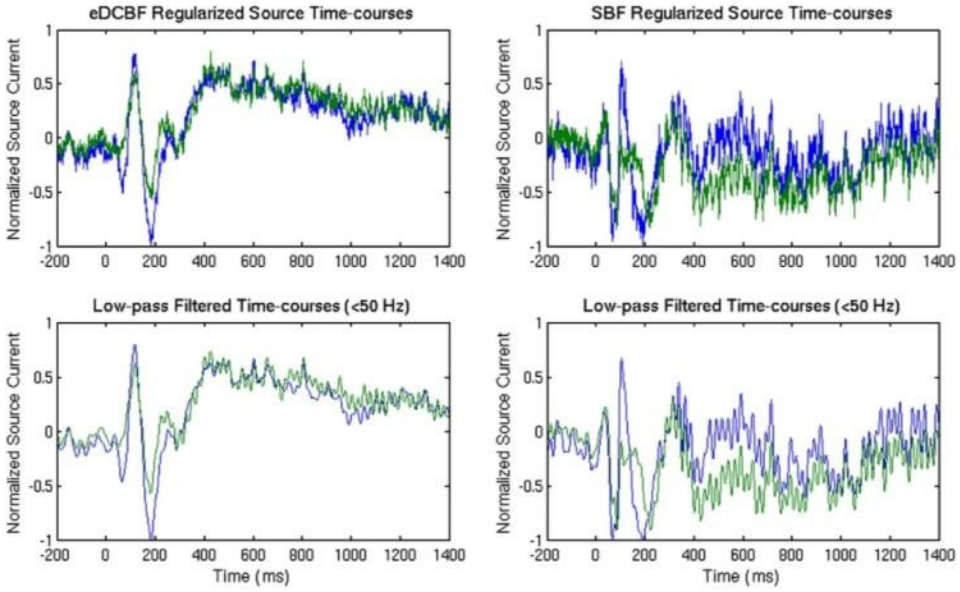

Fig. 11. Normalized eDCBF and SBF source time course reconstruction. eDCBF reconstruction of time courses shows a transient and steady-state response in both left (blue) and right (green) auditory cortices. The left transient response was higher in amplitude while the right steady-state response was more visible. SBF reconstruction of time courses shows distortion and features that are difficult to identify. (For interpretation of the references to colour in this figure legend, the reader is referred to the web version of this article.)

Z^K provides a suitable width for low SNR data while Z^P is preferable for high SNRs.

As a proof of principle, our investigation of the MCBF spatial filter showed accurate correlation reconstruction across a wide variety of source correlations and SNRs in the presence of three correlated sources. In reality, MEG signals can have many active sources. As such, future developments should include an optimization algorithm to determine the proper MCBF core-number to use for reconstruction, which would prevent inaccurate estimation of source activities due to under-modeling. For example, DCBF localization and pseudo-Z-score statistical thresholding can be used to determine MCBF core-number. Furthermore, typical SNR levels for real recordings must be considered, which limits the MCBF core size to 8–10 sources in practice.

We also applied the eDCBF spatial filter to human MEG measurements from a stereo auditory tone paradigm to cross-validate reconstruction performance from our simulations. Localization with the power pseudo-Z-score showed activity in both auditory cortices. The SBF and eDCBF reconstructions were compared to a two-dipole-fit reconstruction. The eDCBF time courses for both right and left hemisphere auditory cortices closely resembled dipole-fit time courses, maintaining both transient and steady-state components of the signal. In contrast, reconstruction with SBF showed malformed and inaccurate time courses. Source localization with eDCBF was used for SBF reconstruction due to the SBF's inability to properly localize correlated neuronal sources (Brookes et al., 2007). Inter-hemispheric correlations computed from eDCBF and dipole-fit estimated time courses were very close; however, the SBF-predicted correlation was underestimated, confirming that the eDCBF offers a more robust reconstruction than the SBF in correlated source environments. Furthermore, strong correlation between eDCBF time courses and dipole-fit results showed that the two methods yield very similar waveforms.

In summary, the present results indicate that the eDCBF spatial filter provides a viable method for exploring complex neuronal networks and their communication, promoting the use of MEG to investigate brain activity.

Acknowledgments

This work was supported in part by a research grant from the McDonnell Foundation via the Brain Trauma Foundation (PI: J. Ghajar, site PIs: R. Lee and M. Huang); by the Department of Veteran Affairs grants to M. Huang (051455 and 060812), R. Lee (E4477-R), and D. Harrington (1IO1CX000146-01 and B501R); by the Office of Naval Research to D. Harrington and T. Liu (N00141010072); and by the National Institutes of Health grants to T. Liu (2R01-NS051661), R. Srinivasan (R01-MH068004), and S. Chien (5-T32 HL-7089-35). The authors also thank Jia Guo for helpful suggestions and discussion. In addition, the authors would like to thank the reviewers for helpful and constructive suggestions that substantially strengthened this work.

References

Brookes, M.J., Stevenson, C.M., Barnes, G.R., Hillebrand, A., Simpson, M.I.G., Francis, S.T., Morris, P.G., 2007. Beamformer reconstruction of correlated sources using a modified source model. NeuroImage 34, 1454–1465.

Dalal, S.S., Sekihara, K., Nagarajan, S.S., 2006. Modified beamformers for coherent source region suppression. IEEE Trans. Biomed. Eng. 53, 1357–1363.

Diwakar, M., Huang, M.X., Srinivasan, R., Harrington, D.L., Robb, A., Angeles, A., Muzzatti, L., Pakdaman, R., Song, T., Theilmann, R.J., Lee, R.R., 2011. Dual-core beamformer for obtaining highly correlated neuronal networks in MEG. NeuroImage 54, 253–263.

Hamalainen, M.S., Ilmoniemi, R.J., 1994. Interpreting magnetic fields of the brain: minimum norm estimates. Med. Biol. Eng. Comput. 32, 35–42.

Hillebrand, A., Singh, K.D., Holliday, I.E., Furlong, P.L., Barnes, G.R., 2005. A new approach to neuroimaging with magnetoencephalography. Hum. Brain Mapp. 25, 199–211.

Huang, M., Aine, C.J., Supek, S., Best, E., Ranken, D., Flynn, E.R., 1998. Multistart downhill simplex method for spatio-temporal source localization in magnetoencephalography. Electroencephalogr. Clin. Neurophysiol. 108, 32–44.

Huang, M., Dale, A.M., Song, T., Halgren, E., Harrington, D.L., Podgorny, I., Canive, J.M., Lewis, S., Lee, R.R., 2006. Vector-based spatial–temporal minimum L1-norm solution for MEG. NeuroImage 31, 1025–1037.

Hui, H.B., Leahy, R.M., 2006. Linearly constrained MEG beamformers for MVAR modeling of cortical interactions. 3rd IEEE International Symposium on Biomedical Imaging: Nano to Macro, 2006, pp. 237–240.

Hui, H.B., Pantazis, D., Bressler, S.L., Leahy, R.M., 2010. Identifying true cortical interactions in MEG using the nulling beamformer. NeuroImage 49, 3161–3174.

Kumihashi, I., Sekihara, K., 2010. Array-gain constraint minimum-norm spatial filter with recursively updated gram matrix for biomagnetic source imaging. IEEE Trans. Biomed. Eng. 57, 1358–1365.
Mosher, J.C., Leahy, R.M., 1998. Recursive MUSIC: a framework for EEG and MEG source localization. IEEE Trans. Biomed. Eng. 45, 1342–1354.
Mosher, J.C., Lewis, P.S., Leahy, R.M., 1992. Multiple dipole modeling and localization from spatio-temporal MEG data. IEEE Trans. Biomed. Eng. 39, 541–557.
Mosher, J.C., Baillet, S., Leahy, R.M., 1999. EEG source localization and imaging using multiple signal classification approaches. J. Clin. Neurophsiol. 16, 225–238.
Quuran, M.A., Cheyne, D., 2010. Reconstruction of correlated brain activity with adaptive spatial filters in MEG. NeuroImage 49, 2387–2400.
Robinson, S., Vrba, J., 1998. Functional neuroimaging by synthetic aperture magnetometry. In: Yoshimoto, T., Kotani, M., Kuriki, S., Karibe, H., Nakasato, N. (Eds.), Recent Advances in Biomagnetism. Tohoku Univ. Press, Sendai, pp. 302–305.
Sekihara, K., Nagarajan, S., Poeppel, D., Marantz, A., 2002. Performance of an MEG adaptive-beamformer technique in the presence of correlated neural activities: effects on signal intensity and time course estimates. IEEE Trans. Biomed. Eng. 49 (12), 1534–1546.
Sekihara, K., Nagarajan, S., Poeppel, D., Marantz, A., 2004. Asymptotic SNR of scalar and vector minimum-variance beamformers for neuromagnetic source reconstruction. IEEE Trans. Biomed. Eng. 51 (10), 1726–1733.
Song, T., Gaa, K., Cui, L., Feffer, L., Lee, R.R., Huang, M.X., 2008. Evaluation of signal space separation via simulation. Med. Biol. Eng. Comput. 46, 923–932.
Song, T., Cui, L., Gaa, K., Feffer, L., Taulu, S., Lee, R.R., Huang, M.X., 2009. Signal space separation algorithm and its application on suppressing artifacts caused by vagus nerve stimulation for magnetoencephalography recordings. J. Clin. Neurophysiol. 26 (6), 392–400.
Spencer, M.E., Leahy, R.M., Mosher, J.C., Lewis, P.S., 1992. Adaptive filters for monitoring localized brain activity from surface potential time series. Conf. Record for 26th Annu. Asilomer Conf. Signals, Systems, and Computers, pp. 156–161.
Taulu, S., Simola, J., 2006. Spatiotemporal signal space separation method for rejecting nearby interference in MEG measurements. Phys. Med. Biol. 51, 1759–1768.
Taulu, S., Kajola, M., Simola, J., 2004. Suppression of interference and artifacts by the signal space separation method. Brain Topogr. 16, 269–275.
Van Drongelen, W., Yuchtman, M., Van Veen, B.D., Van Huffelen, A.C., 1996. A spatial filtering technique to detect and localize multiple sources in the brain. Brain Topogr. 9 (1), 39–49.
Van Veen, B.D., Van Drognelen, W., Yuchtman, M., Suzuku, A., 1997. Localisation of brain electrical activity via linearly constrained minimum variance spatial filtering. IEEE Trans. Biomed. Eng. 44 (9).
Vrba, J., Robinson, S.E., 2001. Signal processing in magnetoencephalography. Methods 25 (2), 249–271.

Acknowledgements

Chapter 2, in full, is a reprint of the material as it appears in Neuroimage 2011. Diwakar, Mithun; Tal, Omer; Liu, Thomas T.; Harrington, Deborah L.; Srinivasan, Ramesh; Muzzatti, Laura; Song, Tao; Theilmann, Rebecca J.; Lee, Ronald R.; Huang, Ming-Xiong (2011). Accurate reconstruction of temporal correlation for neuronal sources using the enhanced dual-core MEG beamformer. NeuroImage 56: 1918-28. The dissertation author was a primary investigator and a co-author of this paper.

CHAPTER 3

Abstract

Adaptive spatial filters (beamformers) have been widely used to reconstruct source activity for biomagnetic measurements recorded by magnetoencephalography (MEG) and assess whole-brain connectivity, yet still contain certain limitations. Most notably, the *conventional single beamformer* (SBF) has difficulty detecting neuronal sources with correlated time-courses, resulting in the misestimation of source amplitudes and time-courses. Furthermore, signal leakage typical of the SBF strongly affects the spatial extents of the estimated sources, limiting the ability to accurately evaluate MEG functional connectivity. The recently introduced *multi-core beamformer* (MCBF) addressed the issue of source correlation, yet a solution required source locations to be known. In this chapter, we introduce an iterative algorithm that when integrated with the *multi-core beamformer* (MCBF) mathematical framework enables accurate source localization without any *a priori* information. Furthermore, combining MCBF together with the iterative approach results in substantial minimization of the signal leakage distortion and other spatial biases common to beamformers. The proposed MCBF solution also ultimately provides voxel-by-voxel source activity estimates thereby enabling whole-brain functional connectivity analyses of MEG evoked and spontaneous data (allowing the characterization of MEG resting-state networks). Performance of the approach was validated and compared to that of the SBF by means of simulated waveforms designed to resemble spontaneous MEG signals as well as real neuromagnetic measurements recorded during an evoked task.

Introduction

Magnetoencephalography (MEG) is a functional neuroimaging modality capable of detecting neural activity with millisecond temporal resolution and high spatial accuracy. The magnetic field distribution at the sensors can be accurately predicted using the quasi-static approximation to the Maxwell Field Equations (forward model) if the neural current distribution and head geometry are known. However, if no additional constraints are imposed, the ability to determine a neural source distribution given a set of sensor measurements (inverse model) is ill-defined and non-unique (i.e. different source distributions yield the same sensor waveforms) (Hamalainen and Ilmoniemi, 1994). Due to the underdetermined nature of the inverse problem, different techniques have been proposed as a means of generating viable solutions.

Adaptive spatial filters (beamformers), which utilize the minimum-variance constraint, are a popular choice for source-space projection. Most commonly used is the *conventional single beamformer* (SBF), which is capable of generating time-courses and power estimates on a voxel-by-voxel basis with high spatial accuracy even under poor signal-to-noise ratio (SNR) conditions (Robinson, 1998; Sekihara et al., 2002; Van Drongelen, 1996; Van Veen et al., 1997). However, SBF reconstructions are susceptible to inter-source correlations, resulting in amplitude suppression and time-course distortion (Sekihara, 2008). Considering that spontaneous and non-averaged task related (e.g. eye tracking) neural activity is known to involve synchronous communication between multiple sources (Singer, 1999), the SBF may not be optimal for analyzing complex, highly coordinated brain activity (Moiseev and Herdman, 2013).

A number of modifications to the SBF have been proposed to address its susceptibility to source correlation, most notably the *nulling beamformer* (NB) and the *coherent source suppression model* (CSSM). Both utilize additional constraints to null out interference from correlated sources and ensure proper recovery of the source of interest. However, the locations of these obstructing sources must be determined *a priori* for these techniques to successfully constrain the problem (Dalal et al., 2006; Hui and Leahy, 2006; Hui et al., 2010; Quraan and Cheyne, 2010), thus limiting their practical use as source locations are normally unknown in spontaneous or non-averaged task-related recordings. Another approach introduced by Brookes et al. (2007) handles the presence of correlated sources by redesigning the spatial filter to reconstruct the signals from two sources simultaneously. Although the *dual-source beamformer* (DSBF) is capable of localizing temporally synchronous yet spatially distant activity, it is computationally expensive, requiring lengthy non-linear searches to determine source orientations, locations, and weightings (Brookes et al., 2007).

The DSBF was later reformulated by Diwakar et al. (2011a) as a vector beamformer, termed the *dual-core beamformer* (DCBF), thereby greatly reducing computational expense by removing the need for non-linear searches of source orientations and weightings (Diwakar et al., 2011a). Another major advantage of the DCBF (and DSBF) over the NB and CSSM techniques, is its ability to accurately localize activity without any *a priori* information. However, the source time-courses generated by the DCBF are simply scaled replicas of each other (i.e. non-unique), precluding any type of functional connectivity (FC) analyses (Brookes et al., 2007; Diwakar et al., 2011a). Addressing DCBF's shortcomings, the *enhanced dual-core beamformer* (eDCBF)

allowed determination of unique source time-courses, thus permitting accurate source-to-source correlation analyses (Diwakar et al., 2011b). Reconstructions of auditory evoked recordings with the eDCBF demonstrated its capability to produce high-fidelity solutions with real data. An extension of the eDCBF was also introduced, dubbed the *multi-core beamformer* (MCBF), to help process data that contained more than two correlated sources. Unfortunately, the increase in dimensionality with the MCBF is associated with a considerable increase in the computational cost of source localization (Diwakar et al., 2011b).

Recent work by Moiseev et al. (2011) focused on developing an iterative localization search algorithm for the *multiple constrained minimum variance beamformer* (MCMV), a modified multi-source beamformer similar to the eDCBF and MCBF. The technique essentially finds the solution without requiring *a priori* knowledge by iteratively determining the source locations using a novel unbiased localizer. Although an important and fundamental first step in the field of multi-source localization, this "bottom-up" approach is inherently challenged, as any correlation of yet to be discovered sources would still distort and interfere with per iteration activity estimates, especially as SNR weakens (Moiseev et al., 2011). In addition, the number of iterations required for an adequate solution (i.e. the estimated number of interfering sources) is normally not well-defined or available in spontaneous settings. Furthermore, the MCMV and its counterparts (i.e. the eDCBF and MCBF) are limited as source dynamics are estimated only in specified locations, unlike the SBF which generates them for the entire brain thereby enabling whole-brain FC analysis.

In this chapter, we put forward an iterative Bayesian-based localization algorithm for the MCBF that overcomes the intrinsic limitations of previous beamformers. The localization procedure utilizes a "top-down" approach which initially assumes an equal contribution for all voxels (i.e. possible sources) in the brain. An iterative process is then used to update the weighting parameters for each voxel, gradually refining the spatial distribution and temporal dynamics of the underlying sources (without any *a priori* information). Because all locations are simultaneously incorporated into the "top-down" solution, this approach avoids confounds due to interference from "undetected" sources in the "bottom-up" approach. Furthermore, as the procedure provides a solution (time-course) at every voxel, it ultimately enables the MCBF to estimate whole-brain dynamics, a prerequisite for assessment of whole-brain neural connectivity.

Cortical FC analyses of resting-state MEG recordings have traditionally computed correlations between sources utilizing the SBF (Brookes et al., 2011a; Brookes et al., 2011b; Hall et al., 2013; Hillebrand et al., 2012; Hipp et al., 2012; Luckhoo et al., 2012; Mantini et al., 2011; Tal et al., 2013). However, as noted above, the temporal correlation between sources (Singer, 1999) may adversely affect the SBF time-course reconstructions, placing its use as a tool for FC analysis under question (Moiseev and Herdman, 2013). In this section, we look further into the matter and compare the reconstruction performance of the conventional SBF to the newly developed MCBF algorithm using simulations whose source time-course characteristics emulate those of spontaneous MEG signals by taking into account prior electrophysiological knowledge (Brookes et al., 2011b; de Pasquale et al., 2010; Liu et al., 2010; Mantini et al., 2007). We also examine the performance of the two reconstruction techniques with real

neuromagnetic measurements evoked by a unilateral median-nerve stimulation, a task involving intricate interaction between multiple neural regions in the somatosensory system, thus serving as an ideal scenario to study the beamformers' ability to accurately map source activity for complex networks.

Materials and Methods

We begin with a review of the general lead-field model and MCBF mathematics, after which we develop an iterative algorithm to obtain the final MCBF solution for source dynamics. The simulations used to compare the performance of MCBF and SBF are then described.

Review of General Lead-field Model

The general lead-field model provides a mathematical description of the magnetic fields produced by dipolar neuronal currents. Let $\boldsymbol{b}(t)$ be an *m x 1* vector of sensor measurements at time *t*, $\boldsymbol{n}(t)$ be an *m x 1* vector of sensor noise measurements, and $\boldsymbol{s}(t)$ be a *2p x 1* matrix of vector source amplitudes, where *m* is the number of sensors and *p* is the number of pre-defined dipolar sources. Let the lead-field matrix defined for the i^{th} source be denoted by the *m x 2* matrix $\boldsymbol{L}_i = [\boldsymbol{l}_{\theta,i} \quad \boldsymbol{l}_{\phi,i}]$, where the θ and ϕ orientations are determined by the two dominant modes obtained from the singular value decomposition (SVD) of the *m x 3* lead-field matrix for each dipole (Huang et al., 2006). The composite lead-field matrix or gain matrix is defined as the *m x 2p* matrix $\boldsymbol{L} = [\boldsymbol{L}_1 \quad \boldsymbol{L}_2 \quad \boldsymbol{L}_3 \quad \cdots \quad \boldsymbol{L}_p]$. The MEG signal equation can then be written as:

$$\boldsymbol{b}(t) = \boldsymbol{L}\boldsymbol{s}(t) + \boldsymbol{n}(t) \tag{1}$$

Taking the covariance of (1) while assuming that the noise and source signals are uncorrelated, provides the following relationship:

$$\boldsymbol{R}_b = \boldsymbol{L}\boldsymbol{R}_s\boldsymbol{L}^T + \boldsymbol{R}_n \tag{2}$$

where $\boldsymbol{R}_b$ is the *m x m* sensor covariance matrix, $\boldsymbol{R}_s$ is the *2p x 2p* source covariance matrix, and $\boldsymbol{R}_n$ is the *m x m* noise covariance matrix.

Multi-core Beamformer

The multi-core lead-field vector is defined as the *m x 2c* matrix $\boldsymbol{L}_m = [\boldsymbol{L}_1 \quad \boldsymbol{L}_2 \quad \cdots \quad \boldsymbol{L}_c]$, where *c* is the desired number of sources to be modeled. The corresponding multi-core weighting vector is defined as the *m x 2c* matrix $\boldsymbol{W}_m = [\boldsymbol{W}_1 \quad \boldsymbol{W}_2 \quad \cdots \quad \boldsymbol{W}_c]$, designed such that:

$$\hat{\boldsymbol{s}}(t) = \boldsymbol{W}_m^T\boldsymbol{b}(t) \tag{3}$$

where $\hat{\boldsymbol{s}}(t)$ represents the estimated source time-courses. The solution for the multi-core weighting vector, $\boldsymbol{W}_m$, is obtained by computing the minimum variance solution (Diwakar et al., 2011b):

$$\boldsymbol{W}_m = \boldsymbol{R}_b^{-1}\boldsymbol{L}_m(\boldsymbol{L}_m^T\boldsymbol{R}_b^{-1}\boldsymbol{L}_m)^{-1} \tag{4}$$

The MCBF estimated vector covariance matrix $\boldsymbol{R}_{\hat{s}}$ is then given by:

$$\boldsymbol{R}_{\hat{s}} = \boldsymbol{W}_m^T\boldsymbol{R}_b\boldsymbol{W}_m = (\boldsymbol{L}_m^T\boldsymbol{R}_b^{-1}\boldsymbol{L}_m)^{-1} \tag{5}$$

The MCBF estimated source vector covariance matrix $\boldsymbol{R}_{\hat{s}}$ can be expressed as:

$$\boldsymbol{R}_{\hat{s}} = \begin{pmatrix} \langle \hat{s}_1(t)\hat{s}_1(t)\rangle \overline{\boldsymbol{\eta}}_1\overline{\boldsymbol{\eta}}_1^T & \langle \hat{s}_1(t)\hat{s}_2(t)\rangle \overline{\boldsymbol{\eta}}_1\overline{\boldsymbol{\eta}}_2^T & \cdots & \langle \hat{s}_1(t)\hat{s}_c(t)\rangle \overline{\boldsymbol{\eta}}_1\overline{\boldsymbol{\eta}}_c^T \\ \langle \hat{s}_2(t)\hat{s}_1(t)\rangle \overline{\boldsymbol{\eta}}_2\overline{\boldsymbol{\eta}}_1^T & \langle \hat{s}_2(t)\hat{s}_2(t)\rangle \overline{\boldsymbol{\eta}}_2\overline{\boldsymbol{\eta}}_2^T & \cdots & \langle \hat{s}_2(t)\hat{s}_c(t)\rangle \overline{\boldsymbol{\eta}}_2\overline{\boldsymbol{\eta}}_c^T \\ \vdots & \vdots & \ddots & \vdots \\ \langle \hat{s}_c(t)\hat{s}_1(t)\rangle \overline{\boldsymbol{\eta}}_c\overline{\boldsymbol{\eta}}_1^T & \langle \hat{s}_c(t)\hat{s}_2(t)\rangle \overline{\boldsymbol{\eta}}_c\overline{\boldsymbol{\eta}}_2^T & \cdots & \langle \hat{s}_c(t)\hat{s}_c(t)\rangle \overline{\boldsymbol{\eta}}_c\overline{\boldsymbol{\eta}}_c^T \end{pmatrix} \tag{6}$$

where $\hat{s}_i(t)$ are the estimated scalar source time-courses ($\langle\cdot\rangle$ indicates the time average) and $\overline{\boldsymbol{\eta}}_i$ are the *2 x 1* estimated normalized orientation vectors. The diagonal *2 x 2* sub-matrices of $\boldsymbol{R}_{\hat{s}}$ are of the same form as the SBF vector covariance matrices (Sekihara et

al., 2004). Thus, source power estimates can be obtained by simply computing the trace of the respective diagonal submatrix (Diwakar et al., 2011b).

The MCBF solution, as formulated above, can only be obtained if the positions of the sources are known, rendering it possible to obtain $\boldsymbol{L}_m$. Since the position of active sources is generally an unknown parameter, the MCBF weight formulated in (4) will be hereafter referred to as the optimal MCBF solution.

Generalized MCBF Solution:

The MCBF solution for the weighting vector presented in (4) is valid only when all sources contributing to the MEG signal are specified in the core. This introduces two challenges: 1) the locations of the sources must be known and 2) the size of the subspace spanned by the MEG measurements places a practical limit on the number of sources specified by the MCBF weights. If the latter limitation did not exist, one could include all dipoles in the MCBF core. Substituting the full gain matrix $\boldsymbol{L}$ for $\boldsymbol{L}_m$ in Equation (4) yields the solution for the MCBF beamformer weight for all sources ($\boldsymbol{W}$):

$$\boldsymbol{W} = \boldsymbol{R}_b^{-1}\boldsymbol{L}\boldsymbol{Q}^{-1} \tag{7}$$

$$\boldsymbol{Q} = \boldsymbol{L}^T\boldsymbol{R}_b^{-1}\boldsymbol{L} \tag{8}$$

Inversion of the $\boldsymbol{Q}$ matrix in Equation (7), however, cannot be performed, as the matrix is highly singular. Instead, we may use the ranked pseudoinverse of $\boldsymbol{Q}$, denoted $\boldsymbol{Q}^+$where matrix inversion can be carried out using 25-60 modes. Unfortunately, $\boldsymbol{Q}^+$ tends to be a poor estimate of $\boldsymbol{Q}^{-1}$ unless the lead fields are weighted to improve the power of modes with actual signal. This can be done by weighting the lead fields by a function $\boldsymbol{\Gamma}(\boldsymbol{P})$ of source power, defined as a block diagonal matrix of 2*p* x 2*p* hyper-parameters composed of 2 x 2 block matrices along the main diagonal (weights for each source) with the

remaining off-diagonal block matrices equal to zero. The diagonal components of the 2 x 2 sub-matrices allow $\boldsymbol{\Gamma}$ to optimize for source strength, while the off-diagonal components allow optimization of source orientation. We can apply the hyperparameters by substituting $\boldsymbol{L} = \boldsymbol{L\Gamma}$ into equations (7) and (8):

$$\boldsymbol{W} = \boldsymbol{R}_b^{-1}\boldsymbol{L\Gamma Q}^{+} \tag{9}$$

$$\boldsymbol{Q} = \boldsymbol{\Gamma}^T\boldsymbol{L}^T\boldsymbol{R}_b^{-1}\boldsymbol{L\Gamma} \tag{10}$$

This solution is equivalent to solving for MCBF weights with the constraint $\boldsymbol{W}^T\boldsymbol{L\Gamma} = \boldsymbol{I}$ or equivalently, $\boldsymbol{W}^T\boldsymbol{L} = \boldsymbol{\Gamma}^{-1}$. To correct for this deformation (or rescaling) when computing source time-courses, we must multiply $\boldsymbol{W}$ by $\boldsymbol{\Gamma}$. This is the same procedure used to rescale time-courses when using the array-gain constraint (Sekihara, 2008). Source time-courses are therefore given by:

$$\boldsymbol{s}(t) = \boldsymbol{\Gamma}^T\boldsymbol{W}^T\boldsymbol{b}(t) \tag{11}$$

We note then that $\boldsymbol{\Gamma}$ would be in optimal form when all 2 x 2 block matrices along the main diagonal that correspond to locations without sources are equal to zero. In other words, the generalized MCBF solution will be reduced to the optimal MCBF solution when all the columns corresponding to source-free locations in $\boldsymbol{L}$ are fully nulled (i.e. $\boldsymbol{L\Gamma}$ matches $\boldsymbol{L}_m$).

Iterative MCBF Approach

In the iterative MCBF approach, the optimal MCBF solution is estimated by successive refinement of the beamformer weighting matrix using information provided by source amplitude estimates. The refinement of the weighting matrix occurs through optimization of the hyperparameters $\boldsymbol{\Gamma}$. The method of optimizing the hyperparameters is based on Bayesian approaches presented by Friston et al. (2008); Owen et al. (2012);

Wipf and Nagarajan (2009); Wipf et al. (2010); Zumer et al. (2007). We begin by examining the cost function, which provides a means to improve solutions through successive iterations and is defined as:

$$\mathcal{L}(\Gamma) = trace\left[\boldsymbol{R}_b \widehat{\boldsymbol{R}}_b^{-1}\right] + \log\left|\widehat{\boldsymbol{R}}_b\right| \tag{12}$$

where $\widehat{\boldsymbol{R}}_b$ is the per-iteration sensor covariance matrix estimate and is initialized to $\boldsymbol{R}_b$ for the first iteration. The cost function is designed to optimize both sparsity and agreement with the forward model per iteration (Owen et al., 2012; Wipf et al., 2010). In each subsequent iteration, $\widehat{\boldsymbol{R}}_b$ is computed with MCBF source activity estimates (Eqn. 11) and the forward model (Eqn. 2):

$$\widehat{\boldsymbol{R}}_b^{next} = \boldsymbol{L}\widehat{\boldsymbol{\Gamma}}^T\widehat{\boldsymbol{W}}^T\,\overline{\boldsymbol{R}_b}\,\widehat{\boldsymbol{W}}\widehat{\boldsymbol{\Gamma}}\boldsymbol{L}^T + \boldsymbol{R}_n \tag{13}$$

$\widehat{\boldsymbol{W}}$ is the per iteration weighting matrix given by:

$$\widehat{\boldsymbol{W}} = \widehat{\boldsymbol{R}}_b^{-1}\boldsymbol{L}\widehat{\boldsymbol{\Gamma}}\widehat{\boldsymbol{Q}}^{+} \tag{14}$$

$$\widehat{\boldsymbol{Q}} = \widehat{\boldsymbol{\Gamma}}^T\boldsymbol{L}^T\widehat{\boldsymbol{R}}_b^{-1}\boldsymbol{L}\widehat{\boldsymbol{\Gamma}} \tag{15}$$

$\overline{\boldsymbol{R}_b}$ is a rank-reduced version of $\boldsymbol{R}_b$ computed with the same number of modes as $\boldsymbol{Q}^{+}$. Use of $\overline{\boldsymbol{R}_b}$ allows de-noising of the forward model resulting in less noisy estimates of $\widehat{\boldsymbol{R}}_b$ computed per iteration. $\widehat{\boldsymbol{\Gamma}}$**,** the per iteration matrix of hyperparameters, is determined by an update equation described below.

To compute an updated equation for $\widehat{\boldsymbol{\Gamma}}$ we adopt procedures (Owen et al., 2012; Wipf et al., 2010) that construct auxiliary functions using sets of hyperplanes to minimize the cost function. The approach is generic and requires only an estimate of source time-courses ($\boldsymbol{X}$). For our purposes, $\boldsymbol{X}$ is computed with the MCBF solution for source time-courses (11) and is given by:

$$\boldsymbol{X} = \widehat{\boldsymbol{\Gamma}}^T \widehat{\boldsymbol{W}}^T \boldsymbol{b}(t) = \widehat{\boldsymbol{\Gamma}}^T \widehat{\boldsymbol{Q}}^+ \widehat{\boldsymbol{\Gamma}}^T \boldsymbol{L}^T \widehat{\boldsymbol{R}}_b^{-1} \boldsymbol{b}(t) \tag{16}$$

Equation 16 can be re-written by defining $\widehat{\boldsymbol{\Gamma}}' = \widehat{\boldsymbol{\Gamma}} \widehat{\boldsymbol{Q}}^+ \widehat{\boldsymbol{\Gamma}}$ such that:

$$\boldsymbol{X} = \widehat{\boldsymbol{\Gamma}}'^T \boldsymbol{L}^T \widehat{\boldsymbol{R}}_b^{-1} \boldsymbol{b}(t) \tag{17}$$

The solution for the minimizing auxiliary function $\boldsymbol{Z}$ with respect to $\widehat{\boldsymbol{\Gamma}}_i'$ (the 2 x 2 sub-matrix of $\widehat{\boldsymbol{\Gamma}}'$ corresponding to the i^{th} source) is analogous to the expression presented in other studies (Owen et al., 2012; Wipf et al., 2010) and is given by:

$$\boldsymbol{Z}_i = \nabla_{\widehat{\boldsymbol{\Gamma}}_i'} \log \left| \widehat{\boldsymbol{R}}_b \right| = \boldsymbol{L}_i^T \widehat{\boldsymbol{R}}_b^{-1} \boldsymbol{L}_i \tag{18}$$

Empirically, we have found that using $\boldsymbol{R}_b^{-1}$, the regularized inverse of the recorded sensor covariance, in (18) instead of $\widehat{\boldsymbol{R}}_b^{-1}$, the regularized inverse of the estimated sensor covariance, provides more reliable reconstructed time-courses. The update equation for $\widehat{\boldsymbol{\Gamma}}_i'$ (Wipf et al., 2010), assuming it is a positive definite matrix, is then given by :

$$\widehat{\boldsymbol{\Gamma}}_i'^{next} = \boldsymbol{Z}_i^{-\frac{1}{2}} \left(\boldsymbol{Z}_i^{\frac{1}{2}} \boldsymbol{X}_i \boldsymbol{X}_i^T \boldsymbol{Z}_i^{\frac{1}{2}} \right)^{\frac{1}{2}} \boldsymbol{Z}_i^{-\frac{1}{2}} \tag{19}$$

$$\boldsymbol{X}\boldsymbol{X}^T = \widehat{\boldsymbol{\Gamma}}'^T \boldsymbol{L}^T \widehat{\boldsymbol{R}}_b^{-1} \overline{\boldsymbol{R}_b} \widehat{\boldsymbol{R}}_b^{-1} \boldsymbol{L} \widehat{\boldsymbol{\Gamma}}' \tag{20}$$

In practice, it is difficult to find an exact solution for $\widehat{\boldsymbol{\Gamma}}_i^{next}$ given $\widehat{\boldsymbol{\Gamma}}_i'^{next}$. However, we have found that we can estimate $\widehat{\boldsymbol{\Gamma}}_i^{next} \approx \left(\widehat{\boldsymbol{\Gamma}}_i'^{next} \right)^{\frac{1}{2}}$ and still get accurate localization. This approximation is equivalent to assuming that $\widehat{\boldsymbol{Q}}^+$ does not contribute significantly to the diagonal 2 x 2 sub-matrices of $\widehat{\boldsymbol{\Gamma}}'$ (i.e. $\widehat{\boldsymbol{\Gamma}}_i' = \widehat{\boldsymbol{\Gamma}}_i \boldsymbol{Q}_i^+ \widehat{\boldsymbol{\Gamma}}_i \approx \widehat{\boldsymbol{\Gamma}}_i \widehat{\boldsymbol{\Gamma}}_i$).

In summary, we have the following iterative path (variables marked "*next*" are used on the subsequent iteration):

1) Initialize $\widehat{\boldsymbol{\Gamma}} = \boldsymbol{I}$ and $\widehat{\boldsymbol{R}}_b = \boldsymbol{R}_b$

2) Compute $\widehat{\boldsymbol{R}}_b^{-1}$ using the regularized inverse (see equation 21)

3) Compute $\widehat{\boldsymbol{W}}$ using $\widehat{\boldsymbol{W}} = \widehat{\boldsymbol{R}}_b^{-1}\boldsymbol{L}\widehat{\boldsymbol{\Gamma}}\widehat{\boldsymbol{Q}}^{+}$ and $\widehat{\boldsymbol{Q}} = \widehat{\boldsymbol{\Gamma}}^T\boldsymbol{L}^T\widehat{\boldsymbol{R}}_b^{-1}\boldsymbol{L}\widehat{\boldsymbol{\Gamma}}$

4) Compute $\widehat{\boldsymbol{R}}_b^{next}$ using $\widehat{\boldsymbol{R}}_b^{next} = \boldsymbol{R}_n + \boldsymbol{L}\widehat{\boldsymbol{\Gamma}}^T\widehat{\boldsymbol{W}}^T\overline{\boldsymbol{R}_b}\widehat{\boldsymbol{W}}\widehat{\boldsymbol{\Gamma}}\boldsymbol{L}^T$

5) Compute $\widehat{\boldsymbol{\Gamma}}_i'^{next} = \boldsymbol{Z}_i^{-\frac{1}{2}}\left(\boldsymbol{Z}_i^{\frac{1}{2}}\boldsymbol{X}_i\boldsymbol{X}_i^T\boldsymbol{Z}_i^{\frac{1}{2}}\right)^{\frac{1}{2}}\boldsymbol{Z}_i^{-\frac{1}{2}}$ using $\boldsymbol{X}_i\boldsymbol{X}_i^T = \widehat{\boldsymbol{\Gamma}}_i^T\widehat{\boldsymbol{W}}_i^T\overline{\boldsymbol{R}_b}\widehat{\boldsymbol{W}}_i\widehat{\boldsymbol{\Gamma}}_i$ and $\boldsymbol{Z}_i = \boldsymbol{L}_i^T\boldsymbol{R}_b^{-1}\boldsymbol{L}_i$,

6) Compute $\widehat{\boldsymbol{\Gamma}}_i^{next}$ using $\widehat{\boldsymbol{\Gamma}}_i^{next} \approx \left(\widehat{\boldsymbol{\Gamma}}_i'^{next}\right)^{\frac{1}{2}}$

7) Return to step 2

In steps 2 and 5 above, the matrix inverses of $\widehat{\boldsymbol{R}}_b$ and $\boldsymbol{R}_b$ are calculated by applying a regularization constant (γ) determined from the measured sensor covariance (where $\|\boldsymbol{X}\|_F$ indicates the Frobenius norm).

$$\widehat{\boldsymbol{R}}_b^{-1} = \left(\widehat{\boldsymbol{R}}_b + \gamma\boldsymbol{I}\frac{\|\widehat{\boldsymbol{R}}_b\|_F}{\|\boldsymbol{R}_b\|_F}\right)^{-1};\ \boldsymbol{R}_b^{-1} = (\boldsymbol{R}_b + \gamma\boldsymbol{I})^{-1} \tag{21}$$

Simulation Setup

The sensor space utilized in the simulation was based on the spatial configuration of the Elekta/Neuromag™ whole-head MEG system (VectorView) which contains 306 sensors (204 gradiometers and 102 magnetometers). The modeled source space was generated using FreeSurfer, where a healthy subject's T1-weighted anatomical MRI was first segmented, and the resulting brain's gray-white matter boundary was then used to define a fixed source grid (7mm spacing). The segmented inner-skull surface was employed to construct a boundary element based triangular mesh (5mm side length). With the source grid and the triangular mesh, the MEG forward model calculation for the lead-field matrix was performed using a boundary element model (Huang et al., 2007;

Mosher et al., 1999). The built-in FSL Harvard-Oxford Atlas (Jenkinson et al., 2012) was utilized to identify the locations in which the simulated sources were placed. In total, ten sources were created, with a pair of sources placed in each of the following cortical regions (one per hemisphere): the superior frontal gyrus, the precentral gyrus, the middle temporal gyrus, the angular gyrus and the occipital pole. The location of the ten sources is illustrated in Figure 3.1 using an inflated FreeSurfer image of the subject's brain.

When designing the simulated source time-courses, we took into account previously observed characteristics of MEG fluctuations thought to be direct manifestations of electrophysiological FC (Brookes et al., 2011b; de Pasquale et al., 2010; Liu et al., 2010; Mantini et al., 2007). Recent papers (Brookes et al., 2004; Brookes et al., 2011a; Brookes et al., 2011b; Hall et al., 2013; Hipp et al., 2012; Luckhoo et al., 2012; Mantini et al., 2011; Tal et al., 2013) have routinely used the envelope of oscillatory fluctuations (also termed "Hilbert Envelope") of raw resting-state MEG time-courses as a means for quantifying FC across brain regions. Each source time-course was designed with the following general form: thirty seconds of an inactive period followed by thirty seconds of a sinusoidal waveform with an amplitude of 10 nAm (sampled at a standard MEG sampling rate of 1000Hz). In the first simulation, each source's sinusoid was composed of a unique frequency selected from the β band frequency (21Hz to 30Hz in increments of 1Hz), a frequency range commonly known to be involved in human inter-hemispheric cortical interactions (Brookes et al., 2011b; Liu et al., 2010; Mantini et al., 2007). The 1Hz frequency differences between sources ensured that zero correlation existed between any two raw time-courses, helping to minimize the common pitfall for standard MEG source analysis methodologies (e.g. SBF). Each of the raw source time-

courses were then convolved with a modulating low frequency (0.1 Hz) sinusoid (this introduced a negligible degree of raw source correlation; $r \leq 0.0075$), using a frequency known to be associated with resting-state MEG power modulation (de Pasquale et al., 2010; Liu et al., 2010). Thus, once the simulated MEG data have been processed for connectivity analysis (i.e. obtaining the "Hilbert envelope"), one would be left with the 0.1Hz modulating envelope as the source time-course to be used in correlation computations. To introduce variation into the correlation between the envelopes (as would exist in real data), a phase was introduced to each source's modulating envelope relative to the first source's envelope (in steps of 5°). For instance, the 2nd source's envelope had a 5° phase shift relative to the 1st source, while the 10th source's envelope had a 45° phase relative to the 1st source. Not only did this process ensure that the entire correlation range (0 to 1) was utilized for each individual source relative to all other sources, but it also created a visually distinct correlation matrix as illustrated in Figure 3.2. The ten simulated waveforms are displayed as well; for visualization purposes only the envelopes are shown.

In the second simulation, the challenging obstacle of raw source correlation was incorporated into the simulation, creating a more challenging environment for source reconstruction. This was accomplished by matching the β frequency of each pair of homologous sources (e.g., left and right precentral sources operate @ 25Hz, left and right occipital pole sources operate at 29Hz, and so forth) and introducing a phase shift between the raw source time-courses of each source pair (2 pairs set at 20°, 1 pair set at 50°, 1 pair set at 70° and 1 pair at 90°). It is important to note that no changes were made

to the sources' modulating envelopes (i.e. the correlation matrix being "solved for" should not change).

Once all source time-courses were constructed, the simulated sensor waveforms were computed for each scenario using the BEM forward model. SNR levels were adjusted by adding uncorrelated random Gaussian noise to the sensor waveforms, where the SNR was defined as the ratio of the Frobenius norm of the signal vector to that of the noise vector calculated over the interval with signal. In general, random Gaussian noise was added such that the sensor space SNR was set at 8. Source reconstruction for the second (correlated) simulation was also further examined at a lower sensor space SNR level of 2 to see how the reconstruction results were affected by the noisier conditions. Lastly, source reconstructions (i.e. the correlated sources simulation at SNR levels of 8 and 2) were also performed with the optimal MCBF solution to help gauge the quality of the proposed iterative algorithm in optimizing the generalized MCBF solution (i.e. simulated source locations used to reduce $\boldsymbol{L}$ to $\boldsymbol{L_m}$ for the optimal case).

Prior to source localization, sensor waveforms were band-passed filtered for the frequency range of interest (15Hz to 35Hz). This is a typical approach that helps optimize sensitivity of the beamformer reconstruction to effects in a band of interest (Brookes et al., 2011a; Brookes et al., 2008; Tal et al., 2013). A regularization parameter selected by visual inspection of the eigenvalue distribution was used to regularize the sensor time-courses for SBF and MCBF reconstructions (Sekihara et al., 2002, 2004; Van Veen et al., 1997). For each approach, an estimate of $\boldsymbol{R}_b$ was computed from the thirty-second active period, while an estimate of $\boldsymbol{R}_n$ was obtained from the complementary inactive period. The inverse problem was then computed (gradiometers only) using the proposed MCBF

algorithm and the original SBF (minimum-variance regularized vector) with and without the array-gain correction.

Performance of each methodology was evaluated by examining (1) the reconstructed source Hilbert envelope time-courses, (2) the corresponding source-to-source Hilbert envelope connectivity (Pearson correlation) matrix and (3) the source localization (RMS amplitude) maps (along with a corresponding F-statistic map). Their agreement with the "ground truth" source characteristics (shown in Figures 3.1 and 3.2) was measured by (1) the mean percent error in the source envelopes' RMS amplitude estimates, (2) the percent RMS error in envelope connectivity estimates for all source pairs and (3) the average distance error in the localized source RMS amplitude peaks (i.e. difference between the estimated and true peak locations). Source envelopes were normalized to the maximum value present in their respective reconstructed data, highlighting the relative scaling of the simulated sources to the overall solution provided by the spatial filter (ideally the maximum value corresponds to the value at the location of the simulated sources). For metrics (1) and (2), source envelopes used in the analysis were selected based on the simulated (true) locations. Note that this does not conflict with the notion that no *a priori* information is necessary for the methods, but rather helps us observe how well the algorithm did in reconstructing the activity in the correct (simulated) locations. For each RMS amplitude map, the lower and upper thresholds were set at 3% and 100% of the maximum RMS amplitude value, respectively. Statistical maps were computed by determining the Bonferroni-corrected F-statistic for each voxel by dividing signal window by noise window variances of the time-course envelope values using 118 degrees of freedom. The lower limit map threshold ($Fsig$) was set to the F-

statistic value corresponding to the desired p-value of 0.01. Upper limit map thresholds were set with $Fsat = Fsig + (Fmax - Fsig) \cdot 0.1$.

Median-Nerve Stimulation Task

To examine the performance of the MCBF localization algorithm on real, evoked human data we observed the MEG responses to right median nerve stimulation. This common approach used to study the somatosensory system provides a useful standard for analyzing performance as the location of activity has been documented extensively. MEG and functional studies utilizing other modalities have established that somatosensory stimulation typically activates the thalamus (Huang et al., 2006; Kandel, 2000; Tesche, 1996), BA 1, 2, and 3b of the primary somatosensory cortex (S-I) (Forss et al., 1994; Forss and Jousmaki, 1998; Hari and Forss, 1999; Huang et al., 2004a; Huang et al., 2000; Huang et al., 2006; Huang et al., 2004b; Huang et al., 2005; Jousmaki and Forss, 1998; Kandel, 2000; Mauguiere et al., 1997a, b; Wood et al., 1985), BA 4 of the primary motor area (Baldissera and Leocani, 1995; Davidoff, 1990; Huang et al., 2004a; Huang et al., 2000; Huang et al., 2005; Jones et al., 1978; Jones et al., 1979; Kawamura et al., 1996; Lemon, 1981; Lemon and Porter, 1976; Lemon and van der Burg, 1979; Rosen and Asanuma, 1972; Spiegel et al., 1999; Wong et al., 1978), BA 5 of the superior parietal area (Boakye et al., 2000; Forss et al., 1994; Huang et al., 2006; Jones et al., 1978; Jones et al., 1979; Kandel, 2000; McGlone et al., 2002; Waberski et al., 2002), BA 6 of the supplementary motor area or SMA (Barba et al., 2001; Boakye et al., 2000; Huang et al., 2006; Urbano et al., 1997) and BA 40 of the secondary somatosensory cortex (S-II) (Forss and Jousmaki, 1998; Fujiwara et al., 2002; Hari and Forss, 1999; Hari et al., 1993; Huang et al., 2006; Huang et al., 2005; Kandel, 2000; Simoes et al., 2003). Furthermore,

since the stimulation results in a complex network of closely-spaced and correlated source activation, a challenging localization scenario is provided for reconstruction.

MEG recordings were obtained using a single healthy male subject. The subject's median nerve was stimulated using a bipolar Grass^{TM} constant-current stimulator. The stimuli were square-wave electric pulses of 0.2 ms duration delivered at a frequency of 1 Hz. The inter-stimulus-interval (ISI) was between 800 and 1200 ms. The intensity of the stimulation was adjusted until robust thumb twitches were observed. A trigger was designed to simultaneously send a signal to the MEG for every stimulus delivery to allow averaging over evoked trials. Magnetic fields evoked by median nerve stimulation were measured using the Elekta/Neuromag^{TM} whole-head MEG system. EOG electrodes were used to detect eye blinks and eye movements. An interval of 500 ms post-stimulus was recorded, using 300 ms of pre-stimulus data for noise measurement. An interval of 30 ms centered on the stimulus was discarded due to the presence of stimulus-related artifacts. Data were sampled at 1000 Hz and run through a high-pass filter with a 0.1 Hz cut-off and through MaxFilter to remove environmental noise (Song et al., 2009; Song et al., 2008; Taulu et al., 2004; Taulu and Simola, 2006). 512 artifact-free MEG responses were averaged with respect to the stimulus trigger.

Registration of MRI and MEG was performed using data obtained from the Polhemus Isotrak system prior to MEG scanning. The source space was defined using FreeSurfer's segmentation of the subject's T1-weighted anatomical MRI where the brain's gray-white matter boundary obtained was used to position the dipoles (7mm spacing). As in the simulated portion, the segmented inner-skull surface was employed to construct a boundary element based triangular mesh (5mm side length). With both the

source grid and the triangular mesh, the MEG forward model calculation for the lead-field matrix was performed using a boundary element model (Huang et al., 2007; Mosher et al., 1999). The sensor covariance matrix, $\boldsymbol{R}_b$, was constructed using the post-stimulus interval while a diagonal estimate of $\boldsymbol{R}_n$ was computed using the pre-stimulus interval. The regularization level of $\boldsymbol{R}_b$ (Sekihara et al., 2002, 2004; Sekihara, 2008; Van Veen et al., 1997) was determined by utilizing a modified "broken-stick" model which helps identify the meaningful components of the data (Behzadi et al., 2007; Tal et al., 2013). A regularization parameter equal to the sixth largest eigenvalue of $\boldsymbol{R}_b$ (approximately equal to 4.5% of the largest eigenvalue) was used for localization and time-course estimation. The MCBF algorithm was executed with 32 iterations in order to generate the shown source time-courses and source localization (RMS amplitude) map. The data was also processed equivalently with the SBF (with array-gain correction). An evaluation and comparison of each methodology's performance was completed by visual means.

Results

Simulation Results

The performance of both algorithms for the first simulation (minimally correlated sources; $r \leq 0.0075$) is graphically summarized in Figure 3.3. For each of the methods (MCBF – left column, SBF – center column, SBF w/ array-gain correction – right column), the reconstructed source Hilbert envelopes (top row), the inter-source Hilbert envelope connectivity matrix (2nd row) and the source localization (RMS amplitude) map (3rd row) with the corresponding F-statistic map (bottom row) are displayed. The MCBF performed considerably well: source envelope amplitudes (4.1%±3.1% error) and waveforms were properly recovered resulting in an accurate estimation of inter-source

envelope connectivity (0.67%±0.02% error) while no error was observed in peak localization (i.e. estimated peak location for each source coincided with the simulated location). Qualitative inspection of the RMS map's topography reveals MCBF's strengths of accuracy along with precision (i.e. symmetric and well-defined peaks centered on simulated locations), further confirmed by the F-statistic map which shows source significance only when overlapping with simulated locations (i.e. those which are supposed to contain signal). Since the F-statistic reflects the likelihood of a source existing based on source space SNR, the observed agreement between the two maps reflects MCBF's ability to minimize spatial biases.

In contrast, the reconstruction performance of the SBF (without the array-gain correction) was of a mixed nature. Although, envelope waveforms were adequately reconstructed such that the error in connectivity measures was minimal(0.57%±0.02% error), the sources amplitudes (relative to the maximum RMS value in the reconstructed SBF dataset) were severely underestimated (70.0%±0.1% error). This is a result of the SBF's sensitivity to the spatial non-uniformity of the lead-field norm resulting in a large, false intensity (i.e. weights approach infinity) near the center of the brain (Kumihashi and Sekihara, 2010; Sekihara, 2008). Moreover, unlike the MCBF, the spatial extent of the SBF sources in the RMS amplitude map is loosely defined (e.g. smeared, "blob"-like), reflecting a familiar yet undesirable beamformer phenomenon known as *signal leakage* (Brookes et al., 2012) where voxels surrounding true sources show a false signal (the source signal is essentially "leaking" into them). The combination of these two susceptibilities can be detrimental as now both the reconstructed signal's true origin and true amplitude are undistinguishable. Thus, SBF source localization is rendered

impractical as no local peaks exist around the simulated locations (all the energy is "leaking" towards the brain's center at an increasing slope). This severe spatial bias results in stronger yet false sources "penetrating" the final RMS amplitude map, virtually attenuating the true sources and thus hindering them from view. However, as the F-statistic is spatially bias-free (both signal and noise contain the same nonuniform lead-field bias, and thus it cancels out), the corresponding F-statistic map still shows hot spots in the correct locations.

The array-gain modification introduced to the SBF attempts to address this problem by rescaling the weight vector to account for such non-uniformity (Kumihashi and Sekihara, 2010; Sekihara, 2008). Envelope amplitude estimation improved (25.0%+19.2% error) and while the waveforms did appear slightly noisier than before the correction, there was only a minimal effect on the connectivity estimates (0.63%±0.02% error). Furthermore, the source RMS amplitude map now exhibited amplitude peaks at the nearby the correct (simulated) locations, thus allowing the calculation of the localization metric (1.33mm average error). We note that the largest RMS amplitude value in the dataset corresponded now to a true source, demonstrating that the array-gain modification rescaled the data to help "bring out" the actual sources and partially overcome the large, false signal in the center. Nevertheless, source time-courses were not scaled in a fully equivalent manner, unlike the non-corrected SBF where relative inter-source scaling was preserved. Furthermore, minimizing the SBF's spatial bias ultimately caused the RMS map contours to match those of the F-statistic map. However, despite this adjustment, the two middle temporal sources are still barely visible (corresponding to

the two attenuated time-courses). Furthermore, the array gain correction does not address the problem of signal leakage (i.e. local source topography).

Overall, the quantitative assessment indicated that both the MCBF and the SBF with the array-gain modification technique could adequately localize sources as well as estimate the underlying envelope correlations (the non-corrected SBF could only accomplish the latter). However, the MCBF's source reconstruction strongly outperformed either version of the SBF when estimating the amplitude not only of signal containing voxels (i.e. the genuine sources) but also those voxels which should not contain any signal (i.e. noise only). Such behavior can be explained by the fact that the iterative MCBF algorithm simply finds a more effective way to project the highly linearly-dependent data into the source space, thereby strongly minimizing the signal leakage effects on the reconstructed MCBF results. The presence of many such "false" voxels in the SBF reconstruction is a significant drawback, highlighting that it still has some limitations even when the sources environment conditions are minimally correlated.

Next, the algorithm performance was examined as varying degrees of correlation were introduced between the source pairs (i.e. correlation between the raw source-space–projected time series, not the Hilbert envelopes). The reconstruction results are summarized in Figure 3.4. MCBF reconstruction efforts were largely unaffected due to its immunity to raw source correlation. Source envelope time-course amplitudes (7.1%±5.46% error), inter-source connectivity estimates (1.33%±0.04% error), the source localization (0mm error), and F-statistic maps remained comparable to those obtained under the minimally correlated conditions. In contrast, a review of the reconstructed SBF data revealed the presence of strong interference effects. Considerable source amplitude

attenuation (47.6%±21.2% and 40.8%±27.2% error without and with the array-gain correction, respectively) and time-course distortion resulting in connectivity misestimation (17.5%±0.4% error for both) were observed. Interestingly, intra-hemispheric envelope correlation values were generally overestimated while the inter-hemispheric connectivity values were primarily underestimated. As with the previous simulation, the SBF localization map showed below par source topography due to signal leakage and the need for the array-gain correction. Due to several of the sources "leaking" to the center of the brain, localization accuracy still could not be estimated with the non-corrected SBF version, while the average localization error for the array-gain corrected version more than doubled (2.93mm). The source attenuation due to underlying correlations also noticeably influenced both of the SBF F-statistic maps. The reduction in contribution from the signal component lowered the source space SNR, thus lowering the significance (i.e. F-stat) of all dipoles across the brain. To summarize, these results indicate that when correlated sources are present, performance of the SBF markedly decreases whereas the MCBF continues to perform well, regardless of the added challenge.

Algorithm performance reconstructing correlated activity in a noisier environment (SNR level of 2) was also explored (Figure 3.5). An examination of the SBF reconstruction revealed minor performance reductions (59.2%±15.9% error in RMS amplitude and a 19.8%±0.5% error in connectivity for the non-corrected SBF; 41.2%±26.1% error in RMS amplitude, 20.07%±0.5% error in connectivity and 2.93mm average localization error for the array-gain SBF), suggesting that the errors induced by the correlation between sources outweighed the effect of increased noise levels. In

contrast, as the MCBF is inherently robust to source correlation, observable changes in reconstruction quality could be attributed to the increase in noise. Most reconstructed source envelope time-courses demonstrated amplitude suppression (55.2%±35.5% error) and noisier waveforms, with the latter resulting in greater misestimation of inter-source envelope connectivity (6.5%±0.02%error). For the first time, the MCBF localization was imperfect (2.1mm). Nonetheless, it is important to note that the similarity in the SBF and MCBF values of the mean distance errors can be misleading. Although noise did result in a loss of precision in MCBF peak localization, the MCBF sources' focal nature (i.e. peak definition and spatial extent) was generally preserved in both the F-statistic and RMS maps (as when compared to the SBF maps). Thus, even in the presence of noise, the iterative MCBF algorithm successfully manages to reduce signal leakage, such that spatial assessment of source activity does not suffer.

In summary (Table 1), increased noise levels had minimal effect on SBF performance as its inability to properly reconstruct in a correlated environment overshadowed the effects of the lower SNR. In contrast, certain components of the MCBF reconstruction (amplitude and connectivity estimates) did suffer to some degree from the noisier conditions. However, as Moiseev and Herdman (2013) discussed in detail, the mathematics of the eDCBF (and its expanded version - the MCBF) should allow for perfect reconstruction at any arbitrary SNR as long as the source positions are known (and a good noise estimate is available). To validate this claim and the capabilities of the underlying MCBF mathematics, we used the known source locations to test the optimal MCBF case in which the weight matrix is "focused" using the known simulated source locations (see Methods). By doing this we are also indirectly assessing the

limitations of the proposed iterative algorithm (i.e. ability to identify the optimal beamformer weight matrix). The optimal MCBF reconstruction results for both the high (8) and the low (2) SNR levels in a correlated environment are displayed in Figure 3.6. As expected, a qualitative evaluation indicated a strong improvement in reconstruction quality in the noisy environment. Reconstructed source envelopes exhibited more accurate amplitudes (3.9%±0.5% and 4.6%±0.8% error for SNR levels of 8 and 2, respectively) and waveforms leading to improved connectivity measures (0.66%±0.02% and 1.58%±0.05% error for SNR levels of 8 and 2, respectively). For the noisy conditions (SNR 2), these values represent a significant improvement over those provided by iterative algorithm (the RMS amplitude error was reduced by more than 90%; connectivity error was reduced by 75%). They also represent a slight improvement over the high SNR iterative values (amplitude error reduced by 45%; connectivity error reduced by over 50%), although the absolute correction is much smaller than in the low SNR case. This highlights both the MCBF's underlying potential as a mathematical technique for recovery of time-course and connectivity measures as well as the need for improvement in the iterative algorithm for future implementations.

Median Nerve Stimulation Task Results

The measured human MEG response to the median-nerve stimulation is shown in figure 3.7 (gradiometer sensors displayed only; all channels superimposed). The ensuing source reconstruction results (source activity map and time-courses) are summarized for both methods visually in figures 3.8-3.10. Figure 3.8 displays the source RMS amplitude localization maps obtained for SBF (top) and MCBF (bottom). The source map produced by MCBF reveals the expected activation in the many regions of the somatosensory

system (S-I,M1,SMA,S-II, SP) and thalamus as well as other areas, including the superior temporal gyrus and the parietal-occipital junction. In contrast, the SBF reconstruction managed to mainly resolve only the dominant region of activity (where most of the energy was located) while all secondary regions were suppressed. The highlighted activity is also smeared across the primary somatosensory region (unlike the sparse, well-defined peaks of the MCBF sources), challenging the characterization of distinct sources. We note that when the array-gain constraint was not applied (not shown in figure), no source activity on the lateral surface was detected as all energy leaked to the center due to spatial bias (as was seen in the simulations). It is also interesting to note that the map thresholding was applied equally (a set percentile of the cumulative distribution function (CDF) of the RMS data), yet it corresponded to a vastly different range of the RMS data values (over 90% of the entire RMS range was included in the MCBF map in comparison to a little over 40% of the SBF's RMS range). Once again, this emphasizes the impact of signal leakage on the reconstruction, as the sheer number of voxels containing false signal increases immensely, considerably hindering the ability to discover and properly distinguish all true sources.

Time-course reconstruction was examined as well (Figure 3.9-10). All reconstructed source time-courses (superimposed) are displayed in the top panel of Figure 3.9 for both the MCBF (left) and the SBF (right). A simple visual comparison indicates not only that some components of the transient response were not revealed (e.g. S-II, SMA components), but that the signal of those responses which were captured has leaked to many surrounding grid locations (many non-zero time-courses, thus the "noisy" look). The predicted MEG sensor waveforms (computed from the reconstructed time-

courses using the same forward model as in the inverse solution) are shown in the bottom panel of Figure 3.9 for both the MCBF (left) and the SBF (right). The strong similarity between the recorded (Figure 3.8) and the predicted MCBF sensor waveforms indicate that the solution reasonably explains the proposed underlying source configuration. Conversely, the strong mismatch between the recorded and the predicted SBF waveforms highlights the erroneousness of the SBF's attempt at solving the inverse problem. Individual time-courses for the S-I and S-II activity peaks (picked using the MCBF reconstruction) are presented in Figure 3.10 for the MCBF (left) and the SBF (right). The MCBF S-I activation (BA 3b) showed a strong transient response 20 ms following stimulation. The MCBF S-II activation showed a much smaller initial transient response with a large delayed response peaking at about 80-90 ms. The latencies of these peak activations as well as the general wave shape agree with previous neurological studies (Boakye et al., 2000; Forss and Jousmaki, 1998; Hari and Forss, 1999; Huang et al., 2006). The SBF source time-courses appear much noisier, and although the SBF S-I activation transient response was still primarily visible, the S-II activation seemed to be considerably suppressed and masked by noise.

Conclusions

Despite an inability to accurately operate in correlated settings (Brookes et al., 2007; Dalal et al., 2006; Diwakar et al., 2011a; Diwakar et al., 2011b; Hui and Leahy, 2006; Hui et al., 2010; Moiseev et al., 2011; Moiseev and Herdman, 2013; Quraan and Cheyne, 2010; Sekihara et al., 2002), the *conventional single beamformer* (SBF) is a popular source reconstruction technique commonly used in FC analyses of task-related and spontaneous MEG recordings (Brookes et al., 2011a; Brookes et al., 2012a; Brookes

et al., 2011b; Hall et al., 2013; Hillebrand et al., 2012; Hipp et al., 2012; Luckhoo et al., 2012; Mantini et al., 2011; Tal et al., 2013). Various modifications have been put forward to address this inherent mathematical limitation of the SBF, yet they either require *a priori* information or are incapable of estimating FC (source-to-source and/or whole-brain). In this chapter, we adapted an iterative Bayesian-based localization approach and applied it without any *a priori* information to the *multi-core beamformer* (MCBF), enabling accurate source localization irrespective of the underlying correlation while also providing per voxel time-course reconstruction, which is a requirement for whole-brain FC estimations. We emulated resting-state waveforms and designed intricate simulations involving ten sources, as compared to the more common 3 to 4 sources typically used in prior work, to perform a comparison of the MCBF and the SBF reconstruction capabilities at varying connectivity strengths (for both the raw time-courses and envelopes) and SNR conditions. Task-activated neuromagnetic measurements (median-nerve stimulation) were used to further assess the beamformers' ability to resolve closely-spaced, highly correlated human neural networks. Our results showed that the SBF and MCBF were both capable of producing accurate inter-source power envelope correlation estimates when no raw inter-source correlations existed. Nevertheless, the RMS maps clearly showed that the MCBF was superior in correctly localizing the simulated sources, whereas SBF source definition was spatially smeared (i.e. due to signal leakage) as well as spatially biased when the array-gain correction was not applied. Furthermore, the envelope time-course plots demonstrated that MCBF successfully recovered source amplitudes while SBF envelopes were improperly scaled (with or without the array-gain correction). In the presence of raw inter-source correlation, the MCBF outperformed the

SBF (regardless of the array-gain constraint) in all reconstruction categories: source localization, estimation of inter-source envelope correlations, and source amplitude recovery. When noise levels were substantially increased, the ability of our localization algorithm to refine the weight matrix was lessened. Interestingly, the SBF reconstruction results were still so strongly influenced by the existing inter-source correlation that effects due to increased noise levels were overshadowed. In the evoked (high SNR, highly correlated) recordings, the MCBF bettered the SBF yet again, reconstructing more comprehensive source activity maps (resolving all the components of the heavily-studied somatosensory response), cleaner and better-detailed source time-courses (reducing signal leakage) and predicted sensor waveforms nearly identical to the originals. Altogether, these results suggest that the MCBF holds more promise than the SBF as a tool suitable for studying intricate MEG dynamics as well as conducting MEG FC analyses.

Whole-brain measurements of neural dynamics are essential for FC investigation of the electrophysiological signal in the resting-state brain (Brookes et al., 2011b; de Pasquale et al., 2010; Mantini et al., 2011). This feature was previously unavailable in prior multi-source beamformers, as they were designed to only evaluate activity at selected locations of interest (Brookes et al., 2007; Diwakar et al., 2011a; Diwakar et al., 2011b; Moiseev et al., 2011), unlike the conventional beamformers (SBF/NB/CCSM). This limitation was overcome by the generalized framework of the MCBF, permitting simultaneous application of the beamformer (i.e. source-space projection) to every grid point. The MCBF's expanded ability to compute voxel-by-voxel time-courses and

amplitude estimates is thus of critical importance in its application to whole-brain FC analyses.

Concerns regarding beamformer signal leakage are also addressed by the proposed algorithm. Signal leakage is currently a significant hindrance in assessing MEG dynamics, FC and resting-state network formation (Brookes et al., 2011a; Brookes et al., 2011b; Brookes et al., 2012b) as it introduces spurious connectivity measures (Brookes et al., 2012b). Although corrections for such effects have been proposed (Brookes et al., 2012b), it was noted that the success of the suggested fix was highly dependent on the particular source projection algorithm employed. A second concern was that the correction could also remove any genuine zero-lag neurophysiological communications that existed, a generally undesirable effect. As suggested by Brookes et al. (2012b), application of beamformers that are insensitive to raw inter-source correlation could hold the key to solving this issue. The present study supports the validity of this hypothesis showing that the MCBF can overcome one of the greatest drawbacks of the SBF (and other beamformers as well).

Nonetheless, the algorithm for hyperparameter optimization still exhibits some shortcomings and certainly has room for improvement. The simulations showed the algorithm's performance degrading as noise levels increased; on the contrary, the accuracy of the optimal MCBF solution remained identical (as was mathematically proven by Moiseev and Herdman (2013)). While this underscores the mathematical potential of the MCBF technique, it also reflects the iterative algorithm's need to more effectively refine the generalized solution (i.e. the beamformer weight matrix). Thus, further improvement or development of more robust algorithms is warranted.

MEG resting-state measurements conventionally employ five minutes of data (Brookes et al., 2011a; Brookes et al., 2011b; Brookes et al., 2012b; de Pasquale et al., 2010; Hall et al., 2013; Hillebrand et al., 2012; Hipp et al., 2012; Luckhoo et al., 2012; Mantini et al., 2011; Tal et al., 2013) for construction of the signal covariance matrix, thus providing a higher effective SNR for the beamformer and improving its reconstruction performance (Brookes et al., 2008). In our study, we designed our waveforms to contain only 30 seconds of signal (at the equivalent sampling rate to real data), thereby challenging the filter more than is typically done for spontaneous analyses. In the future, the application of the MCBF to real data which contains more samples (e.g. 10x for a 5 minute recording) should only improve reconstruction performance. Combined with the ability to minimize signal-leakage and spatial bias (towards the head's center) and operate in the presence of underlying source correlation, the MCBF could lead to vastly improved estimates of FC and better characterization of resting-state networks.

In conclusion, use of the SBF in FC studies has been largely justified by hypothesizing that the nature of correlated neuronal oscillations in the resting-state is short-lived and thus, should have little impact on time-course reconstruction (Brookes et al., 2011b). However, this would truly be unverifiable using the SBF, as its inherent limitation hinders accurate examination of the underlying correlations among the supposed "resolved" sources. As the MCBF innately bypasses this obstacle, and even further, curtails signal leakage distortions as well as accurately and precisely reconstructs source features, it is conceivably the ideal tool for future FC investigations in the MEG domain (Moiseev and Herdman, 2013).

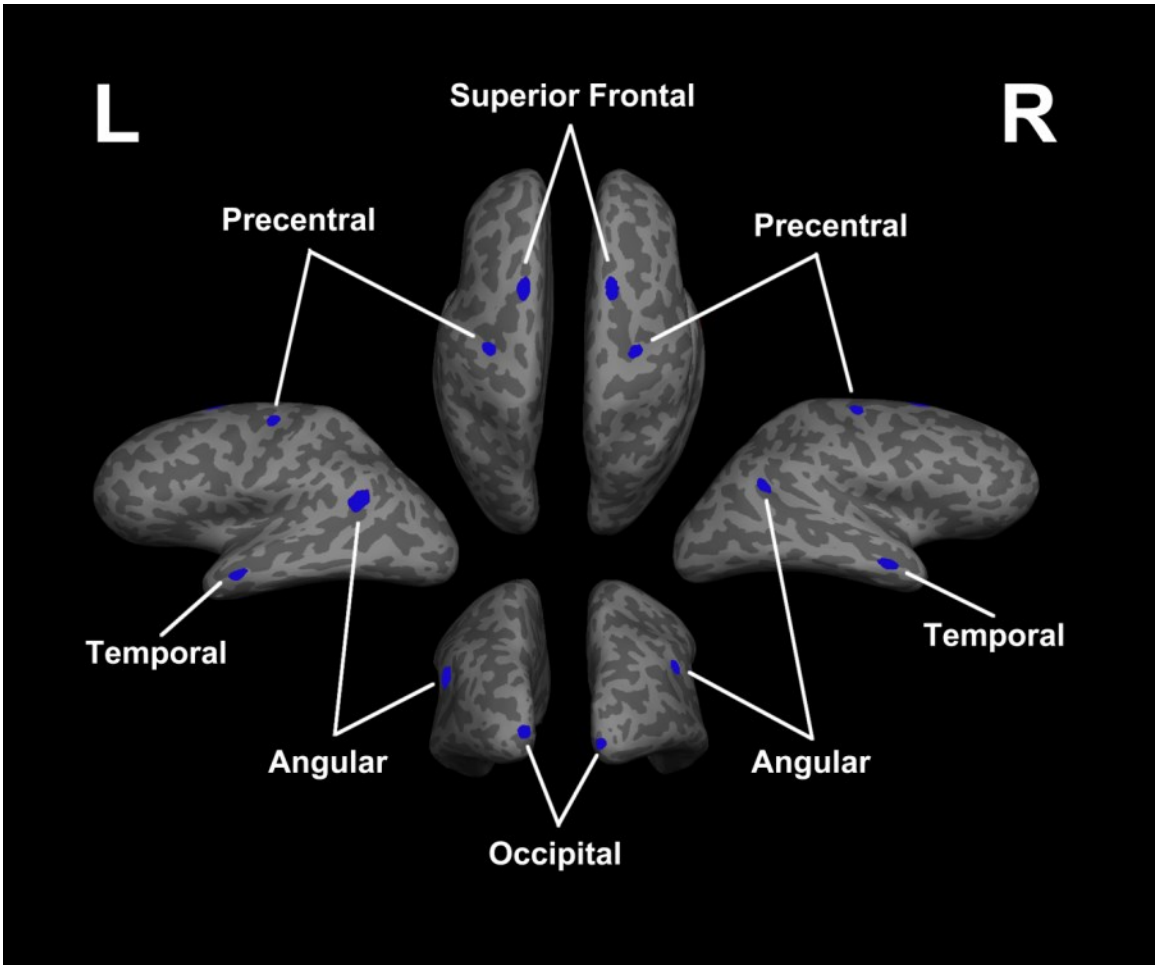

Figure 3.1: Subject's head (inflated in FreeSurfer) displaying the true location of all ten simulated sources (L and R designate left and right hemispheres).

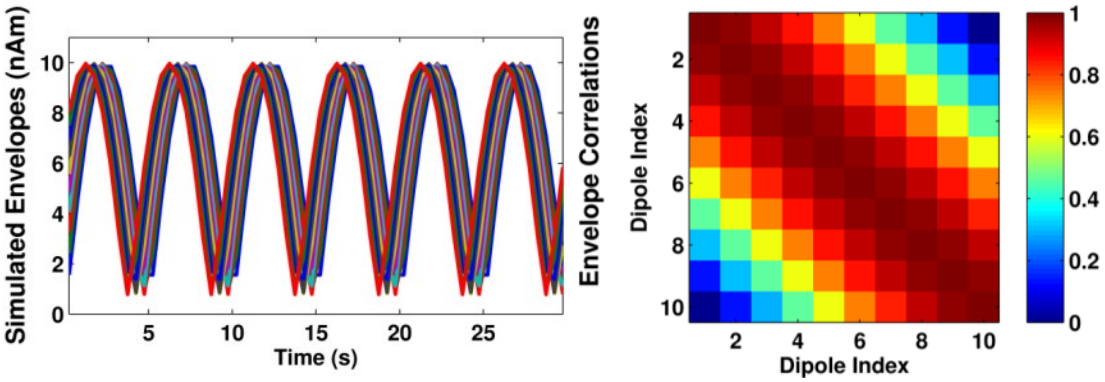

Figure 3.2: ***Left panel*** **– Simulated time-courses (Hilbert envelopes) for all ten sources.** ***Right panel*** **- Source-to-source connectivity (Pearson Correlation) matrix formed by cross-correlating all the source envelope time-courses displayed above.**

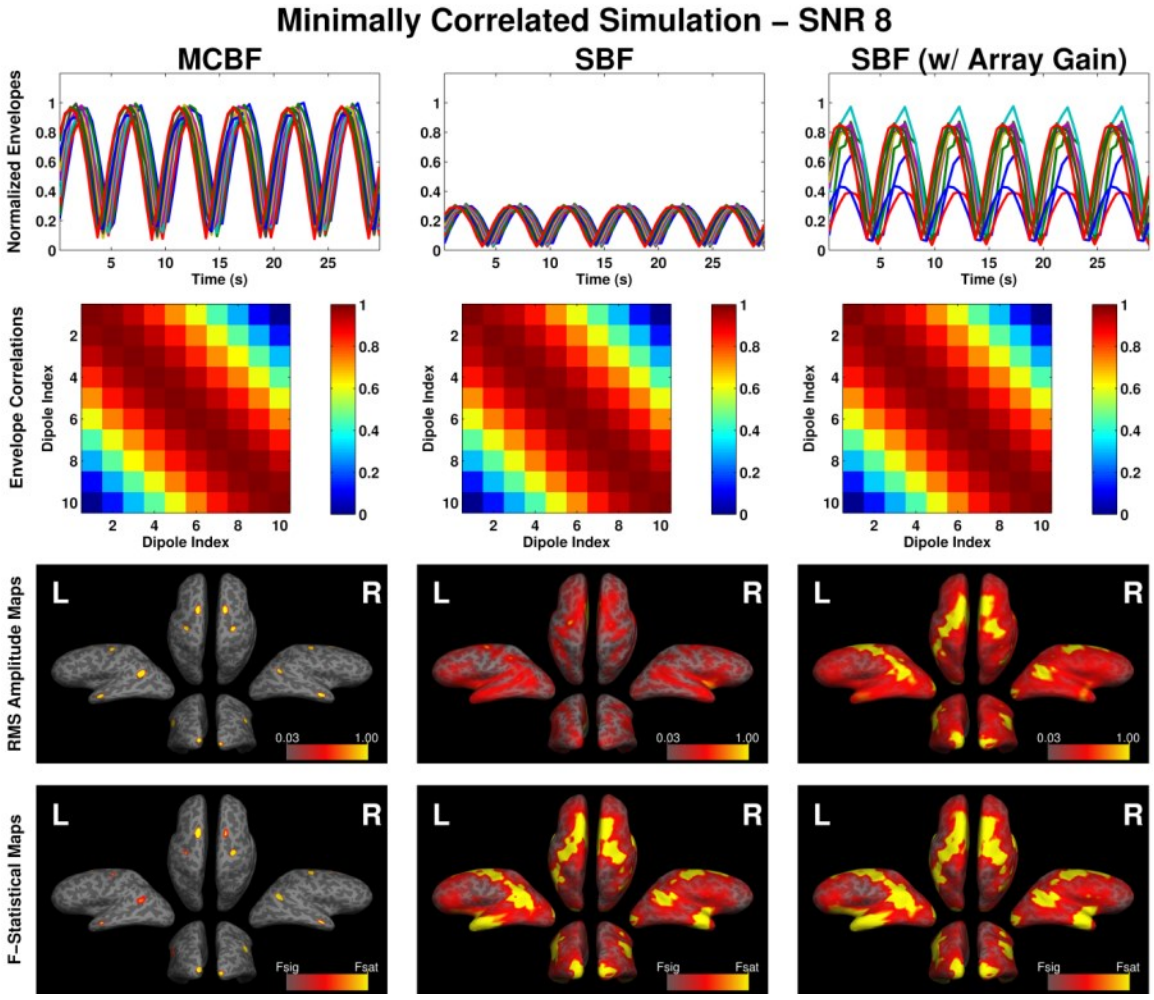

Figure 3.3: Source reconstruction results for the Minimally Correlated Sources Simulation (SNR = 8) for the Multi-Core Beamformer (MCBF), the Single Beamformer (SBF), and the SBF with the array-gain constraint.
Top Panels – Reconstructed "Hilbert envelope" time-courses for all ten sources. 2nd Row Panels - Source-to-source connectivity (Pearson correlation) matrix formed from the estimated envelope time-courses. 3rd row Panels -Source RMS amplitude maps (significant voxels only) with the minimum and maximum thresholds set at 3% and 100% of the maximum RMS amplitude value, respectively. Bottom Panels –F-statistic maps with Fsig corresponding to $p < 0.01$ (Bonferroni corrected).

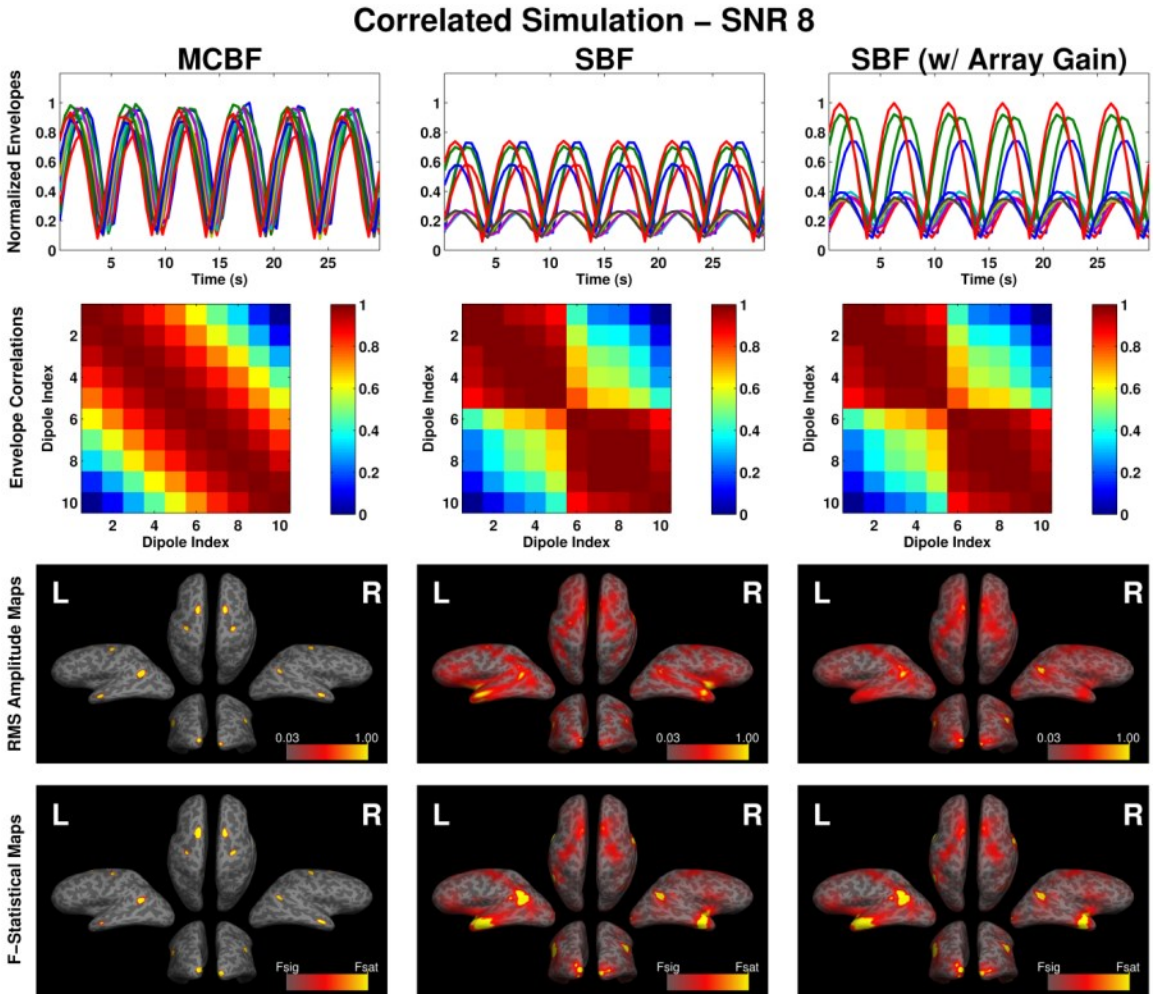

Figure 3.4: Source reconstruction results for the Correlated Sources Simulation (SNR = 8) for the Multi-Core Beamformer (MCBF), the Single Beamformer (SBF), and the SBF with the array-gain constraint.
Top Panels – Reconstructed "Hilbert envelope" time-courses for all ten sources. 2nd Row Panels - Source-to-source connectivity (Pearson correlation) matrix formed from the estimated envelope time-courses. 3rd row Panels - Source RMS amplitude maps (significant voxels only) with the minimum and maximum thresholds set at 3% and 100% of the maximum amplitude RMS value, respectively. Bottom Panels –F-statistic maps with F_{sig} corresponding to $p < 0.01$ (Bonferroni corrected).

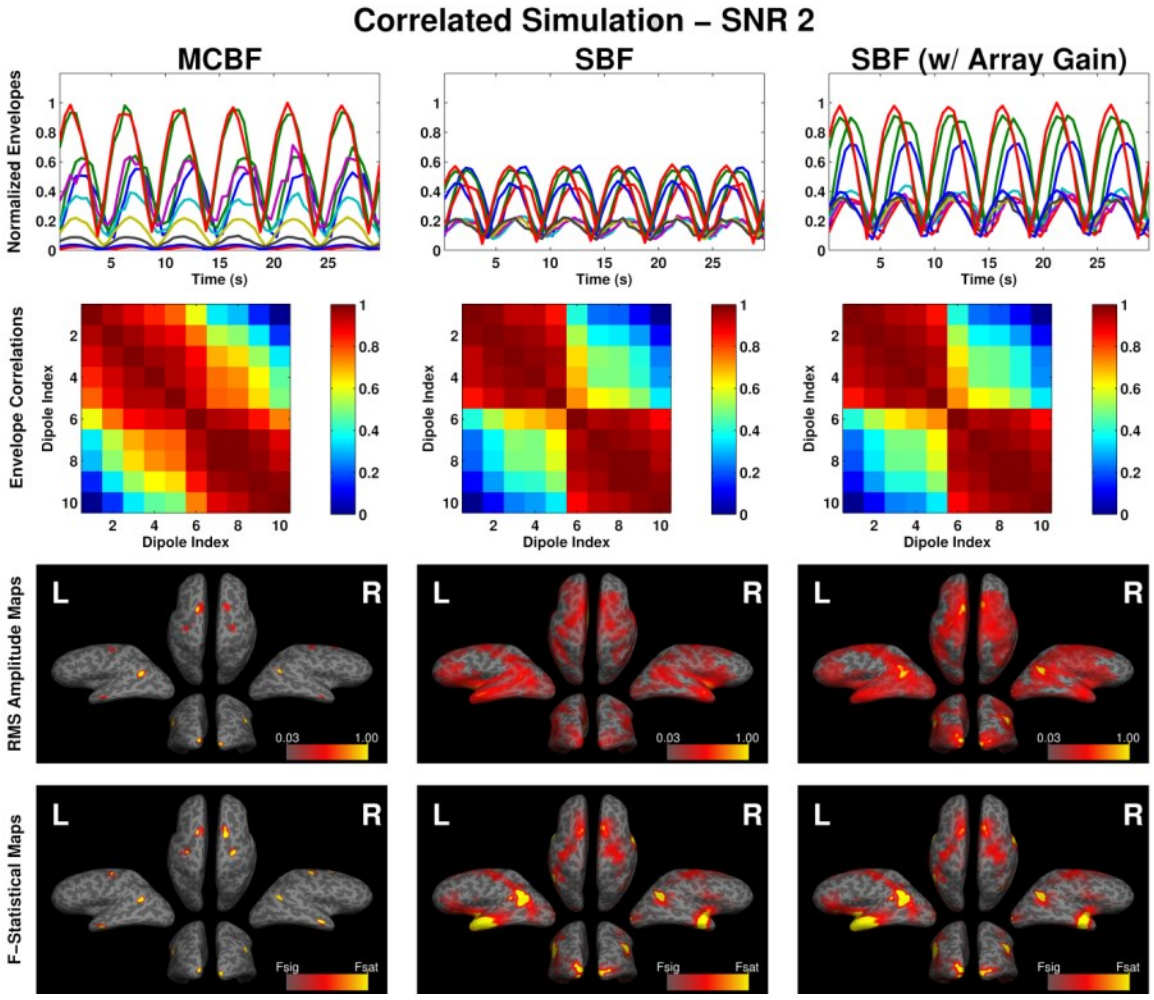

Figure 3.5: Source reconstruction results for the Correlated Sources Simulation (SNR = 2) for the Multi-Core Beamformer (MCBF), the Single Beamformer (SBF), and the SBF with the array-gain constraint.
Top Panels – Reconstructed "Hilbert envelope" time-courses for all ten sources. 2nd Row Panels - Source-to-source connectivity (Pearson correlation) matrix formed from the estimated envelope time-courses. 3rd row Panels - Source RMS amplitude maps (significant voxels only) with the minimum and maximum thresholds set at 3% and 100% of the maximum amplitude RMS value, respectively. Bottom Panels –F-statistic maps with F_{sig} corresponding to $p < 0.01$ (Bonferroni corrected).

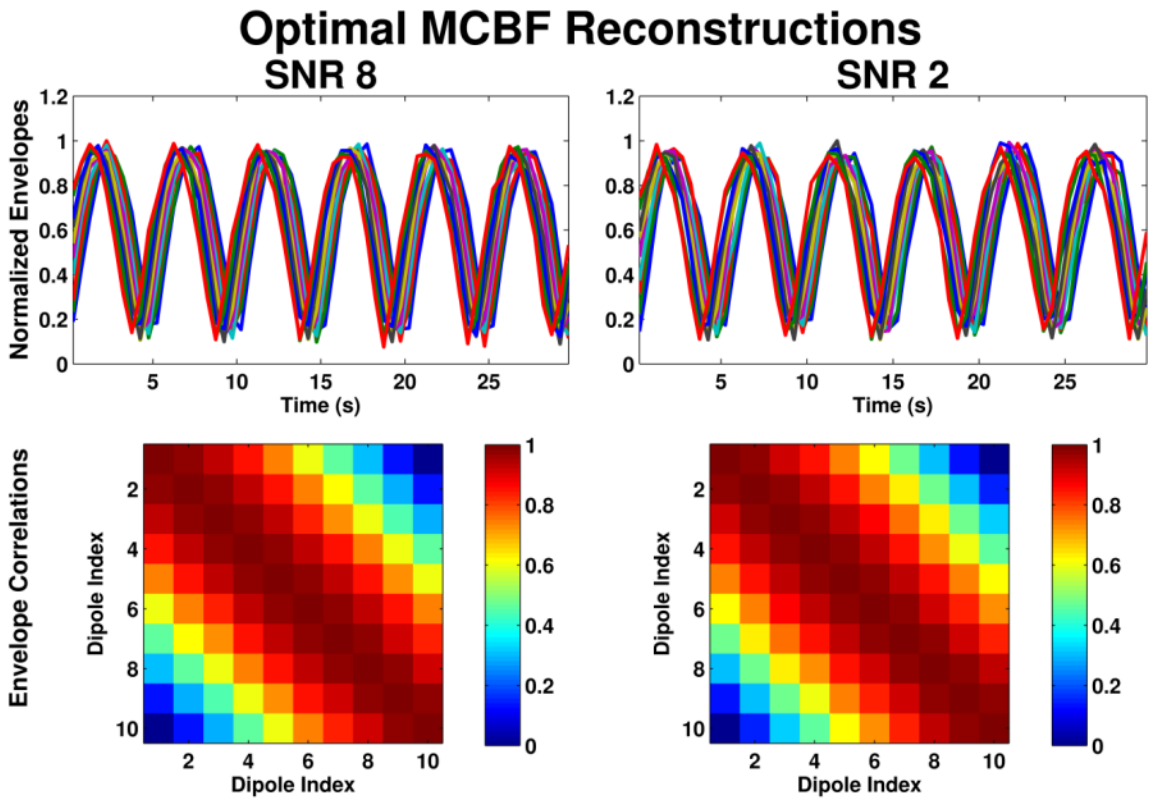

Figure 3.6: Optimal Multi-Core Beamformer reconstruction results for the Correlated Sources Simulation at a SNR level of 8 (left) and at a SNR level of 2 (right).
Top panels – Reconstructed "Hilbert envelope" time-courses for all ten sources. Bottom panels - Source-to-source connectivity (Pearson correlation) matrix formed from the estimated envelope time-courses.

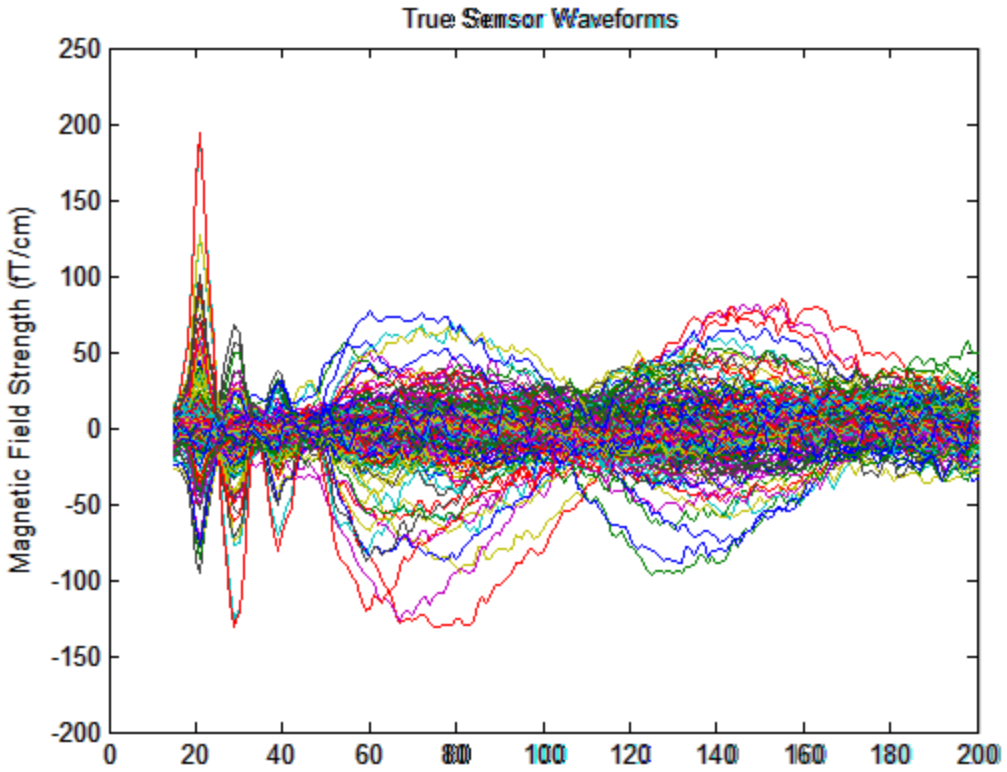

Figure 3.7: The recorded MEG sensor (gradiometers only) waveforms for the right median-nerve stimulation experiment

An exact representation of the data prior to being sent to the SBF and the MCBF reconstructions. Note the first 15ms were not included as an interval of 30ms (centered on the stimulus) was discarded due to the presence of stimulus-related artifacts.

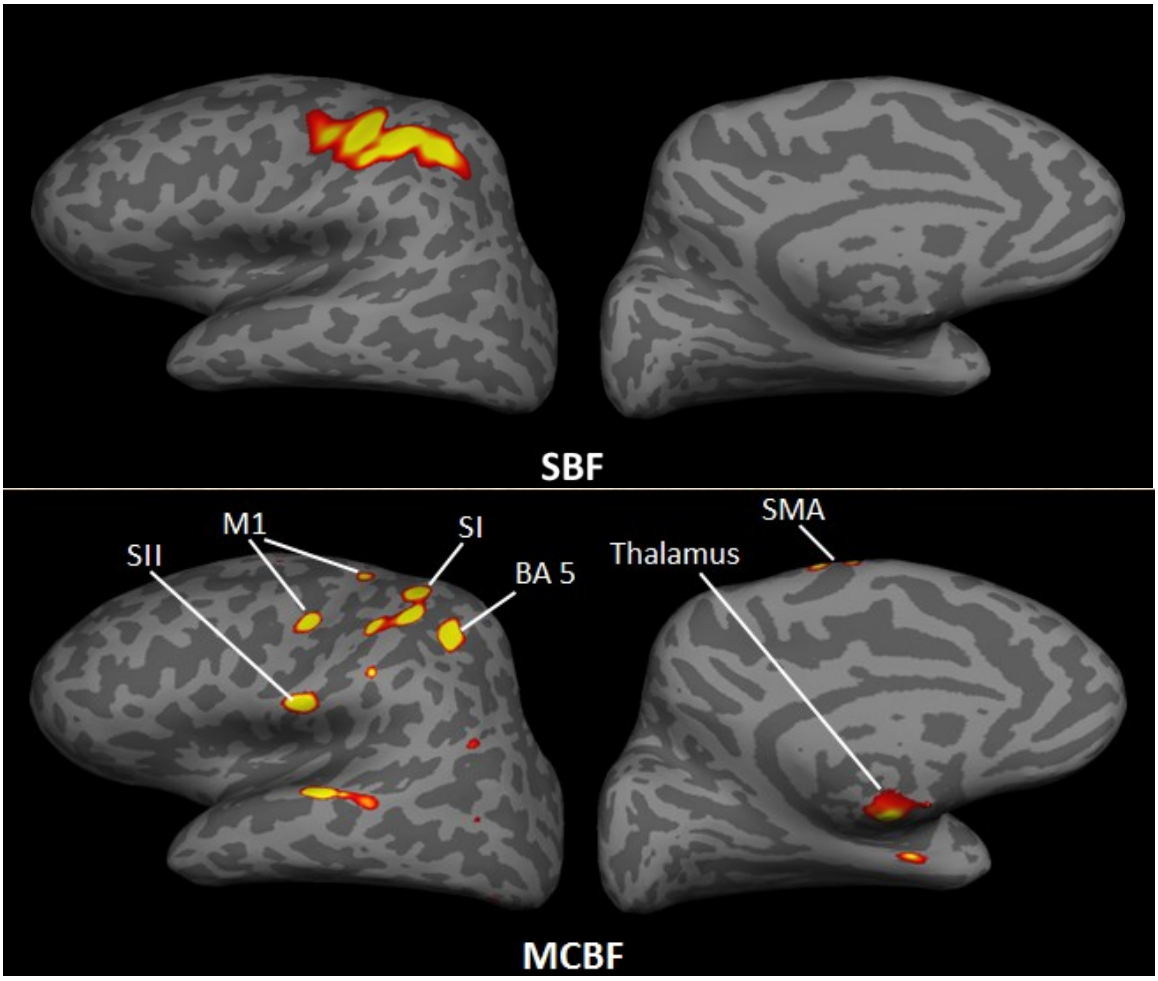

Figure 3.8: Median-nerve source localization (RMS amplitude) maps provided by the SBF and MCBF algorithm (left hemisphere shown).
Source RMS amplitude map red and yellow thresholds were set at the 97th percentile and the 99th percentile of the CDF, respectively. Only significant voxels (whose Bonferroni-corrected F-statistic was larger than the F-stat which corresponds to p = 0.01) are displayed. M1 = primary motor cortex; S-I = primary somatosensory cortex; S-II = secondary somatosensory cortex; SMA = supplementary motor area; BA = Brodmann area.

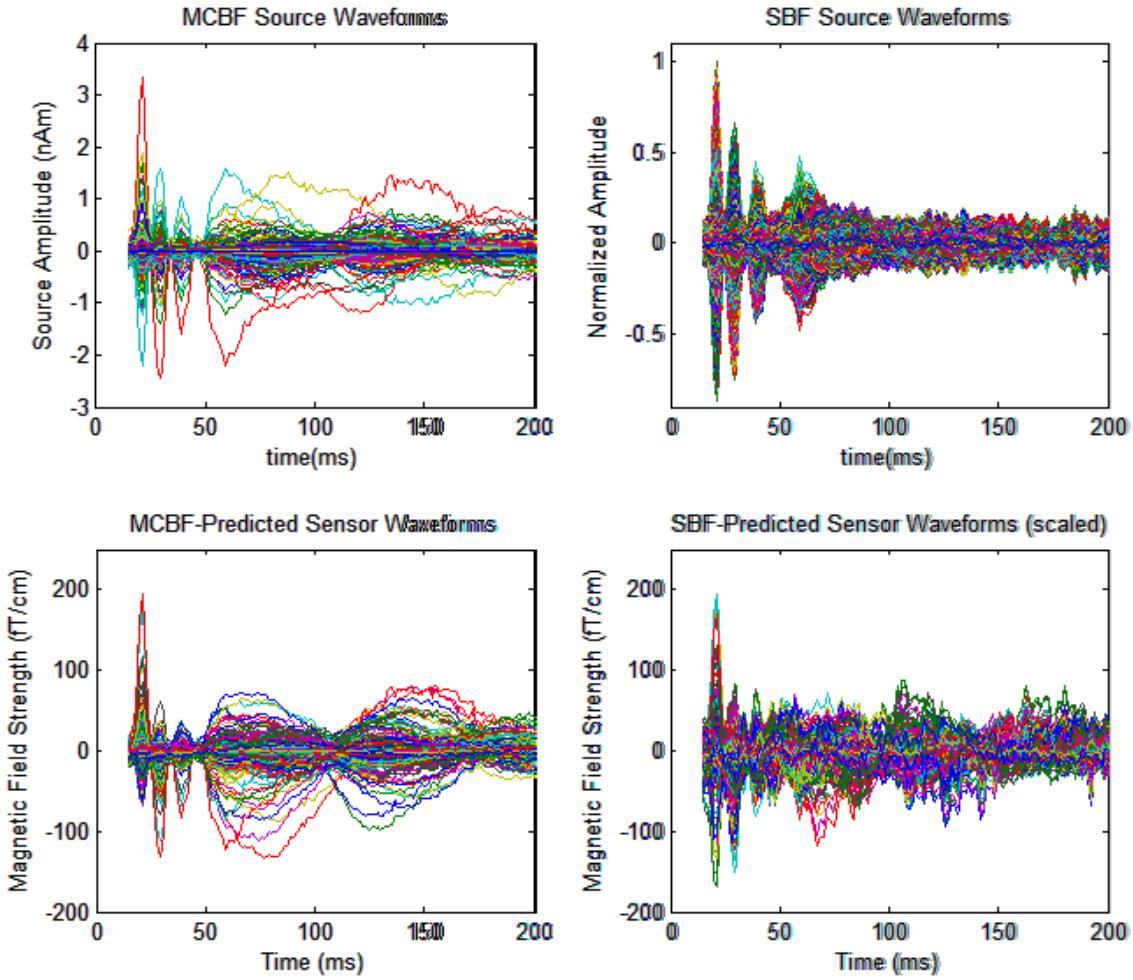

Figure 3.9: Reconstructed median-nerve source time-courses (top panels) and predicted MEG sensor waveforms (bottom panels) for the MCBF (left panels) and the SBF (right panel).
The sensor waveforms (gradiometers only) were computed from the reconstructed time-courses (respectively for each technique) via the same forward model used in the inverse solution estimation.

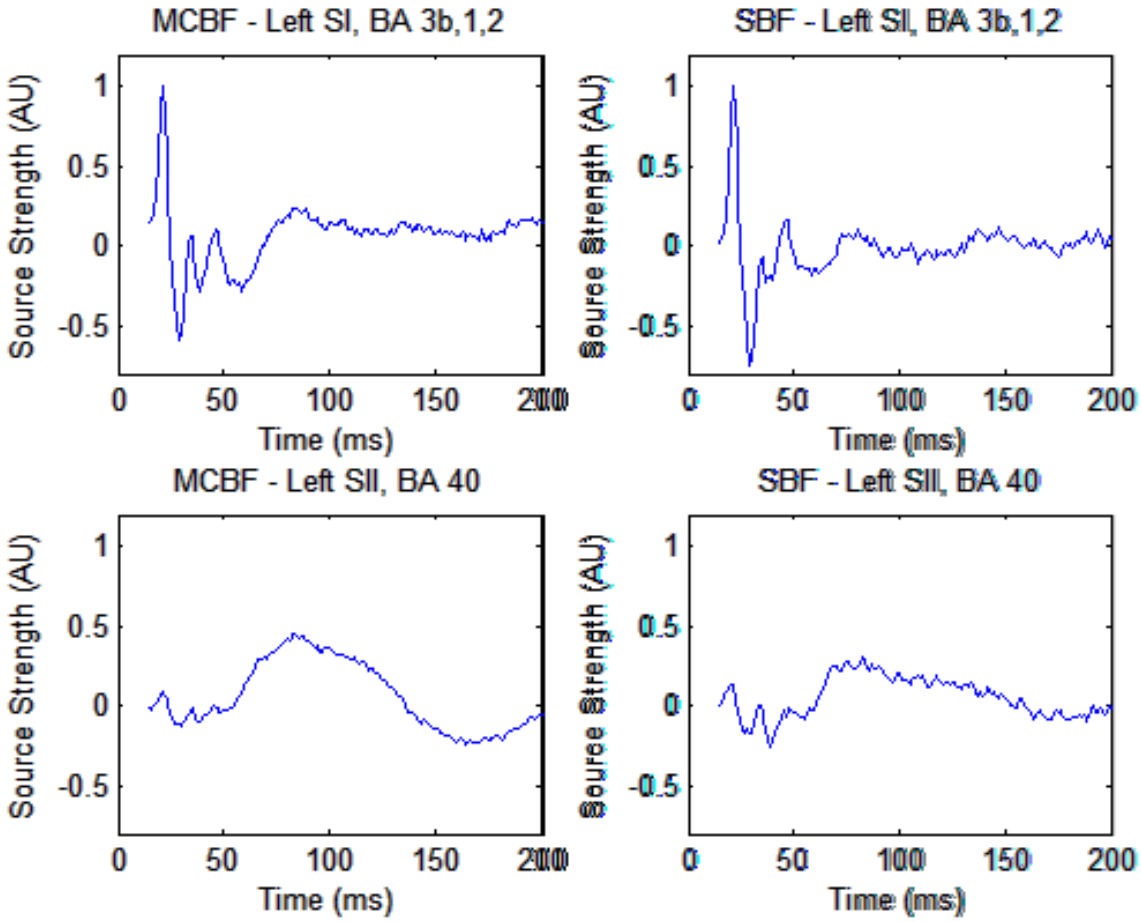

Figure 3.10: Individual reconstructed median-nerve time-courses for the S-I (BA 3b,1,2) region (top panels) and S-II (BA 40) region (bottom panels) for the MCBF (left panels) and the SBF (right panels).

References

Baldissera, F., Leocani, L., 1995. Afferent excitation of human motor cortex as revealed by enhancement of direct cortico-spinal actions on motoneurones. Electroencephalogr Clin Neurophysiol 97, 394-401.

Barba, C., Frot, M., Guenot, M., Mauguiere, F., 2001. Stereotactic recordings of median nerve somatosensory-evoked potentials in the human pre-supplementary motor area. Eur J Neurosci 13, 347-356.

Behzadi, Y., Restom, K., Liau, J., Liu, T.T., 2007. A component based noise correction method (CompCor) for BOLD and perfusion based fMRI. Neuroimage 37, 90-101.

Boakye, M., Huckins, S.C., Szeverenyi, N.M., Taskey, B.I., Hodge, C.J., Jr., 2000. Functional magnetic resonance imaging of somatosensory cortex activity produced by electrical stimulation of the median nerve or tactile stimulation of the index finger. J Neurosurg 93, 774-783.

Brookes, M.J., Gibson, A.M., Hall, S.D., Furlong, P.L., Barnes, G.R., Hillebrand, A., Singh, K.D., Holliday, I.E., Francis, S.T., Morris, P.G., 2004. A general linear model for MEG beamformer imaging. Neuroimage 23, 936-946.

Brookes, M.J., Hale, J.R., Zumer, J.M., Stevenson, C.M., Francis, S.T., Barnes, G.R., Owen, J.P., Morris, P.G., Nagarajan, S.S., 2011a. Measuring functional connectivity using MEG: methodology and comparison with fcMRI. Neuroimage 56, 1082-1104.

Brookes, M.J., Stevenson, C.M., Barnes, G.R., Hillebrand, A., Simpson, M.I., Francis, S.T., Morris, P.G., 2007. Beamformer reconstruction of correlated sources using a modified source model. Neuroimage 34, 1454-1465.

Brookes, M.J., Vrba, J., Robinson, S.E., Stevenson, C.M., Peters, A.M., Barnes, G.R., Hillebrand, A., Morris, P.G., 2008. Optimising experimental design for MEG beamformer imaging. Neuroimage 39, 1788-1802.

Brookes, M.J., Woolrich, M., Luckhoo, H., Price, D., Hale, J.R., Stephenson, M.C., Barnes, G.R., Smith, S.M., Morris, P.G., 2011b. Investigating the electrophysiological basis of resting state networks using magnetoencephalography. Proc Natl Acad Sci U S A 108, 16783-16788.

Brookes, M.J., Woolrich, M.W., Barnes, G.R., 2012. Measuring functional connectivity in MEG: a multivariate approach insensitive to linear source leakage. Neuroimage 63, 910-920.

Dalal, S.S., Sekihara, K., Nagarajan, S.S., 2006. Modified beamformers for coherent source region suppression. IEEE Trans Biomed Eng 53, 1357-1363.

Davidoff, R.A., 1990. The pyramidal tract. Neurology 40, 332-339.

de Pasquale, F., Della Penna, S., Snyder, A.Z., Lewis, C., Mantini, D., Marzetti, L., Belardinelli, P., Ciancetta, L., Pizzella, V., Romani, G.L., Corbetta, M., 2010. Temporal dynamics of spontaneous MEG activity in brain networks. Proc Natl Acad Sci U S A 107, 6040-6045.

Diwakar, M., Huang, M.X., Srinivasan, R., Harrington, D.L., Robb, A., Angeles, A., Muzzatti, L., Pakdaman, R., Song, T., Theilmann, R.J., Lee, R.R., 2011a. Dual-Core Beamformer for obtaining highly correlated neuronal networks in MEG. Neuroimage 54, 253-263.

Diwakar, M., Tal, O., Liu, T.T., Harrington, D.L., Srinivasan, R., Muzzatti, L., Song, T., Theilmann, R.J., Lee, R.R., Huang, M.X., 2011b. Accurate reconstruction of temporal correlation for neuronal sources using the enhanced dual-core MEG beamformer. Neuroimage 56, 1918-1928.

Forss, N., Hari, R., Salmelin, R., Ahonen, A., Hamalainen, M., Kajola, M., Knuutila, J., Simola, J., 1994. Activation of the human posterior parietal cortex by median nerve stimulation. Exp Brain Res 99, 309-315.

Forss, N., Jousmaki, V., 1998. Sensorimotor integration in human primary and secondary somatosensory cortices. Brain Res 781, 259-267.

Friston, K., Harrison, L., Daunizeau, J., Kiebel, S., Phillips, C., Trujillo-Barreto, N., Henson, R., Flandin, G., Mattout, J., 2008. Multiple sparse priors for the M/EEG inverse problem. Neuroimage 39, 1104-1120.

Fujiwara, N., Imai, M., Nagamine, T., Mima, T., Oga, T., Takeshita, K., Toma, K., Shibasaki, H., 2002. Second somatosensory area (SII) plays a significant role in selective somatosensory attention. Brain Res Cogn Brain Res 14, 389-397.

Hall, E.L., Woolrich, M.W., Thomaz, C.E., Morris, P.G., Brookes, M.J., 2013. Using variance information in magnetoencephalography measures of functional connectivity. Neuroimage 67, 203-212.

Hamalainen, M.S., Ilmoniemi, R.J., 1994. Interpreting magnetic fields of the brain: minimum norm estimates. Med Biol Eng Comput 32, 35-42.

Hari, R., Forss, N., 1999. Magnetoencephalography in the study of human somatosensory cortical processing. Philos Trans R Soc Lond B Biol Sci 354, 1145-1154.

Hari, R., Karhu, J., Hamalainen, M., Knuutila, J., Salonen, O., Sams, M., Vilkman, V., 1993. Functional organization of the human first and second somatosensory cortices: a neuromagnetic study. Eur J Neurosci 5, 724-734.

Hillebrand, A., Barnes, G.R., Bosboom, J.L., Berendse, H.W., Stam, C.J., 2012. Frequency-dependent functional connectivity within resting-state networks: an atlas-based MEG beamformer solution. Neuroimage 59, 3909-3921.

Hipp, J.F., Hawellek, D.J., Corbetta, M., Siegel, M., Engel, A.K., 2012. Large-scale cortical correlation structure of spontaneous oscillatory activity. Nat Neurosci 15, 884-890.

Huang, M., Davis, L.E., Aine, C., Weisend, M., Harrington, D., Christner, R., Stephen, J., Edgar, J.C., Herman, M., Meyer, J., Paulson, K., Martin, K., Lee, R.R., 2004a. MEG response to median nerve stimulation correlates with recovery of sensory and motor function after stroke. Clin Neurophysiol 115, 820-833.

Huang, M.X., Aine, C., Davis, L., Butman, J., Christner, R., Weisend, M., Stephen, J., Meyer, J., Silveri, J., Herman, M., Lee, R.R., 2000. Sources on the anterior and posterior banks of the central sulcus identified from magnetic somatosensory evoked responses using multistart spatio-temporal localization. Hum Brain Mapp 11, 59-76.

Huang, M.X., Dale, A.M., Song, T., Halgren, E., Harrington, D.L., Podgorny, I., Canive, J.M., Lewis, S., Lee, R.R., 2006. Vector-based spatial-temporal minimum L1-norm solution for MEG. Neuroimage 31, 1025-1037.

Huang, M.X., Harrington, D.L., Paulson, K.M., Weisend, M.P., Lee, R.R., 2004b. Temporal dynamics of ipsilateral and contralateral motor activity during voluntary finger movement. Hum Brain Mapp 23, 26-39.

Huang, M.X., Lee, R.R., Miller, G.A., Thoma, R.J., Hanlon, F.M., Paulson, K.M., Martin, K., Harrington, D.L., Weisend, M.P., Edgar, J.C., Canive, J.M., 2005. A parietal-frontal network studied by somatosensory oddball MEG responses, and its cross-modal consistency. Neuroimage 28, 99-114.

Huang, M.X., Song, T., Hagler, D.J., Jr., Podgorny, I., Jousmaki, V., Cui, L., Gaa, K., Harrington, D.L., Dale, A.M., Lee, R.R., Elman, J., Halgren, E., 2007. A novel integrated MEG and EEG analysis method for dipolar sources. Neuroimage 37, 731-748.

Hui, H.B., Leahy, R.M., 2006. Linearly constrained MEG beamformers for MVAR modeling of cortical interactions. 3rd IEEE International Symposium on Biomedical Imaging: Nano to Macro, pp. 237–240.

Hui, H.B., Pantazis, D., Bressler, S.L., Leahy, R.M., 2010. Identifying true cortical interactions in MEG using the nulling beamformer. Neuroimage 49, 3161-3174.

Jenkinson, M., Beckmann, C.F., Behrens, T.E., Woolrich, M.W., Smith, S.M., 2012. Fsl. Neuroimage 62, 782-790.

Jones, E.G., Coulter, J.D., Hendry, S.H., 1978. Intracortical connectivity of architectonic fields in the somatic sensory, motor and parietal cortex of monkeys. J Comp Neurol 181, 291-347.

Jones, E.G., Wise, S.P., Coulter, J.D., 1979. Differential thalamic relationships of sensory-motor and parietal cortical fields in monkeys. J Comp Neurol 183, 833-881.

Jousmaki, V., Forss, N., 1998. Effects of stimulus intensity on signals from human somatosensory cortices. Neuroreport 9, 3427-3431.

Kandel, E.R., Schwartz, J.H., Jessel, T.M., 2000. Principles of Neural Science. McGraw Hill, New York.

Kawamura, T., Nakasato, N., Seki, K., Kanno, A., Fujita, S., Fujiwara, S., Yoshimoto, T., 1996. Neuromagnetic evidence of pre- and post-central cortical sources of somatosensory evoked responses. Electroencephalogr Clin Neurophysiol 100, 44-50.

Kumihashi, I., Sekihara, K., 2010. Array-gain constraint minimum-norm spatial filter with recursively updated gram matrix for biomagnetic source imaging. IEEE Trans Biomed Eng 57, 1358-1365.

Lemon, R.N., 1981. Functional properties of monkey motor cortex neurones receiving afferent input from the hand and fingers. J Physiol 311, 497-519.

Lemon, R.N., Porter, R., 1976. Proceedings: Natural afferent input to movement-related neurones in monkey pre-central cortex. J Physiol 258, 18P-19P.

Lemon, R.N., van der Burg, J., 1979. Short-latency peripheral inputs to thalamic neurones projecting to the motor cortex in the monkey. Exp Brain Res 36, 445-462.

Liu, Z., Fukunaga, M., de Zwart, J.A., Duyn, J.H., 2010. Large-scale spontaneous fluctuations and correlations in brain electrical activity observed with magnetoencephalography. Neuroimage 51, 102-111.

Luckhoo, H., Hale, J.R., Stokes, M.G., Nobre, A.C., Morris, P.G., Brookes, M.J., Woolrich, M.W., 2012. Inferring task-related networks using independent component analysis in magnetoencephalography. Neuroimage 62, 530-541.

Mantini, D., Della Penna, S., Marzetti, L., de Pasquale, F., Pizzella, V., Corbetta, M., Romani, G.L., 2011. A signal-processing pipeline for magnetoencephalography resting-state networks. Brain Connect 1, 49-59.

Mantini, D., Perrucci, M.G., Del Gratta, C., Romani, G.L., Corbetta, M., 2007. Electrophysiological signatures of resting state networks in the human brain. Proc Natl Acad Sci U S A 104, 13170-13175.

Mauguiere, F., Merlet, I., Forss, N., Vanni, S., Jousmaki, V., Adeleine, P., Hari, R., 1997a. Activation of a distributed somatosensory cortical network in the human brain. A dipole modelling study of magnetic fields evoked by median nerve stimulation. Part I: Location and activation timing of SEF sources. Electroencephalogr Clin Neurophysiol 104, 281-289.

Mauguiere, F., Merlet, I., Forss, N., Vanni, S., Jousmaki, V., Adeleine, P., Hari, R., 1997b. Activation of a distributed somatosensory cortical network in the human brain: a dipole modelling study of magnetic fields evoked by median nerve stimulation. Part II: Effects of stimulus rate, attention and stimulus detection. Electroencephalogr Clin Neurophysiol 104, 290-295.

McGlone, F., Kelly, E.F., Trulsson, M., Francis, S.T., Westling, G., Bowtell, R., 2002. Functional neuroimaging studies of human somatosensory cortex. Behav Brain Res 135, 147-158.

Moiseev, A., Gaspar, J.M., Schneider, J.A., Herdman, A.T., 2011. Application of multi-source minimum variance beamformers for reconstruction of correlated neural activity. Neuroimage 58, 481-496.

Moiseev, A., Herdman, A.T., 2013. Multi-core beamformers: derivation, limitations and improvements. Neuroimage 71, 135-146.

Mosher, J.C., Leahy, R.M., Lewis, P.S., 1999. EEG and MEG: forward solutions for inverse methods. IEEE Trans Biomed Eng 46, 245-259.

Owen, J.P., Wipf, D.P., Attias, H.T., Sekihara, K., Nagarajan, S.S., 2012. Performance evaluation of the Champagne source reconstruction algorithm on simulated and real M/EEG data. Neuroimage 60, 305-323.

Quraan, M.A., Cheyne, D., 2010. Reconstruction of correlated brain activity with adaptive spatial filters in MEG. Neuroimage 49, 2387-2400.

Robinson, S., Vrba, J., 1998. Functional neuroimaging by synthetic aperture magnetometry. Tohoku Univ. Press, Sendai.

Rosen, I., Asanuma, H., 1972. Peripheral afferent inputs to the forelimb area of the monkey motor cortex: input-output relations. Exp Brain Res 14, 257-273.

Sekihara, K., Nagarajan, S.S., Poeppel, D., Marantz, A., 2002. Performance of an MEG adaptive-beamformer technique in the presence of correlated neural activities: effects on signal intensity and time-course estimates. IEEE Trans Biomed Eng 49, 1534-1546.

Sekihara, K., Nagarajan, S.S., Poeppel, D., Marantz, A., 2004. Asymptotic SNR of scalar and vector minimum-variance beamformers for neuromagnetic source reconstruction. IEEE Trans Biomed Eng 51, 1726-1734.

Sekihara, K., Nagarajan, S.S., 2008. Adaptive Spatial Filters for Electormagnetic Brain Imaging. SpringerLink, Berlin.

Simoes, C., Jensen, O., Parkkonen, L., Hari, R., 2003. Phase locking between human primary and secondary somatosensory cortices. Proc Natl Acad Sci U S A 100, 2691-2694.

Singer, W., 1999. Neuronal synchrony: a versatile code for the definition of relations? Neuron 24, 49-65, 111-125.

Song, T., Cui, L., Gaa, K., Feffer, L., Taulu, S., Lee, R.R., Huang, M., 2009. Signal space separation algorithm and its application on suppressing artifacts caused by vagus nerve stimulation for magnetoencephalography recordings. J Clin Neurophysiol 26, 392-400.

Song, T., Gaa, K., Cui, L., Feffer, L., Lee, R.R., Huang, M., 2008. Evaluation of signal space separation via simulation. Med Biol Eng Comput 46, 923-932.

Spiegel, J., Tintera, J., Gawehn, J., Stoeter, P., Treede, R.D., 1999. Functional MRI of human primary somatosensory and motor cortex during median nerve stimulation. Clin Neurophysiol 110, 47-52.

Tal, O., Diwakar, M., Wong, C.W., Olafsson, V., Lee, R., Huang, M.X., Liu, T.T., 2013. Caffeine-Induced Global Reductions in Resting-State BOLD Connectivity Reflect Widespread Decreases in MEG Connectivity. Front Hum Neurosci 7, 63.

Taulu, S., Kajola, M., Simola, J., 2004. Suppression of interference and artifacts by the Signal Space Separation Method. Brain Topogr 16, 269-275.

Taulu, S., Simola, J., 2006. Spatiotemporal signal space separation method for rejecting nearby interference in MEG measurements. Phys Med Biol 51, 1759-1768.

Tesche, C.D., 1996. Non-invasive imaging of neuronal population dynamics in human thalamus. Brain Res 729, 253-258.

Urbano, A., Babiloni, F., Babiloni, C., Ambrosini, A., Onorati, P., Rossini, P.M., 1997. Human short latency cortical responses to somatosensory stimulation. A high resolution EEG study. Neuroreport 8, 3239-3243.

Van Drongelen, W., Yuchtman, M., Van Veen, B.D., Van Huffelen, A.C., 1996. A spatial filtering technique to detect and localize multiple sources in the brain. Brain Topogr 9, 39-49.

Van Veen, B.D., van Drongelen, W., Yuchtman, M., Suzuki, A., 1997. Localization of brain electrical activity via linearly constrained minimum variance spatial filtering. IEEE Trans Biomed Eng 44, 867-880.

Waberski, T.D., Gobbele, R., Darvas, F., Schmitz, S., Buchner, H., 2002. Spatiotemporal imaging of electrical activity related to attention to somatosensory stimulation. Neuroimage 17, 1347-1357.

Wipf, D., Nagarajan, S., 2009. A unified Bayesian framework for MEG/EEG source imaging. Neuroimage 44, 947-966.

Wipf, D.P., Owen, J.P., Attias, H.T., Sekihara, K., Nagarajan, S.S., 2010. Robust Bayesian estimation of the location, orientation, and time course of multiple correlated neural sources using MEG. Neuroimage 49, 641-655.

Wong, Y.C., Kwan, H.C., MacKay, W.A., Murphy, J.T., 1978. Spatial organization of precentral cortex in awake primates. I. Somatosensory inputs. J Neurophysiol 41, 1107-1119.

Wood, C.C., Cohen, D., Cuffin, B.N., Yarita, M., Allison, T., 1985. Electrical sources in human somatosensory cortex: identification by combined magnetic and potential recordings. Science 227, 1051-1053.

Zumer, J.M., Attias, H.T., Sekihara, K., Nagarajan, S.S., 2007. A probabilistic algorithm integrating source localization and noise suppression for MEG and EEG data. Neuroimage 37, 102-115.

CHAPTER 4

Introduction

In recent times, connectivity (i.e. functional relation) between spatially distinct regions in the brain has become a key matter of study in the field of neuroscience. Such functional connectivity (FC) measures have been commonly used as means for identifying and characterizing resting-state brain activity and distributed network formation (Beckmann et al., 2005; Smith et al., 2009). Typically this uses functional magnetic resonance imaging (fMRI) in spite of the fact that it provides only an indirect measure of neural activity due to the signal's hemodynamic basis (Buxton et al., 2004). Furthermore, the modality's limited temporal resolution due to the signal broadening inherent to the hemodynamic response restricts its ability to fully investigate the underlying, rapid neural fluctuations believed to be responsible for the observed fMRI manifestations (Schnitzler and Gross, 2005; Singer, 1999). These confounds can be avoided by utilizing direct measures of electrophysiology, such as magnetoencephalography (MEG), which detects extra-cranial magnetic fields produced by synchronized neural currents (Hamalainen et al., 1993). Indeed, recent work with MEG has identified a number of the networks commonly observed with fMRI (Brookes et al., 2011a; Brookes et al., 2011b; Hipp et al., 2012).

In order to project the externally collected MEG data onto the brain (i.e. source space), FC analyses (Brookes et al., 2011a; Brookes et al., 2012a; Brookes et al., 2011b; Hall et al., 2013; Hillebrand et al., 2012; Hipp et al., 2012; Luckhoo et al., 2012; Mantini et al., 2011; Tal et al., 2013) routinely use an adaptive spatial filter known as the

minimum-variance single beamformer (SBF) (Robinson, 1998; Sekihara et al., 2002; Van Drongelen, 1996; Van Veen et al., 1997). Although compelling to use due to robust performance in low signal-to-noise conditions (e.g. resting-state measurements) and ease of implementation, the SBF reconstructions are susceptible to inter-source correlations, resulting in source amplitude suppression and time-course distortion (Brookes et al., 2007; Dalal et al., 2006; Diwakar et al., 2011a; Diwakar et al., 2011b; Hui and Leahy, 2006; Hui et al., 2010; Moiseev et al., 2011; Moiseev and Herdman, 2013; Quraan and Cheyne, 2010). Considering that spontaneous and non-averaged task related (e.g. eye tracking) neural activity is known to involve synchronous communication between multiple sources (Singer, 1999), the use of SBF as a tool for FC analysis could be questionable (Moiseev and Herdman, 2013). Furthermore, due to the ill-posed nature of the inverse problem, certain dependencies in the projected signals could exist between spatially separate voxels resulting in the phenomenon known as signal leakage. This can be a hindrance to assessing MEG dynamics (FC and resting-state network formation) as signal leakage will introduce spurious connectivity measures (Brookes et al., 2012b). The SBF also suffers from strong spatial bias towards the head's center due to a non-uniform lead-field (Kumihashi and Sekihara, 2010; Sekihara, 2008), an effect which can be reduced using the array-gain constraint (Sekihara, 2008), but at the cost of incorrect relative scaling among sources as we have shown in Chapter 3.

Beamformers that are less sensitive to the presence of underlying source correlation, signal leakage and spatial bias could potentially lead to improved estimates of resting-state FC and network characterization (Brookes et al., 2012b; Moiseev and Herdman, 2013). In chapter 3 we introduced and analyzed the *multi-core beamformer*

(MCBF) combined with an iterative algorithm and used both complex simulations and evoked neuromagnetic data measurements to demonstrate the method's ability to successfully reconstruct sources regardless of their correlation and minimize signal leakage and spatial bias.

Application of the SBF in spontaneous FC studies has been largely justified by hypothesizing that the nature of correlated neuronal oscillations in the resting-state is short-lived and thus, should have little impact on time-course reconstruction (Brookes et al., 2011b). However, this would truly be unverifiable using the SBF, as its inherent limitation hinders accurate examination of the underlying correlations among the supposed "resolved" sources. As the MCBF innately bypasses this obstacle, and even further, curtails signal leakage distortions as well as accurately and precisely reconstructs source features, it is conceivably the better tool for spontaneous FC investigations (Moiseev and Herdman, 2013).

In this chapter, we look further into the matter and compare the reconstruction performance of the SBF to the MCBF using resting-state measurements collected previously for Tal et al. (2013) by recomputing the study's results with the MCBF. We also employ CHAMPAGNE, an L2 minimum-norm iterative solution developed by Wipf et al. (2010) which is insensitive to source correlation as well. In addition, we apply independent component analysis (ICA) to the spontaneous source data reconstructed by SBF and MCBF in order to extract resting-state networks (RSNs). The SBF and MCBF networks' spatial extent are compared to each other as well as their established fMRI analogues (Smith et al., 2009). Such insights should help determine whether SBF reconstructions are adequate for spontaneous MEG FC estimations.

Materials and Methods

Data from a previous study are employed; all experimental and data processing procedures have been previously published (Tal et al., 2013) and are repeated here for the reader's convenience.

Experimental Protocol

Twelve healthy volunteers were initially enrolled in this study after providing informed consent. Two subjects were not able to complete the study due to excessive motion and dental artifacts, resulting in a final sample size of 10 subjects (4 males and 6 females; ages 21 to 33 years; mean of 25.6 years). To minimize potential confounds due to differing levels of caffeine consumption (Jones et al., 2000; Reeves et al., 2002), we recruited subjects with low levels of caffeine usage (<50 mg/day). Participants were instructed to abstain from caffeine for 24 hours prior to being scanned, as well as to maintain low caffeine consumption for a two month period prior to the beginning of the study and throughout the entire duration of the study.

The study employed a double-blind, placebo-controlled, repeated measures design. For each modality (MEG and fMRI), each subject participated in two independent imaging sessions, a control session and a caffeine session, where the order of the two sessions was random. Each of the four imaging sessions (MEG control and caffeine; fMRI control and caffeine) was separated from the other sessions by at least two weeks. Half the subjects started with MEG sessions while the other half started with fMRI sessions. Each session consisted of a pre-dose section and a post-dose section, with each MEG and fMRI section lasting about 30 and 60 minutes, respectively. After the pre-dose section, subjects were taken out of the MEG or MRI scanner and asked to ingest a

capsule containing 200 mg of caffeine or placebo. A forty minute period was allotted between capsule ingestion and the first functional scan of the post-dose section, as previous studies have shown that the absorption of caffeine from the gastrointestinal tract reaches 99% about forty five minutes post ingestion (Fredholm et al., 1999).

Each MEG scan section consisted of four 5 minute resting-state scans, two with eyes closed (EC) and two with eyes open (EO), in the following order: EC, EO, EC and EO. Subjects were instructed to stay awake, keep their mind blank and their hands open, laying flat. During EO resting-state scans, participants were asked to visually fixate on a black cross placed on a white screen, while during the EC resting-state scans they were asked to keep their eyes closed and to imagine the black cross. In this chapter, our analysis will focus primarily on the EC scans from the MEG sessions.

Data Acquisition and Processing

MEG data were measured using an Elekta/NeuromagTM whole-head MEG system with 204 gradiometers and 102 magnetometers in a magnetically shielded room (IMEDCO-AG, Switzerland). Electro-oculogram (EOG) electrodes were used to record eye blinks and movements. Data were sampled at 1000 Hz and pre-processed using MaxFilter (NeuromagTM) to remove environmental noise and signal artifacts due to magnetic interference from sources outside the brain (Song et al., 2009; Song et al., 2008; Taulu et al., 2004; Taulu and Simola, 2006). Temporal independent components analysis (ICA) was applied to the data using the fastICA algorithm (http://research.ics.tkk.fi/ica/fastica), and artifact-related independent components due to eye blinks, cardiac activity, and instrument-related activity were removed based on visual inspection of their temporal and spatial signatures (typically removing 1-3 components).

Using the high-resolution anatomical data obtained in the MRI scan, a boundary-element based triangular mesh of 5-mm mesh size was generated for each subject from their inner-skull surface. FreeSurfer was used to define a fixed source grid (7mm spacing) on the brain's gray-white matter boundary, which was then divided into cortical regions of interest using the FreeSurfer computed parcellations (Desikan et al., 2006). With the inner-skull triangular mesh and gray-matter source grid, the MEG forward model calculation for the lead-field (gain) matrix was performed using a boundary element model (Huang et al., 2007; Mosher et al., 1999). Registration of MRI and MEG data was performed using positioning information obtained with a Polhemus Isotrak system prior to each MEG session.

In our analysis, we considered MEG data both within a wide-band range of 1-50 Hz and within the following bands: delta (δ) – 1-4 Hz, theta (θ) – 4-8 Hz, alpha (α) – 8-13 Hz, low and high beta (β) – 13-20 Hz & 20-30 Hz, respectively, and low gamma (γ) – 30-50 Hz. The frequency filtered MEG data were then projected into source space using the array-gain constraint minimum-variance regularized vector beamformer (Robinson, 1998; Sekihara, 2008; Van Drongelen, 1996; Van Veen et al., 1997), the multi-core beamformer (Diwakar et al., 2011b) in tandem with the proposed iterative algorithm (Chapter 3) as well as CHAMPAGNE (Wipf et al., 2010), yielding a set of bandlimited time-courses (at each source location) for each of the reconstruction techniques. The regularization level was set uniquely for each individual MEG recording by utilizing a modified "broken-stick" model as described in (Behzadi et al., 2007) which helps to identify the meaningful (data-related) principal components. A statistical distribution of expected eigenvalues, derived from random normally distributed data with rank and

Frobenius norm equal to that of the MEG data of interest, was used for comparison and determination of the noise level (i.e., the number of significant ($p < 0.05$) modes). The value of the first non-significant (noise) component then represented the cut-off and was used as the regularization parameter. Reconstructed source time-courses were then Hilbert transformed to obtain the analytic signal. The envelope of oscillatory power fluctuations was obtained from the absolute value of the analytic signal and this envelope time course was then epoched into 500ms blocks, following the approach of (Brookes et al., 2011a).

Connectivity Measures

For each subject, we used the FreeSurfer cortical parcellations (Desikan et al., 2006) to define anatomical regions of interest (ROIs). As described in (Wong et al., 2012), we discarded ROIs for which any subject had less than 5 voxels within a region, resulting in a total of 40 ROIs (20 per hemisphere). A central source for each of the cortical ROIs was defined as the source with the smallest mean path length to all the other sources within the ROI. Next, a sphere-shaped region was defined to include every source that was both within 12 mm of the central source and contained within the same ROI. Envelope time-courses within this region were then averaged to provide a final average MEG time-course for each ROI. To assess connectivity, we computed the Pearson correlation coefficient (r) between the average time-courses for each pair of ROIs (780 pairs). For each modality, the correlation coefficient was computed for each of the four acquisition sections (pre-dose and post-dose sections of both the Control and Caffeine sessions). The correlation coefficients from repeated scans (e.g. the two pre-dose EC scans) were averaged. For quantitative assessments, the Pearson correlation

scores were converted to the Fisher z-scores using the Fisher transformation (Luckhoo et al., 2012). The change in the z-score metric (Δz = post-dose z-score minus pre-dose z-score) in each session (caffeine and control) was calculated, and a repeated measures two-way analysis of variance (ANOVA) (Keppel and Wickens, 2004) was then used to examine the effects of two factors on the measured connectivity: (1) the effect of caffeine/control and (2) the effect of ROI pair (Wong et al., 2012).

Preliminary Post-processing ICA

Following the approach of Brookes et al. (2011b), temporal ICA was applied to the data using the fastICA algorithm (Hyvarinen, 1999) to extract the resting-state networks' (RSNs) spatial configurations. Prior to ICA, data were prewhitened and reduced to thirty principal components and twenty-five independent components (ICs) were obtained (Brookes et al., 2011b). For each IC, the Pearson correlation between its time-course and the time-course of every voxel was computed and the correlation values were then combined to form a RSN spatial map, resulting in a series of RSNs maps. The spatial similarity of the MEG RSNs maps to previously published fMRI RSN maps derived from spatial ICA (Smith et al., 2009) were quantified using a spatial Pearson correlation coefficient measure (only voxels within the brain included).

Results

Source Time-courses

For a representative subject, the projected source time-courses from a single run (5 min) in the control session are shown in Figure 4.1 for the SBF, the MCBF and CHAMPAGNE. A qualitative review reveals that although source waveform shape and structure is generally similar (i.e. activity peaks match temporally and in magnitude), the

overall neural activity is noticeably represented by a smaller number of sources with the MCBF than with the SBF, indicating that signal leakage reduction effects of the algorithm presented in Chapter 3 extend to resting-state analyses as well. CHAMPAGNE time-courses appear to fall somewhere in the middle: although less source time-courses seem to be used than SBF, signal leakage is still more apparent than with the MCBF.

Analysis of Data from Caffeine Study

To qualitatively compare the two reconstruction techniques, the figures presented in (Tal et al., 2013) were reproduced. For the same representative subject, Pearson correlation coefficient matrices are displayed in Figure 4.2 indicating the degree of connectivity in the eyes closed (EC) condition for all ROI pairs for each of the four scan sections (pre-dose and post-dose sections of the caffeine and control session). The SBF connectivity matrices are shown in the top, while the MCBF and CHAMPAGNE are shown in the bottom left and the right hand sides of the figure, respectively (the SBF matrices are similar to those previously presented in (Tal et al., 2013)). The connectivity metrics were obtained using the wide-band frequency range (1-50Hz). As before, correlations in the post-dose caffeine data are visibly lower than in the pre-dose caffeine data, indicating a caffeine-induced global decrease in this subject's connectivity, while there is not a widespread difference between the pre-dose and post-dose correlations in the control session. Although some individual ROI pairs might slightly differ in their value, a consensus in the subject's global connectivity exists among the three reconstruction approaches for each of the four sessions.

Similarly, group results were also recomputed. Figure 4.3 shows the changes in z-score (post-dose minus pre-dose) averaged across subjects and sessions (control and

caffeine – EC condition), with the changes for SBF, MCBF and CHAMPAGNE shown in the top, middle and bottom panels of the figure, respectively. The upper triangle of each matrix shows the mean changes in the z-score metric (across subjects) for all ROI pairs, while the lower triangle shows the t-statistics of those ROI pairs that exhibited a significant ($p < 0.05$) change in connectivity across the sample. Significant decreases and increases in z-scores are indicated by blue and red hues, respectively. From a qualitative perspective, broad decreases in connectivity can be observed for the caffeine data while the control data shows fewer significant changes than the caffeine data. It is noted that in the control data (where minimal changes are expected to be seen as minimal physical changes in subject state are expected to occur between pre-dose and post-dose sections), MCBF and CHAMPAGNE showed fewer significant ROI pairs than the SBF, perhaps indicating that false connectivity changes due to signal leakage are reduced. The quantitative assessment of the data provided by two-way repeated measures ANOVA is shown in Table 4.1. For all reconstruction techniques, the caffeine/control factor showed a significant effect ($p \leq 0.0065$, $p \leq 0.0058$ and $p \leq 0.0089$ for SBF, MCBF and CHAMPAGNE, respectively), indicating that the change in correlation was significantly different between the caffeine and control sessions as well as that the projection approach of choice did not substantially affect the computed global group statistical measures. A one-way ANOVA (factor being reconstruction method) conducted on the observed mean global (averaged across ROI pairs) connectivity reductions for all the subjects (including both control and caffeine session values) showed no difference to exist between the results provided the three techniques ($p = 0.94$). Post-hoc two-tailed t-tests further validated no that significant difference existed between the reconstruction methods

results ($p > 0.22$ for all three comparison cases). However, we note that if examining just the absolute correlation values themselves instead of the changes across sections (one-way ANOVA still insignificant with $p = 0.4$), equivalent post-hoc t-tests comparing the three approaches shows significant changes when comparing CHAMPAGNE with SBF or MCBF ($p < 1e\text{-}8$) but not in between MCBF and SBF ($p = 0.63$).

Band-specific (frequency bands defined in Methods) mean connectivity changes across all ROIs are compared in Figure 4.4 (displayed in the same manner as the wide-band data in Figure 4.3). Widespread decreases in z-scores are evident in the caffeine data across all bands regardless of reconstruction technique, with the strongest reductions appearing in the α, low β and high β bands. As was seen with the wide-band control data, MCBF and CHAMPAGNE appear to result in fewer significant ROI pairs (with the exception of the Δ band), potentially implying a reduction in signal leakage. The quantitative assessment using the two-way repeated measures ANOVA (Tables 4.2, 4.3 and 4.4 for SBF, MCBF and CHAMPAGNE, respectively) revealed that in both approaches only the θ, low β and high β bands showed a significant main effect ($p \leq 0.05$) of the caffeine/control factor (interaction term not significant for any of the bands with significant main effect). Interestingly, the ANOVA results from the MCBF and CHAMPAGNE data were more conservative when estimating significance (i.e. larger p-values). This could follow from reduction of spurious connectivity due to signal leakage, where ROI pairs whose signal was "leaked" (i.e. not truly belonging there) and were demonstrating a false positive significance, are now without any signal and consequently not significant.

Resting-State ICA Analysis

For a representative subject, a single run (5-min acquisition) was used to generate two sets of twenty-five independent RSN spatial maps (from the SBF and MCBF reconstructed time-courses, respectively). The results were matched to their 10 known fMRI analogues by means of a spatial correlation (i.e. resulting in a 25x10 matrix of correlation coefficients). As an example, the strongest MEG complements of the fMRI motor network are displayed for the SBF, MCBF and CHAMPAGNE data in Figure 4.5. Although the degree of correspondence (i.e. correlation to fMRI RSN) was similar for the three methods (0.45, 0.48 and 0.42 for SBF, MCBF and CHAMPAGNE respectively), a visual comparison does seem to indicate a somewhat less defined motor RSN in the SBF and CHAMPAGNE maps than in the MCBF map, perhaps suggestive of increased signal leakage effects (same thresholding was applied for both maps: 98.5^{th} and 99.9^{th} percentile of the data's cumulative distribution function (CDF) for red and yellow, respectively). It is interesting to note that the MEG motor RSNs were mainly restricted to a single hemisphere (for a given IC), while generally the fMRI motor RSNs are known to be captured bilaterally. Four 5-min acquisitions (all control runs) were concatenated to enhance IC map spatial definition. Results shown for SBF, MCBF and CHAMPAGNE (Figure 4.6) exhibit improved RSN spatial extent (in comparison to maps from the single run), yet the MCBF motor map still seemed to maintain its edge in RSN spatial definition when compared to the SBF and CHAMPAGNE motor maps. Other examples of MEG RSN maps resembling known fMRI networks are shown for MCBF, such as the visual network (Figure 4.7) and executive network (Figure 4.8). It is noted that when comparing the amount of correspondence for the best matching maps across the 10 maps, similar patterns of spatial correlation are observed regardless of reconstruction (i.e. if a resolved

SBF network has a high degree of spatial matching, then so would the respective MCBF network, and vice versa). This suggests that although signal leakage (voxel nonindependence) is reduced by using MCBF, due to ICA's inherent nature of extracting independent features it may be somewhat resistant to leakage effects, and thus both techniques result in comparable ICA maps suggesting that the utilization of the advanced may not provide significant advantages MCBF.

Conclusions

Although commonly used to reconstruct MEG data collected in resting-state functional connectivity analyses (Brookes et al., 2011a; Brookes et al., 2012a; Brookes et al., 2011b; Hall et al., 2013; Hillebrand et al., 2012; Hipp et al., 2012; Luckhoo et al., 2012; Mantini et al., 2011; Tal et al., 2013), the minimum-variance single beamformer is vulnerable to the presence of inter-source correlations (Brookes et al., 2007; Dalal et al., 2006; Diwakar et al., 2011a; Diwakar et al., 2011b; Hui and Leahy, 2006; Hui et al., 2010; Moiseev et al., 2011; Moiseev and Herdman, 2013; Quraan and Cheyne, 2010), believed to exist during spontaneous and non-averaged task related neural activities (Singer, 1999). Artifacts due to the ill-posed inverse problem such as spatial leakage (Brookes et al., 2012b) and bias towards the center of the brain (Kumihashi and Sekihara, 2010; Sekihara, 2008) further provide complications for resting-state FC analyses, placing its use for such tasks under question (Brookes et al., 2012b; Moiseev and Herdmann, 2013). In this chapter, we attempted to determine whether these factors were strong enough to affect resting-state MEG functional measurements (e.g. connectivity) and the associated interpretation of the measures (e.g. ROI based changes, resting-state networks).

First, re-examination of the resting-state MEG data collected for the caffeine study (Tal et al., 2013) was completed using both the SBF, the MCBF (Diwakar et al., 2011b) combined with the iterative algorithm (Chapter 4) and CHAMPAGNE (Wipf et al. 2010) where the latter two methods have been shown to be immune to such concerns. Interestingly, while the significance of connectivity changes in individual ROI-to-ROI connectivity measures did differ across certain pairs (for the group data), the observed global behavior (i.e. connectivity reductions) and corresponding statistical measures remained alike (for both the wideband and band-limited data). We noted that the apparent visual reduction in significant ROI pairs (when comparing the MCBF and CHAMPAGNE results to the SBF) is attributed perhaps to the minimization of signal leakage effects (i.e. less voxels exhibiting spurious connectivity resulting in false-positive significance). However, given that the global observations did not differ wildly between the two, it seems safe to suggest that underlying source connectivity in spontaneous conditions is minimal enough that the SBF observations can be trusted. We would not recommend the same when attempting to look specific ROI pairs, as clearly disagreement exists between the two on numerous occasions. If one must employ SBF, a secondary measurement (e.g. signal amplitude) should be used to truly verify the existence of a source in that location (as leaked, "weak" signals can result in artifactual connectivity), prior to concluding a significant connectivity change. Second, ICA was employed to extract resting-state networks from SBF, MCBF and CHAMPAGNE reconstructed data. Although better spatial definition was apparent for the MCBF RSNs, the differences were no large enough to justify employment of either MCBF or CHAMPAGNE over SBF.

We note that our work on characterization of MEG RSNs using temporal ICA is extremely preliminary. Foremost, a full quantitative assessment is needed for proper characterization and comparison of the resolved RSNs. Also, networks presented in the established fMRI (Smith et al., 2009) and MEG (Brookes et al., 2011b) literature were obtained by the concatenation of data from numerous subjects (36 and 10, respectively), as such subject-based averaging facilitates the identification of spatially distinct RSN maps. At this time, we have only employed a single subject due to an inability to apply a common pre-processing step of data mean and variance normalization, which normally takes place when concatenating datasets (to help minimize unwanted discrepancies in the grouped signals from affecting the ICA process). This is an unfortunate outcome due to the "sparser" features of the MCBF reconstruction technique which translates to voxels (sources) whose time-courses have near zero amplitudes and variances. As such activity-less locations (voxels) tend to vary across sessions and subjects, improper magnifications of source time-courses may occur resulting in failure during the ICA process. Better understanding of this phenomenon and developing means to address the difficulties which arise from it are critical for any future assessments of multi-subject resting-state MEG data which utilize ICA analysis.

Contrary to expectations based on the observations in Chapter 4, the preliminary investigation suggests that the SBF can serve as a projection tool for spontaneous MEG data when conclusions are to be made on the global level (i.e. changes seen across the entire brain) but not when examining differences in the voxel level (i.e. for a given ROI pair) due to the presence of spurious connectivity measures brought about by SBF's spatial leakage. Further work would be useful to confirm this as the genuine basis for the

disparities between the SBF, MCBF and CHAMPAGNE reconstructions. In addition, improved pre-processing techniques need to be developed to allow the successful application of temporal ICA to MCBF and CHAMPAGNE reconstructed data for RSN characterization and comparison with SBF RSN reconstructions.

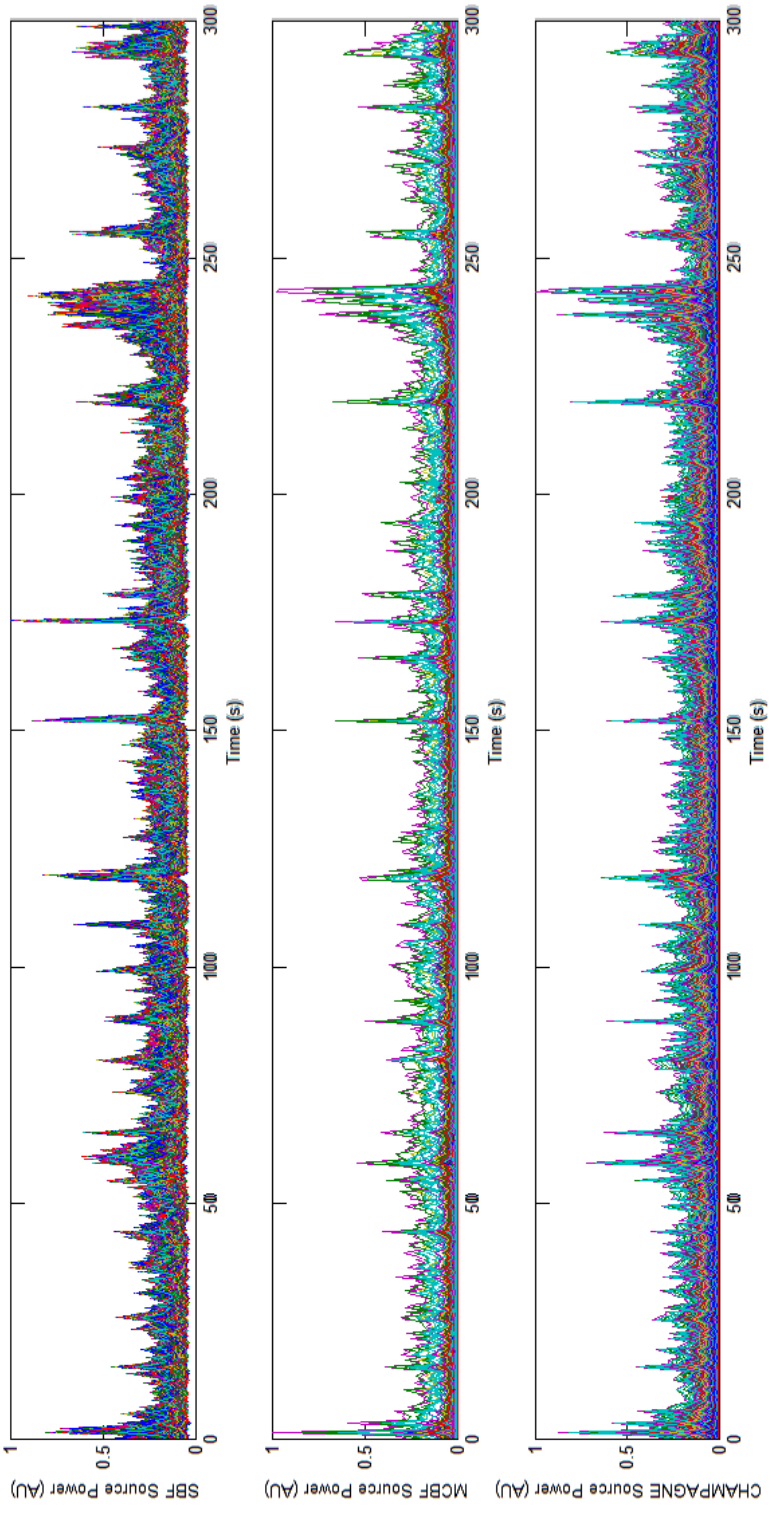

Figure 4.1: Source time-courses for a representative subject reconstructed using SBF (top), MCBF (middle) and CHAMPAGNE (bottom).

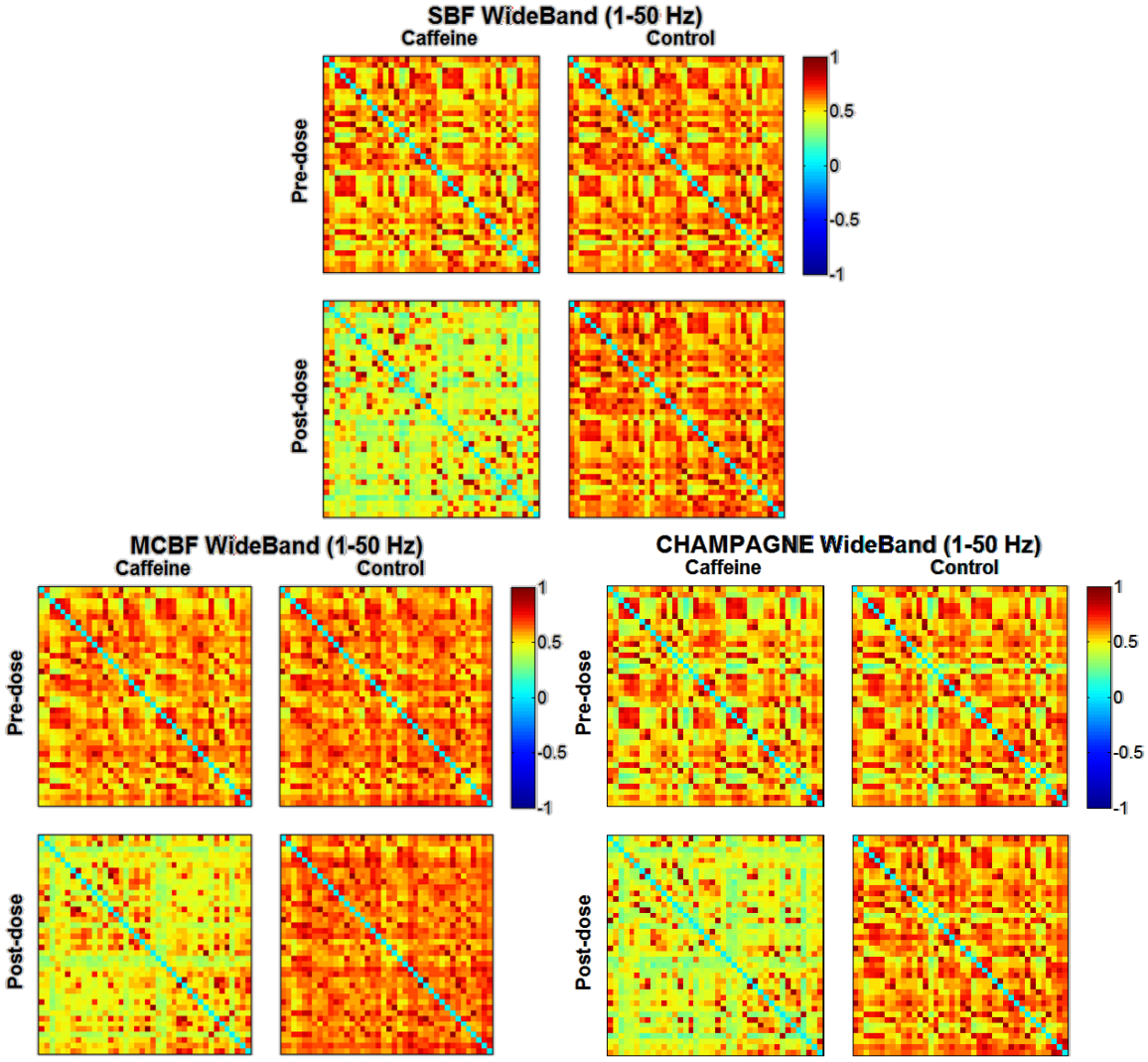

Figure 4.2: Single subject connectivity (ROI-to-ROI Pearson correlations) matrices for MEG wide-band (1-50Hz) data reconstructed with SBF (top), MCBF (bottom left) and CHAMPAGNE (bottom right).
ROI labels (1–20 left hemisphere; 21–40 right hemisphere): anterior cingulate, middle frontal, cuneus, fusiform, inferior parietal, isthmus cingulate, lateral orbitofrontal, medial orbitofrontal, pars opercularis, post central, posterior cingulate, precentral, precuneus, rostral anterior cingulate, rostral middle frontal, superior frontal, superior parietal, superior temporal, supramarginal, insula.

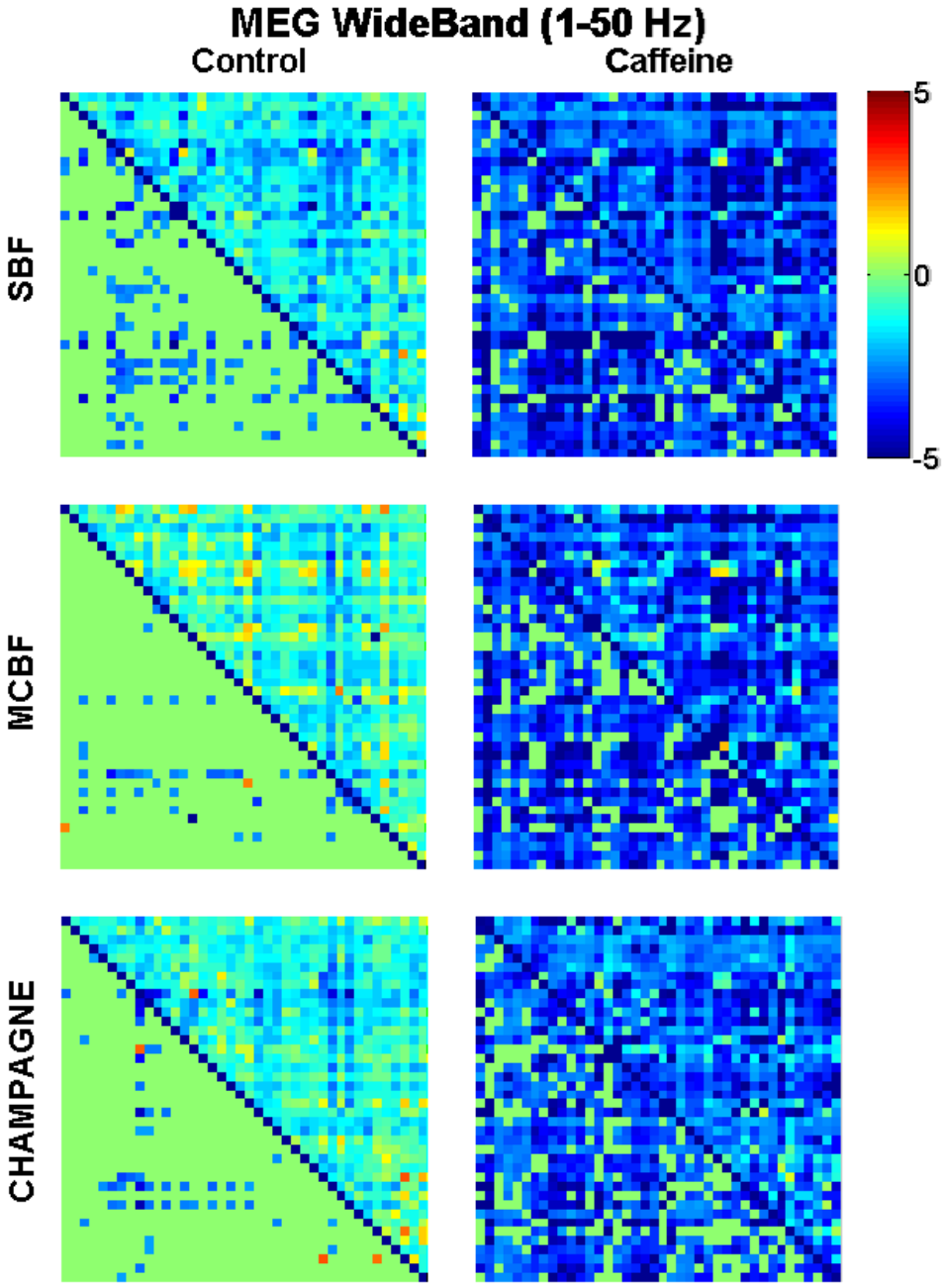

Figure 4.3: Mean connectivity changes across subjects (blue color – decrease, red color – increase) for MEG wide-band (1-50Hz) data reconstructed with SBF (top panels), MCBF (center panels) and CHAMPAGNE (bottom panels).
Upper triangle represents mean change in z-scores and lower triangle shows the respective t-statistics for significant ($p < 0.05$) entries.

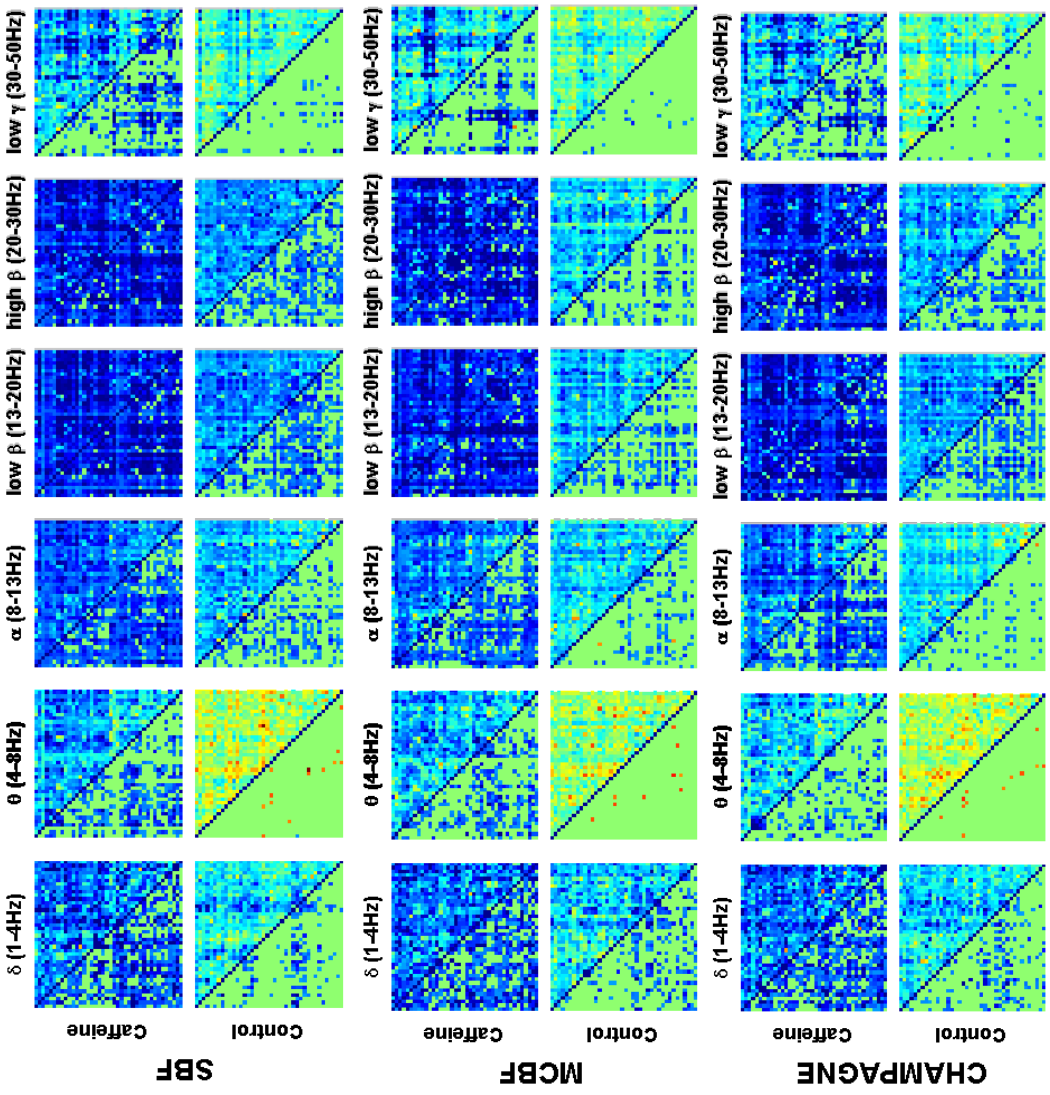

Figure 4.4: Global connectivity changes for SBF, MCBF and CHAMPAGNE reconstructed MEG data (band-limited)

Table 4.1: Repeated measures two-way ANOVA statistics for MEG wide-band data reconstructed with SBF, MCBF and CHAMPAGNE (metric is change in z-score).

		MEG WideBand (1-50Hz) - Eyes Closed					
		SBF		MCBF		CHAMPAGNE	
Factor	**Dof**	F	p	F	p	F	p
Caffeine/contr	(1,9)	12.38	0.0065	12.91	0.0058	11.04	0.0089
ROI pairs	(779,7011	1.23	<1e-5	1.76	<1e-5	1.39	<1e-5
Interaction	(779,7011	0.87	0.99	0.83	1.00	0.85	1.00

Table 4.2: Repeated measures two-way ANOVA statistics for band-limited MEG data reconstructed with the SBF (metric is change in z-score).

	δ		θ		α		Low β		High β		Low γ	
Factor	F	p	F	p	F	p	F	p	F	p	F	p
Caffeine/contr	1.7	0.2	14.5	<0.01	3.7	0.086	9.6	0.012	8.6	0.016	1.3	0.28
ROI pairs	0.8	1.0	1.25	<1e-	2.1	<1e-	1.6	<1e-	1.2	<1e-	1.4	<1e-
Interaction	0.9	0.9	0.80	1.00	0.9	0.89	1.0	0.45	0.9	0.82	0.8	0.99

Table 4.3: Repeated measures two-way ANOVA statistics for band-limited MEG data reconstructed with the MCBF (metric is change in z-score).

	δ		θ		α		Low β		High β		Low γ	
Factor	F	p	F	p	F	p	F	p	F	p	F	p
Caffeine/contr	2.59	0.14	7.25	.025	3.76	0.084	8.79	0.016	13.8	0.048	1.06	0.33
ROI pairs	0.84	1.00	1.01	0.38	1.65	<1e-6	1.75	<1e-6	2.03	<1e-6	1.67	<1e-6
Interaction	0.95	0.83	0.89	0.98	1.04	0.24	1.02	0.37	0.96	0.776	0.77	1.00

Table 4.4: Repeated measures two-way ANOVA statistics for band-limited MEG data reconstructed with the CHAMPAGNE (metric is change in z-score).

	δ		θ		α		Low β		High β		Low γ	
Factor	F	p	F	p	F	p	F	P	F	p	F	p
Caffeine/contro	2.16	0.18	6.5	.031	2.93	0.12	8.81	0.016	7.88	0.02	1.38	0.27
ROI pairs	0.94	0.88	1.0	0.37	2.12	<1e-6	1.96	<1e-6	2.04	<1e-6	1.45	<1e-6
Interaction	1.15	0.004	1.0	0.26	1.25	<1e-6	1.00	0.49	1.15	0.003	0.76	1.00

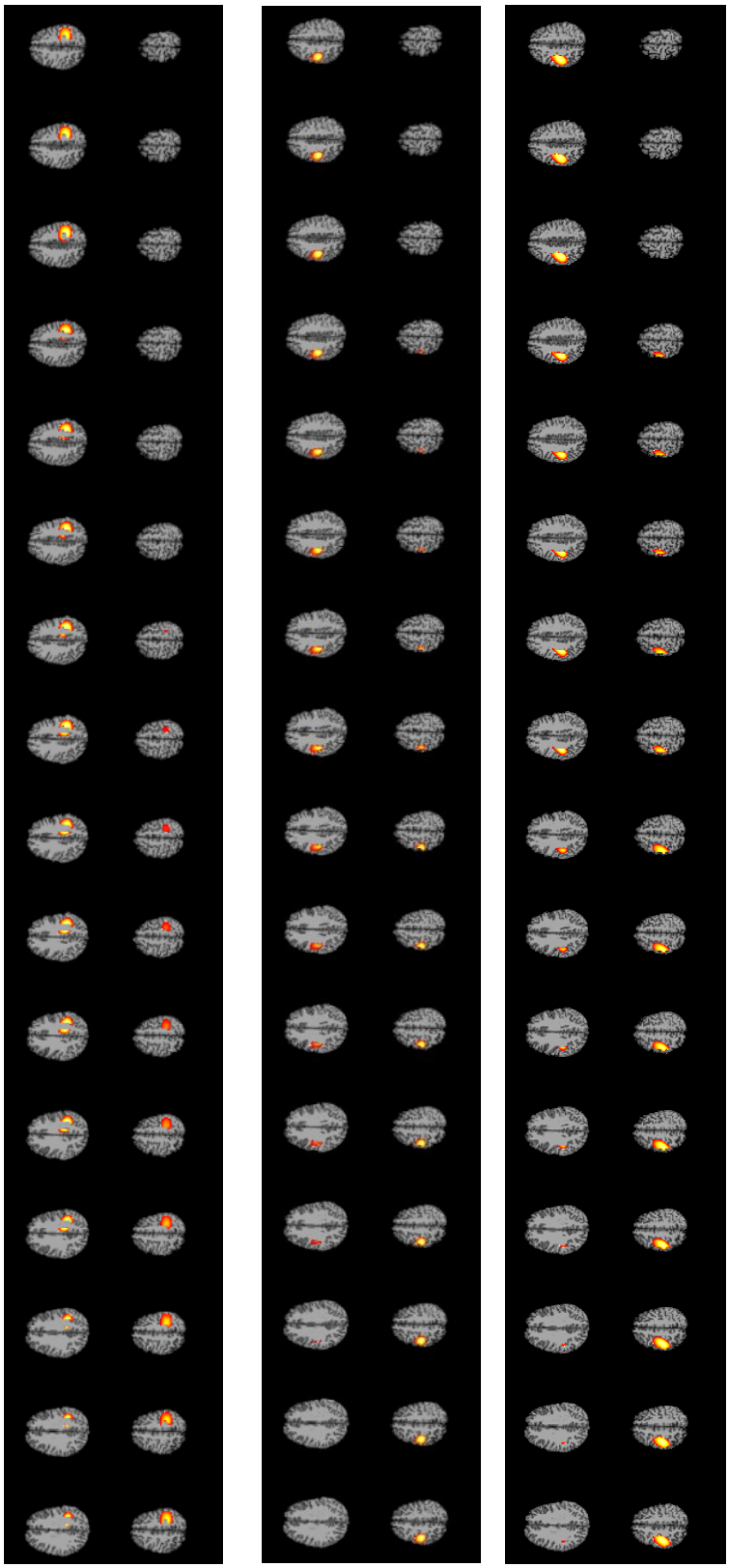

Figure 4.5: Independent component corresponding to motor network from SBF (top), MCBF (middle) and CHAMPAGNE (bottom) reconstructed time-courses (map derived from a single 5-min acquisition for an individual subject).

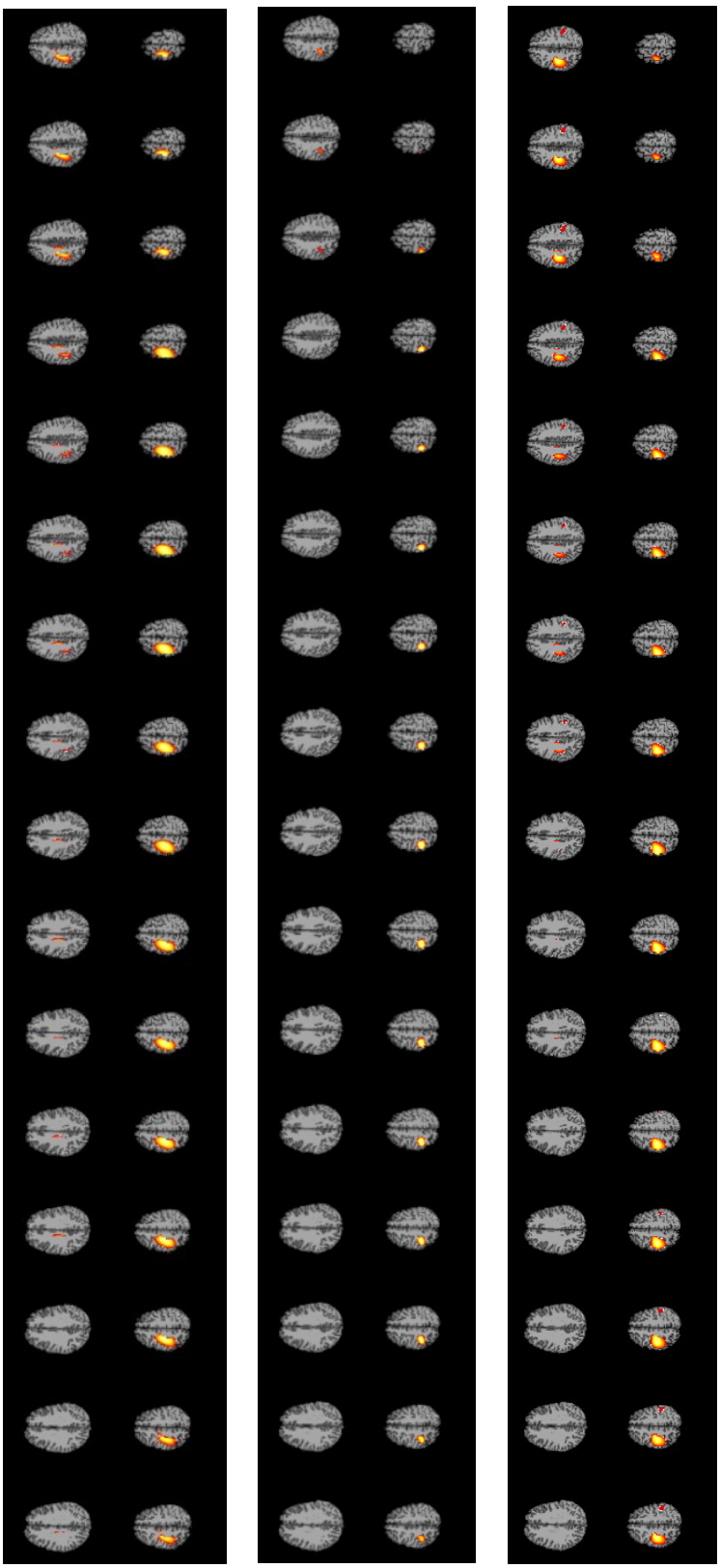

Figure 4.6: Independent component corresponding to motor network from SBF (top), MCBF (middle) and CHAMPAGNE (bottom) reconstructed time-courses (map derived from four concatenated 5-min acquisitions for an individual subject.

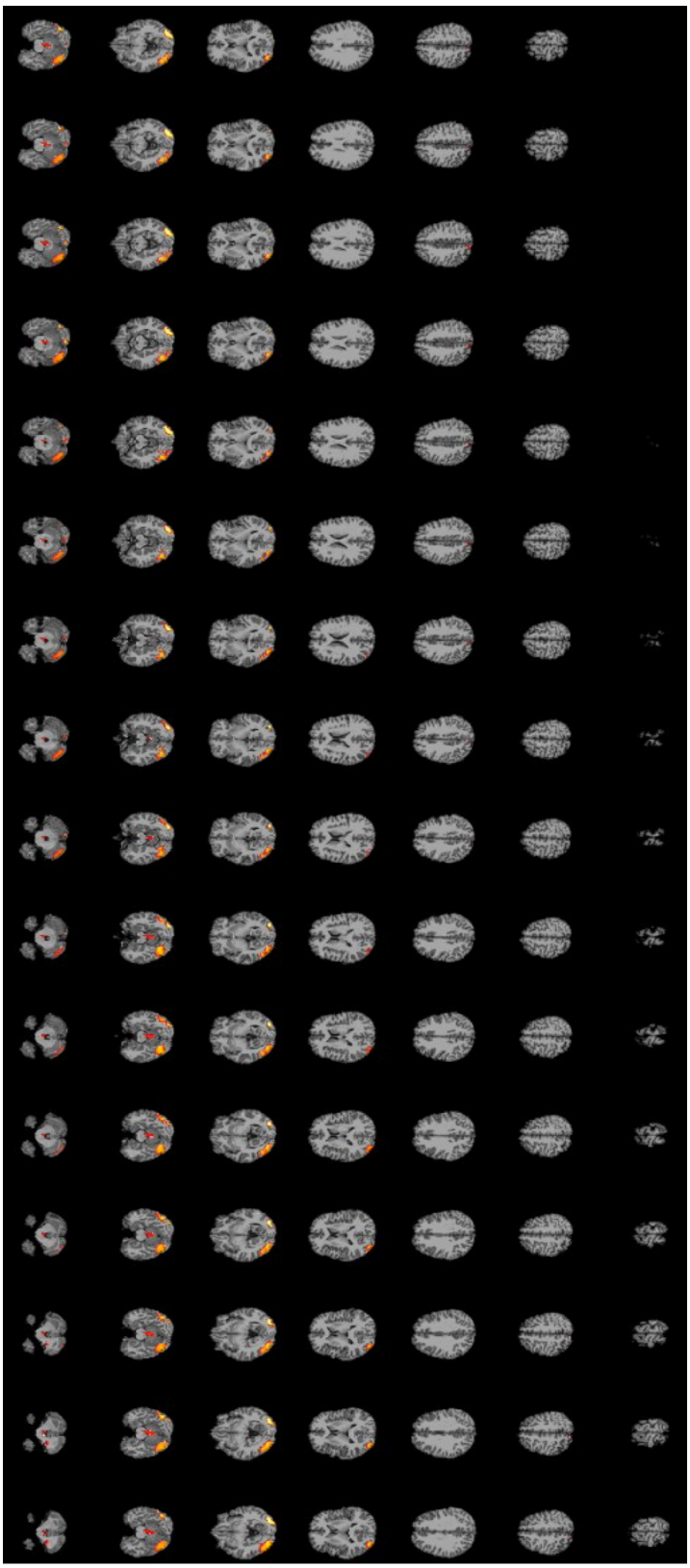

Figure 4.7: Independent component corresponding to visual network from MCBF reconstructed time-courses (map derived from four concatenated 5-min acquisitions for an individual subject.

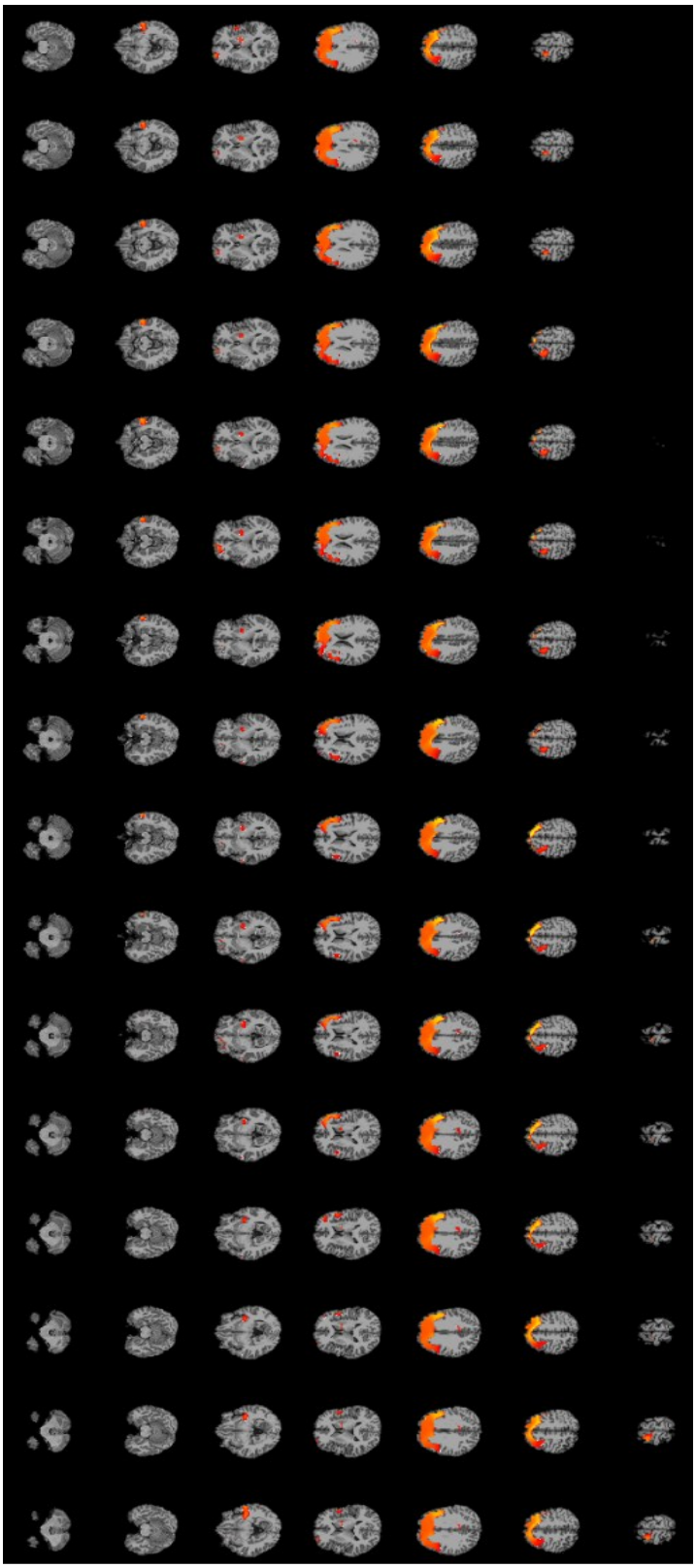

Figure 4.8: Independent component corresponding to executive network from MCBF reconstructed time-courses (map derived from four concatenated 5-min acquisitions for an individual subject.

References

Beckmann, C.F., DeLuca, M., Devlin, J.T., Smith, S.M., 2005. Investigations into resting-state connectivity using independent component analysis. Philos Trans R Soc Lond B Biol Sci 360, 1001-1013.

Behzadi, Y., Restom, K., Liau, J., Liu, T.T., 2007. A component based noise correction method (CompCor) for BOLD and perfusion based fMRI. Neuroimage 37, 90-101.

Brookes, M.J., Hale, J.R., Zumer, J.M., Stevenson, C.M., Francis, S.T., Barnes, G.R., Owen, J.P., Morris, P.G., Nagarajan, S.S., 2011a. Measuring functional connectivity using MEG: methodology and comparison with fcMRI. Neuroimage 56, 1082-1104.

Brookes, M.J., Liddle, E.B., Hale, J.R., Woolrich, M.W., Luckhoo, H., Liddle, P.F., Morris, P.G., 2012a. Task induced modulation of neural oscillations in electrophysiological brain networks. Neuroimage 63, 1918-1930.

Brookes, M.J., Stevenson, C.M., Barnes, G.R., Hillebrand, A., Simpson, M.I., Francis, S.T., Morris, P.G., 2007. Beamformer reconstruction of correlated sources using a modified source model. Neuroimage 34, 1454-1465.

Brookes, M.J., Woolrich, M., Luckhoo, H., Price, D., Hale, J.R., Stephenson, M.C., Barnes, G.R., Smith, S.M., Morris, P.G., 2011b. Investigating the electrophysiological basis of resting state networks using magnetoencephalography. Proc Natl Acad Sci U S A 108, 16783-16788.

Brookes, M.J., Woolrich, M.W., Barnes, G.R., 2012b. Measuring functional connectivity in MEG: a multivariate approach insensitive to linear source leakage. Neuroimage 63, 910-920.

Buxton, R.B., Uludag, K., Dubowitz, D.J., Liu, T.T., 2004. Modeling the hemodynamic response to brain activation. Neuroimage 23 Suppl 1, S220-233.

Dalal, S.S., Sekihara, K., Nagarajan, S.S., 2006. Modified beamformers for coherent source region suppression. IEEE Trans Biomed Eng 53, 1357-1363.

Desikan, R.S., Segonne, F., Fischl, B., Quinn, B.T., Dickerson, B.C., Blacker, D., Buckner, R.L., Dale, A.M., Maguire, R.P., Hyman, B.T., Albert, M.S., Killiany, R.J., 2006. An automated labeling system for subdividing the human cerebral cortex on MRI scans into gyral based regions of interest. Neuroimage 31, 968-980.

Diwakar, M., Huang, M.X., Srinivasan, R., Harrington, D.L., Robb, A., Angeles, A., Muzzatti, L., Pakdaman, R., Song, T., Theilmann, R.J., Lee, R.R., 2011a. Dual-Core Beamformer for obtaining highly correlated neuronal networks in MEG. Neuroimage 54, 253-263.

Diwakar, M., Tal, O., Liu, T.T., Harrington, D.L., Srinivasan, R., Muzzatti, L., Song, T., Theilmann, R.J., Lee, R.R., Huang, M.X., 2011b. Accurate reconstruction of temporal correlation for neuronal sources using the enhanced dual-core MEG beamformer. Neuroimage 56, 1918-1928.

Fredholm, B.B., Battig, K., Holmen, J., Nehlig, A., Zvartau, E.E., 1999. Actions of caffeine in the brain with special reference to factors that contribute to its widespread use. Pharmacol Rev 51, 83-133.

Hall, E.L., Woolrich, M.W., Thomaz, C.E., Morris, P.G., Brookes, M.J., 2013. Using variance information in magnetoencephalography measures of functional connectivity. Neuroimage 67, 203-212.

Hamalainen, M., Hari, R., Ilmoniemi, R.J., Knuutila, J., Lounasmaa, O.V., 1993. Magnetoencephalography - Theory, Instrumentation, and Applications to Noninvasive Studies of the Working Human Brain. Reviews of Modern Physics 65, 413-497.

Hillebrand, A., Barnes, G.R., Bosboom, J.L., Berendse, H.W., Stam, C.J., 2012. Frequency-dependent functional connectivity within resting-state networks: an atlas-based MEG beamformer solution. Neuroimage 59, 3909-3921.

Hipp, J.F., Hawellek, D.J., Corbetta, M., Siegel, M., Engel, A.K., 2012. Large-scale cortical correlation structure of spontaneous oscillatory activity. Nat Neurosci 15, 884-890.

Huang, M.X., Song, T., Hagler, D.J., Jr., Podgorny, I., Jousmaki, V., Cui, L., Gaa, K., Harrington, D.L., Dale, A.M., Lee, R.R., Elman, J., Halgren, E., 2007. A novel integrated MEG and EEG analysis method for dipolar sources. Neuroimage 37, 731-748.

Hui, H.B., Leahy, R.M., 2006. Linearly constrained MEG beamformers for MVAR modeling of cortical interactions. 3rd IEEE International Symposium on Biomedical Imaging: Nano to Macro, pp. 237–240.

Hui, H.B., Pantazis, D., Bressler, S.L., Leahy, R.M., 2010. Identifying true cortical interactions in MEG using the nulling beamformer. Neuroimage 49, 3161-3174.

Hyvarinen, A., 1999. Fast and robust fixed-point algorithms for independent component analysis. IEEE Trans Neural Netw 10, 626-634.

Jones, H.E., Herning, R.I., Cadet, J.L., Griffiths, R.R., 2000. Caffeine withdrawal increases cerebral blood flow velocity and alters quantitative electroencephalography (EEG) activity. Psychopharmacology (Berl) 147, 371-377.

Keppel, G., Wickens, T.D., 2004. Design and Analysis: A Researcher's Handbook. Pearson Prentice Hall, Upper Saddle River.

Kumihashi, I., Sekihara, K., 2010. Array-gain constraint minimum-norm spatial filter with recursively updated gram matrix for biomagnetic source imaging. IEEE Trans Biomed Eng 57, 1358-1365.

Luckhoo, H., Hale, J.R., Stokes, M.G., Nobre, A.C., Morris, P.G., Brookes, M.J., Woolrich, M.W., 2012. Inferring task-related networks using independent component analysis in magnetoencephalography. Neuroimage 62, 530-541.

Mantini, D., Della Penna, S., Marzetti, L., de Pasquale, F., Pizzella, V., Corbetta, M., Romani, G.L., 2011. A signal-processing pipeline for magnetoencephalography resting-state networks. Brain Connect 1, 49-59.

Moiseev, A., Gaspar, J.M., Schneider, J.A., Herdman, A.T., 2011. Application of multi-source minimum variance beamformers for reconstruction of correlated neural activity. Neuroimage 58, 481-496.

Moiseev, A., Herdman, A.T., 2013. Multi-core beamformers: derivation, limitations and improvements. Neuroimage 71, 135-146.

Mosher, J.C., Leahy, R.M., Lewis, P.S., 1999. EEG and MEG: forward solutions for inverse methods. IEEE Trans Biomed Eng 46, 245-259.

Quraan, M.A., Cheyne, D., 2010. Reconstruction of correlated brain activity with adaptive spatial filters in MEG. Neuroimage 49, 2387-2400.

Reeves, R.R., Struve, F.A., Patrick, G., 2002. Topographic quantitative EEG response to acute caffeine withdrawal: a comprehensive analysis of multiple quantitative variables. Clin Electroencephalogr 33, 178-188.

Robinson, S., Vrba, J., 1998. Functional neuroimaging by synthetic aperture magnetometry. Tohoku Univ. Press, Sendai.

Schnitzler, A., Gross, J., 2005. Functional connectivity analysis in magnetoencephalography. Int Rev Neurobiol 68, 173-195.

Sekihara, K., Nagarajan, S.S., Poeppel, D., Marantz, A., 2002. Performance of an MEG adaptive-beamformer technique in the presence of correlated neural activities: effects on signal intensity and time-course estimates. IEEE Trans Biomed Eng 49, 1534-1546.

Sekihara, K., Nagarajan, S.S., 2008. Adaptive Spatial Filters for Electormagnetic Brain Imaging. SpringerLink, Berlin.

Singer, W., 1999. Neuronal synchrony: a versatile code for the definition of relations? Neuron 24, 49-65, 111-125.

Smith, S.M., Fox, P.T., Miller, K.L., Glahn, D.C., Fox, P.M., Mackay, C.E., Filippini, N., Watkins, K.E., Toro, R., Laird, A.R., Beckmann, C.F., 2009. Correspondence of the

brain's functional architecture during activation and rest. Proc Natl Acad Sci U S A 106, 13040-13045.

Song, T., Cui, L., Gaa, K., Feffer, L., Taulu, S., Lee, R.R., Huang, M., 2009. Signal space separation algorithm and its application on suppressing artifacts caused by vagus nerve stimulation for magnetoencephalography recordings. J Clin Neurophysiol 26, 392-400.

Song, T., Gaa, K., Cui, L., Feffer, L., Lee, R.R., Huang, M., 2008. Evaluation of signal space separation via simulation. Med Biol Eng Comput 46, 923-932.

Tal, O., Diwakar, M., Wong, C.W., Olafsson, V., Lee, R., Huang, M.X., Liu, T.T., 2013. Caffeine-Induced Global Reductions in Resting-State BOLD Connectivity Reflect Widespread Decreases in MEG Connectivity. Front Hum Neurosci 7, 63.

Taulu, S., Kajola, M., Simola, J., 2004. Suppression of interference and artifacts by the Signal Space Separation Method. Brain Topogr 16, 269-275.

Taulu, S., Simola, J., 2006. Spatiotemporal signal space separation method for rejecting nearby interference in MEG measurements. Phys Med Biol 51, 1759-1768.

Van Drongelen, W., Yuchtman, M., Van Veen, B.D., Van Huffelen, A.C., 1996. A spatial filtering technique to detect and localize multiple sources in the brain. Brain Topogr 9, 39-49.

Van Veen, B.D., van Drongelen, W., Yuchtman, M., Suzuki, A., 1997. Localization of brain electrical activity via linearly constrained minimum variance spatial filtering. IEEE Trans Biomed Eng 44, 867-880.

Wipf, D.P., Owen, J.P., Attias, H.T., Sekihara, K., Nagarajan, S.S., 2010. Robust Bayesian estimation of the location, orientation, and time course of multiple correlated neural sources using MEG. Neuroimage 49, 641-655.

Wong, C.W., Olafsson, V., Tal, O., Liu, T.T., 2012. Anti-correlated networks, global signal regression, and the effects of caffeine in resting-state functional MRI. Neuroimage 63, 356-364.

CHAPTER 5

Scope

As the task of MEG and EEG signal post-processing is known to be quite extensive, being both time-consuming and computationally complex, an appropriate toolbox to assist in the matter was designed while keeping simplicity and ease in mind. The toolbox, dubbed EEGMEG (for the type of data it handles), required minimal interaction from the user while providing it with a wide array of processing capabilities. The EEGMEG toolbox utilizes MATLAB for its backbone (main software driving the program), while being supplemented by other software such as the Neuroelectromagnetic Forward Head Modeling Toolbox (NFT) (Acar and Makeig, 2010), fMRIB Software Library (FSL)(Smith et al., 2004), Minimum-Norm Estimates (MNE) package (Gramfort et al., 2014), FreeSurfer (Fischl, 2012) and AFNI (Cox, 1996) to complete specific parts of the analysis processes (full functionality requires installation of all programs mentioned).

General Functionality

Processing capabilities

EEGMEG provides an analysis pathway for the two dominant imaging modalities currently available for non-invasive neuroelectrical signal detection: EEG and MEG. For MEG, both sensor-space (outside the brain) and source-space (inside the brain) analysis pipelines are provided, while only the latter is currently available for EEG. Furthermore, in the case of MEG sensor-space analysis, an advanced form which uses anatomical MRI data to improve accuracy is also available to the user. To prepare the MR anatomical data

necessary for the aforementioned case or for any MEG/EEG source-space analysis, EEGMEG contains a pre-preprocessing pathway common to the two modalities, where such data as well as other mandatory items (e.g. Boundary element method (BEM) meshes, dipole grids, gain matrices, etc.) are generated. Pre-preprocessed sensor as well as reconstructed source time-courses can exploit the multiple available atlases (e.g. Harvard-Oxford from FSL, Desikan-Killiany from FreeSurfer) to estimate both ROI-based power and connectivity measures. EEG and MEG reconstructed source time-courses can employ either seed-based or ICA approaches to conduct functional analyses producing both surface and volume maps as well as movies of power and connectivity dynamics (FSL and FreeSurfer compatible formats). All supporting files and results created during the toolbox's processing are immediately stored in a simple, systematic manner allowing easy retrieval of the processed data for any post-analysis examination desired by the user.

Architectural Structure

All of EEGMEG's core functions are written and executed within the MATLAB software environment. To maximize simplicity and ease, EEGMEG was designed such that the average user's knowledge requirements were limited to the minimum of viewing and editing a *single* m-file, named eegmegSetup.m. This file contains a wide array of pertinent flags and parameters for the user to set and is used to distinguish and control the analysis pathway (described in detail below). All analysis pertinent information (e.g. flags, parameters, defining variables, file locations) is stored in single structure (titled *em*), which is used as the sole input and output variable for the majority of EEGMEG's functions. This ensures that each function serves as an independent building block,

simplifying the integration of newly developed functions into the existing processing pathway (as well as their removal).

File Storage

EEGMEG toolbox operation entails mainly three distinct groups of files (see Figure 5.1 for examples) which must be accurately stored, updated and retrieved: neurophysiological recordings (raw as well as minimally pre-processed using MaxFilter and/or ICA to remove non-neuronal artifacts), subject-specific anatomical files (e.g. DICOM files, MEG-MRI registration file, BEM meshes, dipole grids, etc.) and lastly any post-processing results (e.g. reconstructed source time-courses, connectivity/amplitude maps and movies, spatial/temporal ICA maps, etc.). All EEGMEG analyses can be completed locally, resulting in all three file groups remaining within the containing folder (i.e. the folder from which *eegmegSetup.m* was launched). However, the option of the EEGMEG database also exists for those who are collecting repeated measures on subjects or conducting multiple analyses on the same recordings and are interested in increasing storage efficiency. Specifically, the database is comprised from files from the first two groups (neuro-recordings and subject-specific anatomical files) which need to be manipulated or generated only once for any given subject, helping eliminate any unnecessary repetitiveness. All results (3rd group) remain in the same location as described above. All supporting files, regardless of category, are stored (within their own respective location) using a unique folder directory based on the project title, subject id and date of data acquisition, ensuring any necessary data review can be completed with ease.

Main Setup File

Eegmegsetup.m serves as the launch pad for the EEGMEG toolbox and is the sole m-file the average user should be concerned with (see Figure 5.2 for sample excerpts). To start, the user simply defines the analysis by labeling the necessary identifiers which make it unique: project name, subject id and data acquisition date. This information points EEGMEG to a distinct directory pathway, which can be used to follow all file groups related to that specific analysis (i.e. for a given day, subject and projects). EEGMEG can then determine if this is a repeating analysis on an already existing dataset or a brand new analysis (if the pathway does not exist), where in the latter case the user must also specify the current location of the acquired raw data (neurophysiological and anatomical). Lastly, the user must specify the type of analysis to be conducted (e.g. sensor/source EEG/MEG) and then set various corresponding flags and parameters for his desired analysis. For example, when conducting source analysis, a user must select what type of dipole grid he would desire to employ (e.g. rectangular or cortical). Flags/parameters which can be set regardless of analysis type also exist, such as temporal downsampling or filtering or the recorded neurophysiological data. Once finished, the user can simply launch EGGMEG by executing the amended setup file.

Data Processing

Pre-Launch EEGMEG

Before any data pre-processing or analysis begins, EEGMEG runs through a series of automated initialization steps that are necessary for proper operation of the toolbox. For example, EEGMEG checks to see if the unique project/subject/date combo already exists (e.g. corresponding 'em' structure, analysis directories, etc…). If non-

existent, initialization of a new set of essential files and folders will take place and all new raw data (MRI or neurophysiological) will be uploaded if requested.

Anatomical MRI and EEG/MEG Pre-Processing

If any anatomical MRI data is present, and the user desires to or the analysis necessitates anatomical information (mandatory step for MEG/EEG source but not sensor analysis), the following pre-processing steps will take place (see Figure 5.3 for sample figures). First, EEGMEG will utilize FreeSurfer (the process is completely automated, no user input necessary) to reconstruct a volumetric MRI image set along with the white/gray matter segmented volumes and cortical parcellations of the given subject. Next, since MEG sensors are not fixed to the head (i.e. relative positioning unknown), the collected fiducials/sensors coordinates must be used to align and co-register the sensor (MEG) and anatomical (MRI) spaces. This step is completed with the help of MRILAB (Neuromag^{TM}) software and is one of the few steps which requires significant user input (as the alignment process could not be computer automated). SEGLAB (another Neuromag^{TM} software program) then uses the skull-stripped MR volume to create the BEM Mesh (representing the inner skull surface) which will be used in the forward model computation and construction. Although MEG data can be processed using a single surface (as the signal is insensitive to the different layers of the brain), EEG requires at least three surfaces to be modeled (inner skull surface, outer skull surface and scalp). Thus, for any EEG analysis (or if a user desires to do a 3-shell MEG analysis), the NFT toolbox is then employed to construct any necessary meshes. All anatomical MR files are automatically prepared and converted to the necessary format for NFT. For both SEGLAB and the NFT procedures, minimal user input (following printed instructions) is

necessary to obtain all desired surfaces. In addition, the subject's dipole grid is created (fully automated) based on the user's selection from the three available choices: a generic rectangular 3D grid (5mm spacing), a FreeSurfer cortical (gray/white matter boundary) grid and a NFT cortical grid. Combined together (meshes and grid), the EEG and/or MEG forward model is computed using the forward models introduced in (Huang et al., 1999; Mosher et al., 1999). For MEG, a spherical head model is offered in addition to the BEM option. For EEG data, the NFT toolbox's forward model is also available as an option for those using the FS/NFT grids. Lastly, a variety of atlases to be used later in whole-brain ROI analyses are morphed into the subject space (including FSL's Harvard-Oxford, FreeSurfer's Desikan-Killiany and more). Please note that all these steps take place only once (i.e. EEGMEG does not repeat any task twice; all pertinent information is stored for future analyses in the applicable directory).

Neurophysiological Data Pre-processing

This stage begins with a user prompt to select the files of interest for the analysis. If selected to do, MEG data will be cleaned via Maxfilter™ (Taulu et al., 2004; Taulu and Simola, 2006), a temporal signal space separation technique (Figure 5.4A) which helps to remove any unwanted signals originating outside the brain (e.g. dental work, sensor array interference, etc.). Also available is temporal ICA by means of the fastICA algorithm (Hyvarinen, 1999), commonly used to remove any artifact-related independent components (e.g. residual cardiac activity, eye blinks and movements). A user-friendly GUI (Figure 5.4B) containing the computed IC time-courses and corresponding spatial maps, along with automated prompts, provides the user with the necessary environment to visually remove false signals with ease. Next, based on user defined parameters in

eegmegSetup.m, all data files possibly undergo trimming, filtering and downsampling. Trimming can either be completed automatically (user pre-defines desired length) or manually using a pop-up GUI where the user chooses the endpoints. Files can either be low-pass filtered, filtered within a frequency band of choice or left unfiltered. If employing band-pass filtering, multiple bands can be processed at once (e.g. α band, β band, etc.). Downsampling can also be automated (based on filtering choices), manual selected by the user or not applied at all.

Sensor Analysis

Two main methods exist in the MEG sensor analysis path: a simple, quick approach which requires no anatomical MR data and a more intricate approach which accounts for the user's head positioning to improve the results. In the former approach shown in Figure 5.5A, the sensor field is divided into 14 ROIs based on general brain regions (e.g. left/right parietal, L/R temporal, etc.), and the different sensor groups are then used to characterize the global temporal dynamics (e.g. connectivity, power) of the neurophysiological signal. In the latter showing in Figure 5.5B, the gain matrix obtained in the forward model estimation (during anatomical/MEG pre-processing) is used to "guide" the grouping selection, by observing which sensors most reflect the activity at the various cortical ROIs (obtained from the subject's maps) and selecting and grouping those to be used in the sensor ROI-to-ROI dynamics analyses (Figure 5.5D). For example, the sensors which exhibited the highest gain value across all left motor cortex dipoles were then used to form the left motor sensor ROI group.

Source Analysis Reconstruction Techniques

EEGMEG provides the user with the choice between four source reconstruction techniques currently available in neuroelectromagnetic signal analysis research: the minimum-variance vector beamformer (Robinson, 1998; Sekihara, 2008; Van Drongelen, 1996; Van Veen et al., 1997), the Vector-based Spatial-temporal minimum L1-norm solution – VESTAL (Huang et al., 2006), the empirical Bayesian-based method for source localization known as Champagne (Owen et al., 2012; Wipf et al., 2010) and the multi-core beamformer (MCBF) proposed in Chapter 4. All may be executed in the same analysis run if desired. To improve reconstruction success, regularization of the sensor data prior to reconstruction can be employed (regardless of the technique chosen). The user can either manually choose (via a pop-up plot of the eigenvalue spectrum) the desired regularization level for each file, use a predetermined percent cut-off value or use the built-in, automated regularization, an exclusive feature of EEGMEG. The latter utilizes a modified "broken-stick" model (Behzadi et al., 2007) along with precomputed statistical distributions of eigenvalues from random noise (normally distributed) to help identify the meaningful data components that should be kept.

Data Analysis

For the MEG sensor analysis, time-frequency analysis using either Morlet wavelets (Figure 5.5C) or the Hilbert transform can be applied to the data to obtain amplitude and power waveforms. Subsequently, estimates of amplitude and power in the various ROIs and/or functional connectivity (Pearson correlation coefficient) between the ROI pairs can be made for each band of interest. Similarly, MEG and EEG source amplitude and power waveforms can be attained. Analysis outputs include but are not limited to: whole-brain ROI amplitude matrices, whole-brain ROI-to-ROI connectivity

matrices, RMS amplitude and Z-power 3D brain maps, ROI seed-based functional connectivity maps, 3D movies of reconstructed time-courses, spatial/temporal ICA analysis for resting-state networks detections, etc. (Figure 5.6). Three-dimensional maps can either be produced in FreeSurfer format (surface based) or FSL format (volume based), but three-dimensional movies currently only come in the FreeSurfer format. The ROIs used for power/connectivity analysis are obtained either from the Harvard-Oxford atlas or the Desikan-Killiany cortical parcellations. Lastly, for any of the seed-based analysis outputs, the user may select the type of seed to from three existing options: a spherical seed around a manually designated coordinate, an automatically chosen central spherical seed (using a minimum distance scheme) or the entire ROI as the seed (source time-courses are averaged to provide seed time-courses).

Independent EEGMEG tools

EEGMEG also includes some tools that are independent of the analysis pathways mentioned thus far. Most popular is FifView (Figure 5.7), designed for quick and easy access to review any EEG or MEG fif files (Neuromag format). The GUI allows the user to evaluate sensor time-courses both on an individual channel basis and in groups (MEG gradiometers, MEG magnetometers, EEG sensors). For the latter, statistics such as standard deviation of the signal from each of the measurement channels or the signal's overall frequency spectrum can be displayed (can be computed for a certain window of interest or the entire time-course). In addition, sensor time-courses can be manipulated via filtering (low-pass and band-pass) and trimming (completed with user's manual selection of regions to be removed). If desired, all changes can be saved as a new file (same format). Figures of the MEG and EEG sensors' spatial organization are provided

for user convenience, highlighting the sensors whose waveforms are being currently displayed.

An additional GUI tool (Figure 5.7) offered provides the user with the proper environment for inspection of three-dimensional spatial IC maps (computed from reconstructed source time-courses during data analysis). Once the user points the GUI to the folder containing the files of interest, EEGMEG automatically determines the subject being inspected and brings his anatomical MR data into view (in a montage format given the large number of slices), after which it loads the first IC map and overlays it on the anatomical. The user can then easily move back and forth between the available IC maps, as the GUI automatically refreshes the display to overlay the new IC. If multiple frequency bands have been analyzed, the user can navigate between them as well (i.e. each band generates its own set of IC maps). In order to optimize viewing, the user can manually specify the overlay's color scale minimum and maximum threshold values. The GUI can also be requested to do so automatically (when each new IC is overlayed), further increasing ease and speed of inspection.

Another significant tool is the EEGMEG simulator (heavily used in Chapters 2 and 3), which is capable of creating a simulated sensor waveform dataset based on user specified inputs such as: timing parameters (pre-stimulus/stimulus durations, sampling rate), dipole information (number of dipoles and their corresponding amplitude, frequency, orientation, phase shift, modulating frequency and location) and waveform type (basic sinusoidal, complex chirps or modulated sinusoidal waveforms). Simulations can be designed across a range of SNR (signal-to-noise ratios) or dipole locations (resulting in a simulated dataset for each scenario of interest). The anatomical data of a

sample subject pre-loaded into the EEGMEG toolbox is used for the forward model analysis (i.e. sensor time-course computation). Due to the simulator's high degree of flexibility, it can serve as the ideal tool for testing the true performance of a source-reconstruction technique.

A fourth noteworthy tool is the EEGMEG's eigenvalue distribution creator which employs randomly distributed noise waveforms to help identify meaningful eigenvalues in the measured data. Such distributions are typically used in the regularization step in source-reconstruction analysis to determine the "noise" mode cut-off. The user can design the random distributions based on the actual data to be analyzed by defining the number of data points, sampling rate, number of modes expected in the data (can be a range), any filtering (e.g. band-pass) that took place and the desired number of Monte Carlo iterations. The distribution sets are then scaled to a norm of 1 (re-scaled to actual data before any comparison) and stored for future use by any of EEGMEG's source reconstruction techniques.

Future Work

Of highest importance is to complete the functionality of the EEG sensor analysis pathway (previously done with the EEGLAB toolbox), thus allowing EEGMEG to provide a comprehensive EEG/MEG capability within one integrated environment. Other tasks would include the integration of functional MRI analysis (currently done with fmritools toolbox developed at the UCSD center for FMRI) into EEGMEG, as the collection of fMRI data in conjunction with EEG data has become a common occurrence these days. Lastly, an overhaul of all documentation to improve user support and

experience would be advantageous for the success of EEGMEG as a universal tool for neuroelectromagnetic analyses.

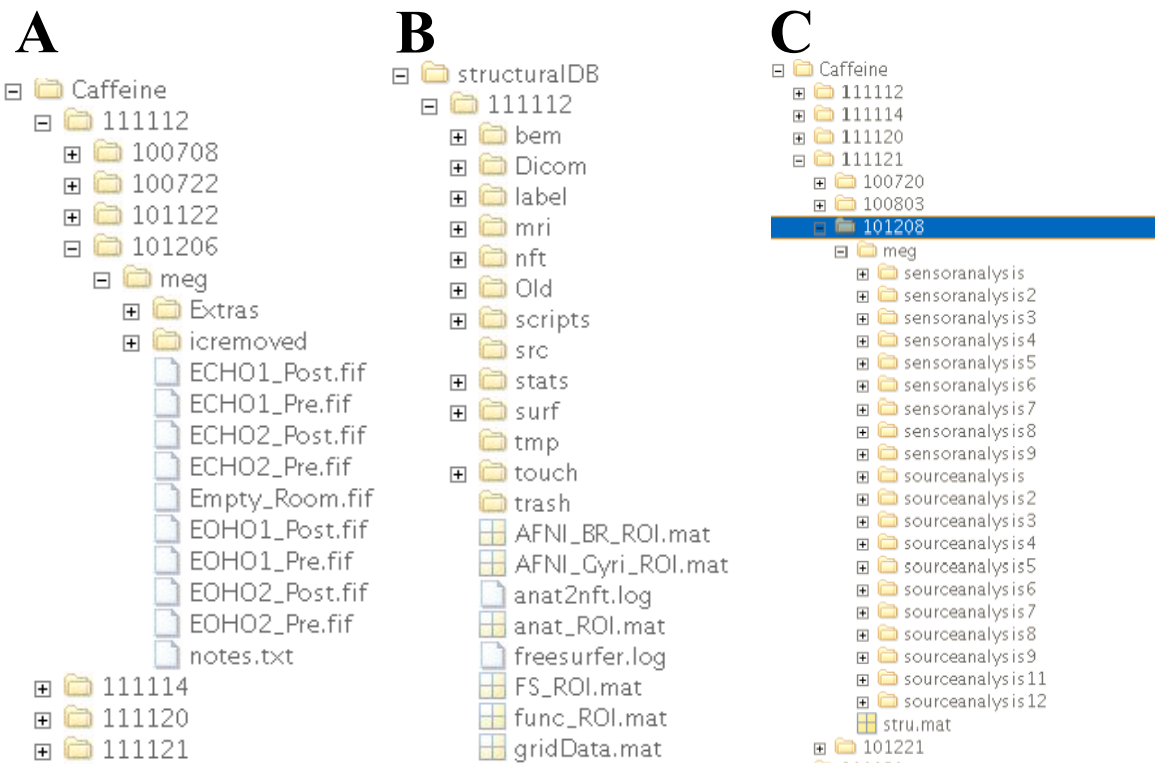

Figure 5.1: Example screenshots of MATLAB depicting EEGMEG's directory structure for the three distinct file groups: neurophysiological recordings (A), subject-specific anatomical files (B) and post-processing results (C).

```
%% Project Definition
em.study.name       = 'Pilot'; % MAKE SURE IT IS ONE WORD
em.study.operator   = 'John Smith';
em.study.scanner    = '3TWest';
em.study.date       = '010101'; %(yy/mm/dd)
em.study.subjectID  = '123456';

% LOCATION OF RAW DATA
% Only used when previous structure does not exist, i.e. first/random (e.g. local) analysis such that the raw files are not located on serve
% If on server then default location is /mnt/raid15/raweegmeg/ (for repeated with new structures)
% IMPORTANT: If first (not random) analysis, i.e. eegmegUpload will be utilized,
% make sure inside folder of raw data entered below, a secondary folder exists
% where the raw files are actually located based on modality, e.g. meg, eeg or fmri,
% othewise Upload will fail.
em.dir.data.home    = [pwd '/'];
%% Initialize/Load structure
% Verify wheter subject/date folder already exists (i.e. secondary
% analysis), and load structure from previous run
if (exist([pwd,'/',em.study.name,'/',em.study.subjectID,'/',em.study.date,'/stru.mat'],'file')==2)
    load ([em.study.name,'/',em.study.subjectID,'/',em.study.date,'/stru.mat'])
else % Initialize new structure if first analysis being done
    new = input('\nCurrent Project does not exist. Would you like to set up a new folder set? 1-Y, 0-N --> ');
    if (new)
        em                  = initEegmeg(em);
    else
        error('Dataset Does Not Exist');
    end
end
%% Analysis Execution
em.flags.megsen.do          = 0; %do MEG sensor analysis
em.flags.megsrc.do          = 1; %do MEG source analysis
em.flags.eegsen.do          = 0; %do EEG sensor analysis
em.flags.eegsrc.do          = 0; %do EEG source analysis

if (~em.flags.megsen.do && ~em.flags.megsrc.do && ...
    ~em.flags.eegsen.do && ~em.flags.eegsrc.do)
    error('\nERROR: No analysis type was selected to execute!!\n');
end  % indicate whether user did not select any analysis to process
%% Directory Creation/Initialization
% directory creation initializing function which runs through all
% defined fields under dir to confirm those folders exist.

    em                  = initEMdir(em);
%% RAW File Upload
% If user desires, raw file upload to server folder can be done through the eegmegSetup
% IMPORTANT: If trying to use previously uploaded files then set em.dir.data.home (line 23) to folder location on database and set flag belo
em.flags.upload             = 0; % do file upload
em.flags.eegmegCombined     = 1; % If using FIF file for EEG sets (already in the MEG files) this should be set to 1. For EEGLAB files flag

if (em.flags.upload)
    em                  = eegmegUpload(em);
end
%% Analysis Specific Flags
%%% General Flags
em.flags.duplicate = 0;         % This will assumes that your analysis parameters are duplicated regardless of type (MEG, EEG, sensor, sourc
% USE WITH CAUTION. THIS WILL ASSUME YOU KNOW WHAT YOU ARE DOING. OTHERWISE IF SET TO 1 W/ OUT PROPER PARAMETER SETUP, ERRORS WILL RESULT!!!

%%% MEG pre-processing
em.flags.megpre.doMF          = 1; % whether or not to execute MaxFilter on raw data
em.flags.megpre.doIC          = 1; % whether or not to execute FAST-ICA on raw data
em.flags.megpre.IClp             = 0; % whether or not to Lowpass filter data before IC (set em.para.meg.IClpf for filtering freq.)

%%% General MEG flags
em.flags.meg.evoked = 0;         % Evoked data
em.flags.meg.spon = 1;           % Spontaneous data
em.flags.meg.grid = 2;           % 1 - rectangular grid, 2 - FS cortical grid
em.flags.meg.trunc = 1;          % Truncate data (0 for no trunction, 1 for automated truncation, 2 for visual truncation)
em.flags.meg.truncForce = 0;     % Redo manual truncation (otherwise uses saved truncation)
em.flags.meg.ds = 0;             % Downsample data (0 for no downsampling, 1 for automated downsampling based on filtering frequency, 2 for
em.flags.meg.useSph = 0;         % Use spherical forward model (this or useBEM must be selected)
em.flags.meg.useBEM = 1;         % Use BEM forward model (this or useSph must be selected) - NEW OPTION WILL INCLUDE 2 (BEM WITH THREE SHELL
em.flags.meg.shellType = 1;      % 1 -  single shell (using SEGLAB) or 2 - three shell (using NFT) model for BEMs
...
%% Analysis Pre-Processing
if (em.flags.megsen.do || em.flags.megsrc.do || em.flags.eegsrc.do || em.flags.eegsen.do)
    em = doEegmegpre(em); % EEG/MEG Pre-processing
end
%% Analysis Processing
em  = doMegsen(em);  % MEG sensor analysis
em  = doMegsrc(em); % MEG source analysis
em  = doEegsen(em); % EEG sensor analysis
em  = doEegsrc(em); % EEG source analysis
%% Save Structure/Update Counters
% Run through each do flag and accordingly update every co flag (updates at end only to ensure counters are not updated unless processing is
% complete) Save structure in /subject/data/stru/
if (em.flags.megsen.do && em.flags.megsen.suc)
    em.flags.megsen.co=em.flags.megsen.co+1;
    em.flags.megsen.suc=0; % reset success indicator
end
...
```

Figure 5.2: Screenshots of sample excerpts from *Eegmegsetup.m*, the main definition file for the EEGMEG toolbox, used to vary the data analysis as desired via flags and parameters.

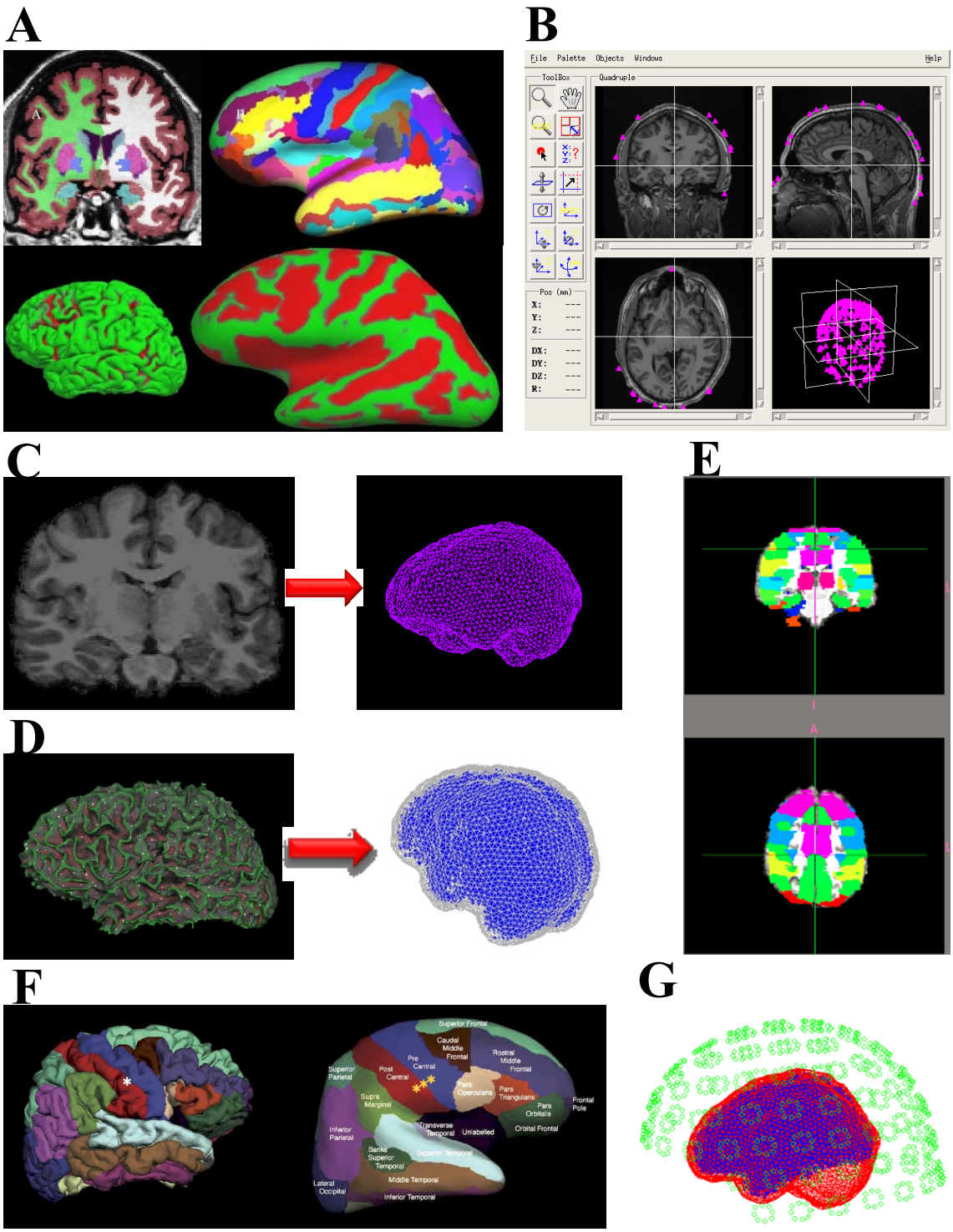

Figure 5.3: Sample images depicting EEGMEG anatomical pre-processing steps. For example, MRI anatomical reconstruction via Freesurfer (A), MEG-MRI registration via MRILAB (B), BEM mesh formation via SEGLAB (C), dipole grid definition via Freesurfer (D), ROI definition via FSL (E) or Freesurfer (F) and sensor-source space model (G) used for MEG forward model computation.

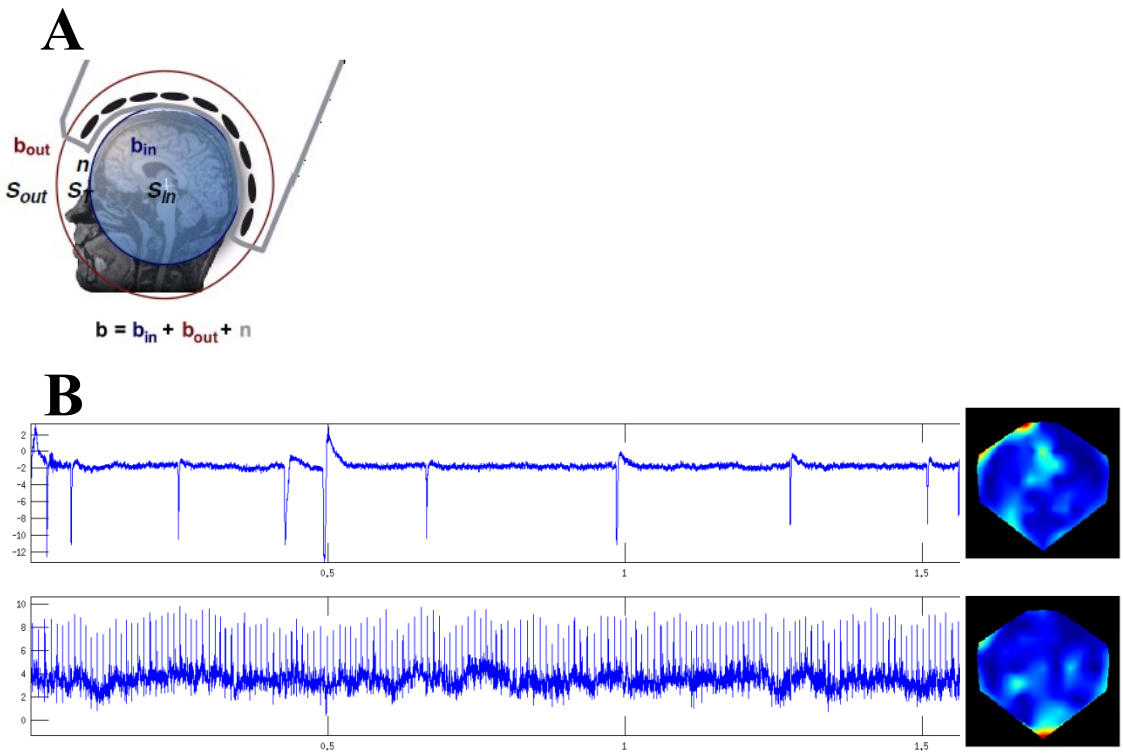

Figure 5.4: Depictions of pre-processing approaches to clean MEG data from unwanted contributions due to signals originating outside the brain (e.g. dental work, sensor array interefernce, cardiac activity, eye-blinks, etc.).
The geometry of the MaxFilter, a temporal signal separation technique, is exhibited in (A). Sample independent components (ICs) time-courses and corresponding spatial maps from a temporal ICA analysis are shown in (B) for both eye-blinks (top) and heart beats (bottom).

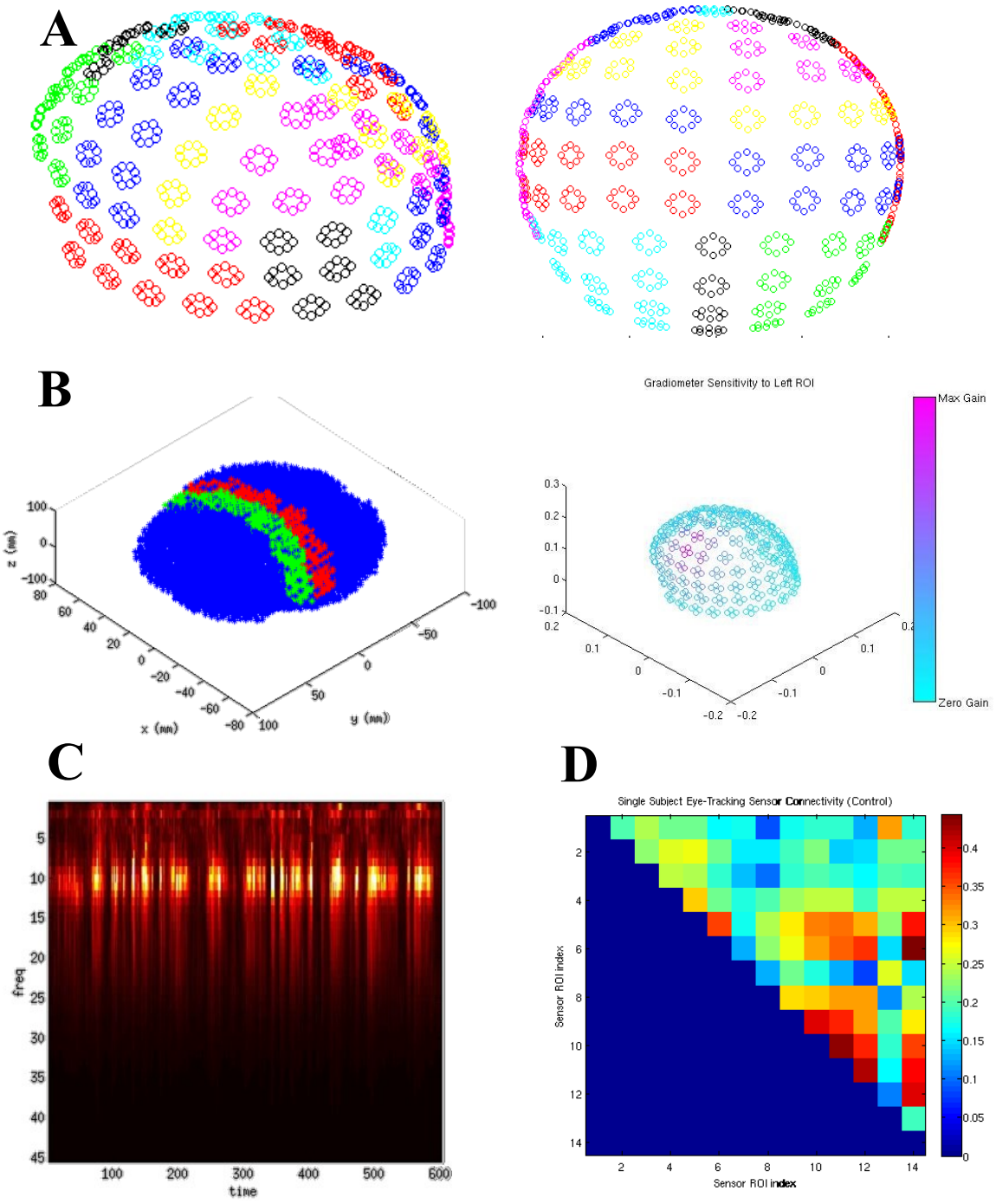

Figure 5.5: Depictions of sensor analysis processing approaches and sample results. Standard sensor analysis division of sensor groups into 14 ROIs based on general brain areas (A) or MRI-guided ROI definition (B) where the anatomical ROI data (left) and the gain matrix (B) are used to select the sensors used for analysis, are available. Analysis approaches include time-frequency analysis using Morlet wavelets (C) or ROI-to-ROI connectivity matrices (D).

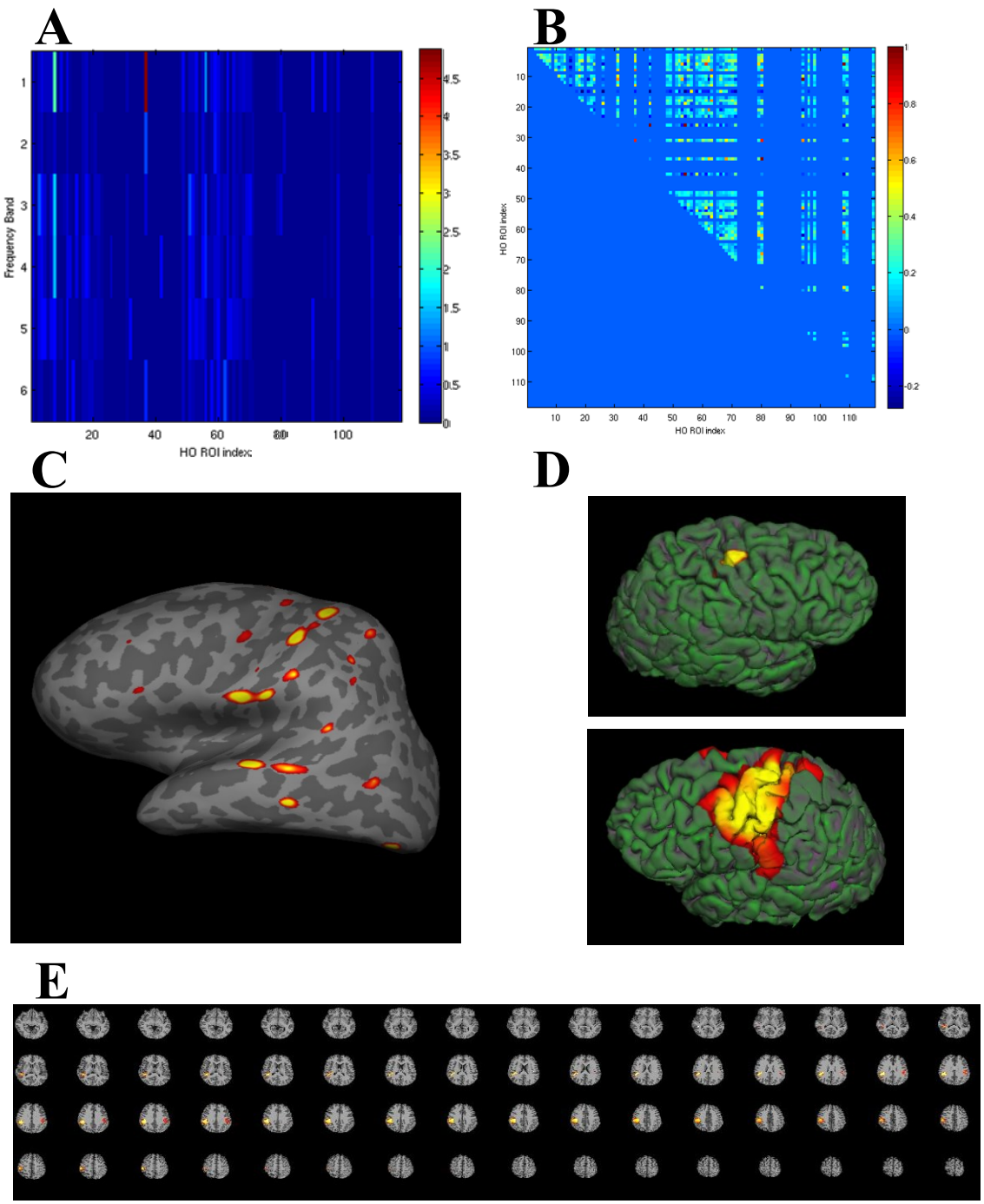

Figure 5.6: Example images of several of the available source analysis processing results which EEGMEG can generate.
Such pictures include but not limited to whole-brain ROI amplitude measures (A), whole-brain ROI-to-ROI connectivity matrices (B), RMS amplitude 3D brain maps (C), ROI seed-based functional connectivity maps (D – top: seed, bottom: homologous cortex connectivity) and IC networks derived from spatial/temporal ICA (E).

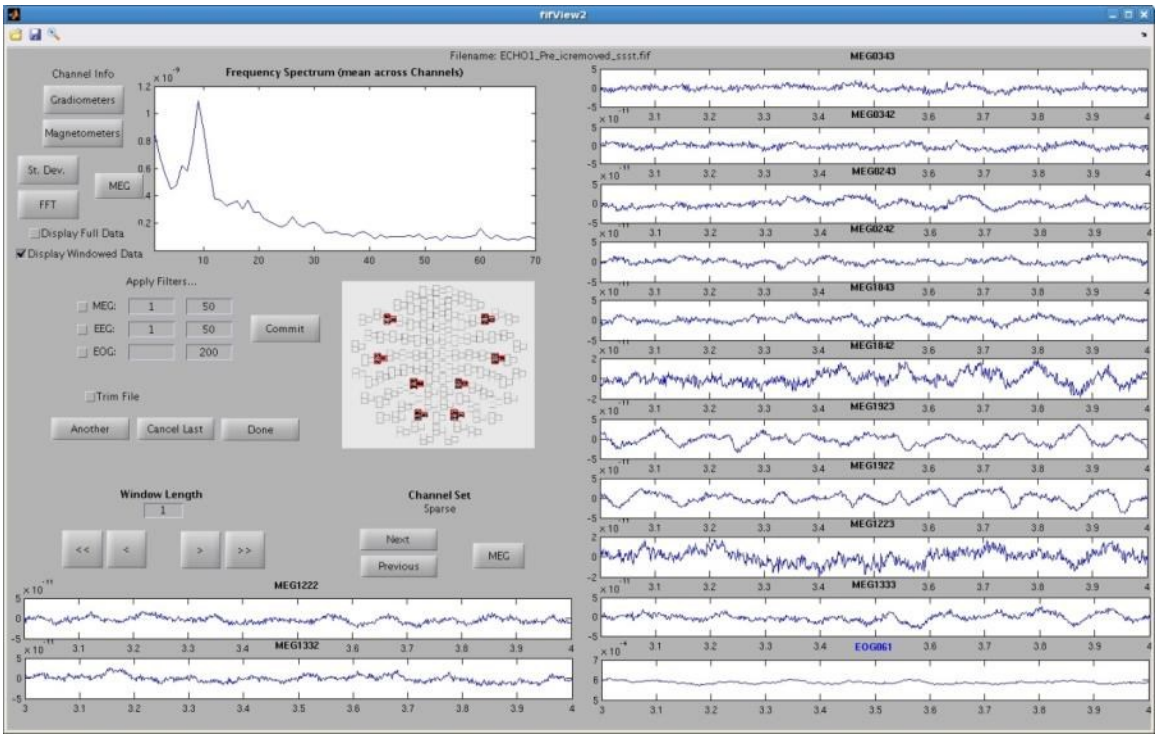

Figure 5.7: Screenshot of fifView, an GUI independent of EEGMEG, which offers the user simple means to visually review recorded electromagnetic sensor data. GUI can inspect both EEG and MEG waveforms (Neuromag format files). User can adjust the size of the window length being viewed and scroll (small and large steps) through time (bottom left). User can also scroll through channels (map above indicating channels being shown) and toggle between modalities using the MEG/EEG button (bottom right). User can filter (either low-pass or band-pass) data and/or trim data (by selecting endpoints of section to be removed). All changes can be made permanent by saving the modified file. Waveforms for all channels (gradiometers/magnetometers) as well as statistics (channel standard deviation, frequency spectrum) can be displayed for all data or just the windowed segment.

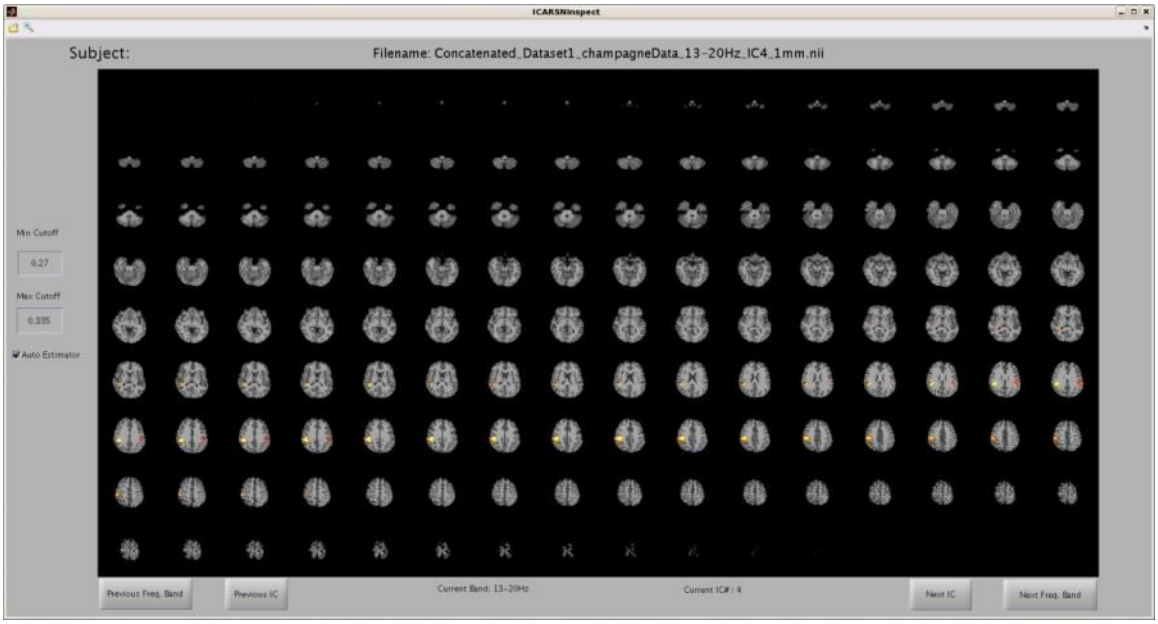

Figure 5.8: Screenshot of the EEGMEG GUI used to inspect the spatial maps for each IC obtained from the ICA analysis (spatial or temporal).
The user may sift through the various computed IC's for each of the frequency bands via simple toggle buttons (bottom of screen). Images can be manually thresholded (color scale endpoints) by entering the desired values (left of screen) or automatically by checking the Auto Estimator option (via statistical distribution estimation).

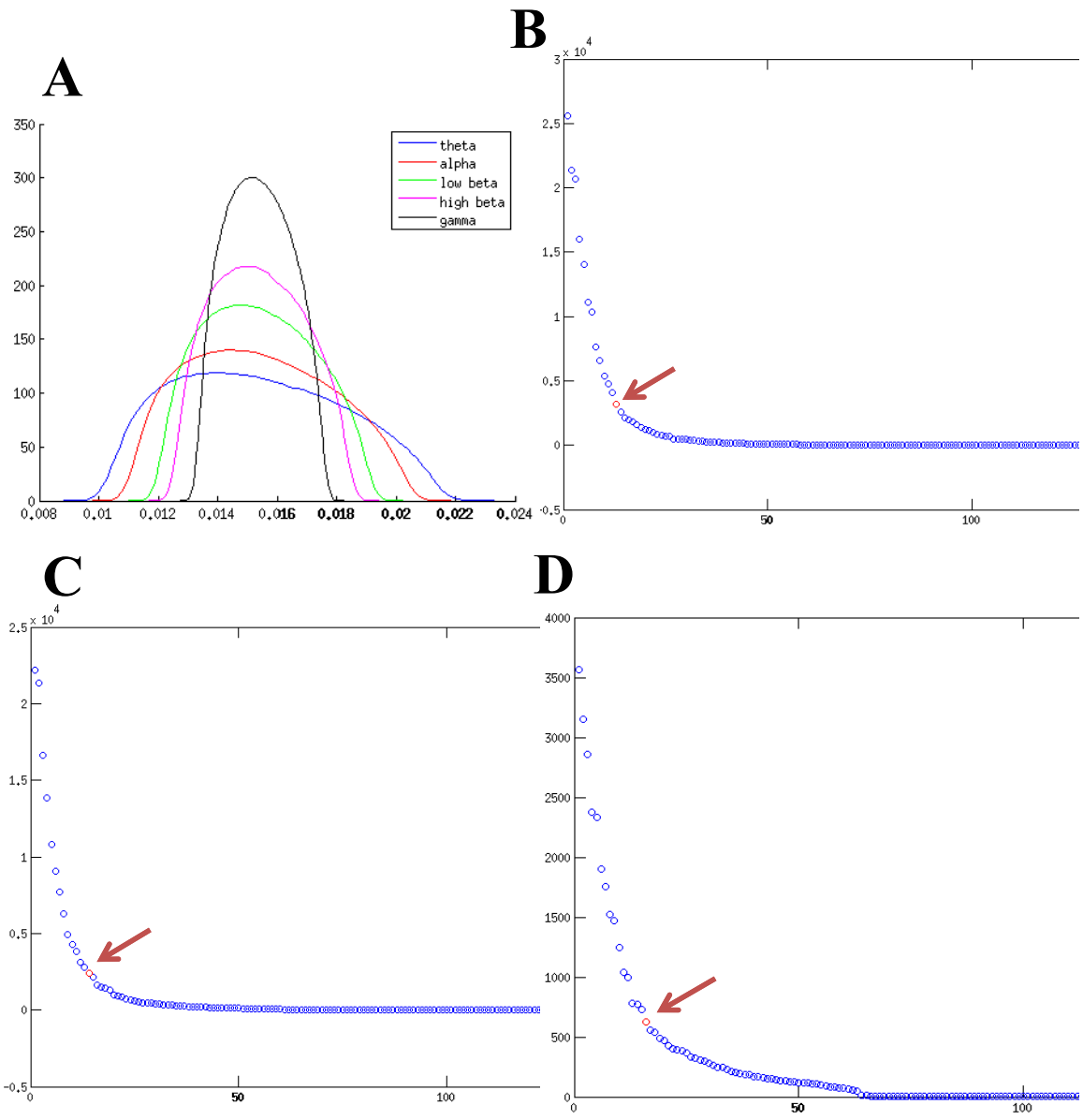

Figure 5.9: EEGMEG's eigenvalue distributions computed from randomly distributed noise for the different frequency bands (A) and corresponding examples of the regularization (cut-off) point selected by the automated algorithm (B-D).

References

Acar, Z.A., Makeig, S., 2010. Neuroelectromagnetic forward head modeling toolbox. J Neurosci Methods 190, 258-270.

Behzadi, Y., Restom, K., Liau, J., Liu, T.T., 2007. A component based noise correction method (CompCor) for BOLD and perfusion based fMRI. Neuroimage 37, 90-101.

Cox, R.W., 1996. AFNI: software for analysis and visualization of functional magnetic resonance neuroimages. Comput Biomed Res 29, 162-173.

Fischl, B., 2012. FreeSurfer. Neuroimage 62, 774-781.

Gramfort, A., Luessi, M., Larson, E., Engemann, D.A., Strohmeier, D., Brodbeck, C., Parkkonen, L., Hamalainen, M.S., 2014. MNE software for processing MEG and EEG data. Neuroimage 86, 446-460.

Huang, M.X., Dale, A.M., Song, T., Halgren, E., Harrington, D.L., Podgorny, I., Canive, J.M., Lewis, S., Lee, R.R., 2006. Vector-based spatial-temporal minimum L1-norm solution for MEG. Neuroimage 31, 1025-1037.

Huang, M.X., Mosher, J.C., Leahy, R.M., 1999. A sensor-weighted overlapping-sphere head model and exhaustive head model comparison for MEG. Phys Med Biol 44, 423-440.

Hyvarinen, A., 1999. Fast and robust fixed-point algorithms for independent component analysis. IEEE Trans Neural Netw 10, 626-634.

Mosher, J.C., Leahy, R.M., Lewis, P.S., 1999. EEG and MEG: forward solutions for inverse methods. IEEE Trans Biomed Eng 46, 245-259.

Owen, J.P., Wipf, D.P., Attias, H.T., Sekihara, K., Nagarajan, S.S., 2012. Performance evaluation of the Champagne source reconstruction algorithm on simulated and real M/EEG data. Neuroimage 60, 305-323.

Robinson, S., Vrba, J., 1998. Functional neuroimaging by synthetic aperture magnetometry. Tohoku Univ. Press, Sendai.

Sekihara, K., Nagarajan, S.S., 2008. Adaptive Spatial Filters for Electormagnetic Brain Imaging. SpringerLink, Berlin.

Smith, S.M., Jenkinson, M., Woolrich, M.W., Beckmann, C.F., Behrens, T.E., Johansen-Berg, H., Bannister, P.R., De Luca, M., Drobnjak, I., Flitney, D.E., Niazy, R.K., Saunders, J., Vickers, J., Zhang, Y., De Stefano, N., Brady, J.M., Matthews, P.M., 2004. Advances in functional and structural MR image analysis and implementation as FSL. Neuroimage 23 Suppl 1, S208-219.

Taulu, S., Kajola, M., Simola, J., 2004. Suppression of interference and artifacts by the Signal Space Separation Method. Brain Topogr 16, 269-275.

Taulu, S., Simola, J., 2006. Spatiotemporal signal space separation method for rejecting nearby interference in MEG measurements. Phys Med Biol 51, 1759-1768.

Van Drongelen, W., Yuchtman, M., Van Veen, B.D., Van Huffelen, A.C., 1996. A spatial filtering technique to detect and localize multiple sources in the brain. Brain Topogr 9, 39-49.

Van Veen, B.D., van Drongelen, W., Yuchtman, M., Suzuki, A., 1997. Localization of brain electrical activity via linearly constrained minimum variance spatial filtering. IEEE Trans Biomed Eng 44, 867-880.

Wipf, D.P., Owen, J.P., Attias, H.T., Sekihara, K., Nagarajan, S.S., 2010. Robust Bayesian estimation of the location, orientation, and time course of multiple correlated neural sources using MEG. Neuroimage 49, 641-655.

CONCLUSIONS

Resting-state fMRI studies are now routinely used to advance our knowledge of the brain's behavioral states and development, cognitive performance and intelligence, as well as its pathology. However, due to the fMRI signal's complex hemodynamic nature, it can provide only an indirect measure of neural activity, and thus interpretation of the observed BOLD signal remains a challenge, especially for experimental conditions without an explicit task. In this work, we validated the neural basis of previous fMRI resting-state findings by probing the corresponding neuromagentic signatures recorded via MEG. In addition, we advanced existing MEG source-space projection techniques to help improve their applicability for conducting complex brain analyses.

In chapter 1 (Tal et al., 2013), we employed source-based MEG (specifically the *single beamformer*) in conjunction with fMRI to further examine the origin of caffeine induced changes in BOLD connectivity observed in previous research by our lab (Rack-Gomer et al., 2009). We observed significant ($p < 0.01$) global reductions in both the MEG and fMRI connectivity measures, indicating that the observed BOLD connectivity changes predominantly resulted from decreases in the connectivity of the underlying neuro-electromagnetic fluctuations (similarities were found for both wideband and band-limited MEG data). Demonstrating the correspondence between the MEG and fMRI findings helped provide firmer evidence for the neural basis of resting-state fMRI observations and its use as a tool for the evaluation of functional connectivity at the neural level. In addition, our study strengthened the case (Brookes et al., 2011a; Brookes et al., 2011b; Hall et al., 2013; Hillebrand et al., 2012; Hipp et al., 2012; Luckhoo et al.,

2012; Mantini et al., 2011) for utilizing source-space MEG measures for characterization of resting-state connectivity.

Concerns regarding the ability of currently available beamformer approaches to correctly reconstruct source amplitudes and time-courses in the presence of correlated sources (Brookes et al., 2007; Dalal et al., 2006; Diwakar et al., 2011a; Hui and Leahy, 2006; Hui et al., 2010; Moiseev et al., 2011; Quraan and Cheyne, 2010; Sekihara et al., 2002), a phenomenon believed to be present during spontaneous and non-averaged task-related brain activity (Singer, 1999), led to the development of an improved version presented in chapter 2 (Diwakar et al., 2011b). After describing the novel mathematical additions, the *multi-core beamformer* (MCBF) insensitivity to correlation was tested with multiple simulations as well as with real data (human auditory task), successfully showing in both cases accurate source localization, amplitude recovery, time-course reconstruction and connectivity estimation. It was shown that the MCBF spatial filter can properly reconstruct source spatio-temporal behavior, thus providing a viable method for exploring complex neuronal networks and their communications (e.g. RSNs), and promoting the use of MEG to investigate such brain activity.

However, as the proposed approach was dependent on the location of the sources of interest to be already known, an ideal yet generally unavailable scenario in resting-state conditions, we introduced in Chapter 3 an iterative algorithm to be integrated with the MCBF mathematical framework enabling source localization without any *a priori* information. Performance was validated by means of complex simulations (containing waveforms designed to resemble spontaneous MEG signals) as well as real neuromagnetic measurements (evoked median nerve stimulation), and MCBF

reconstructions were compared with those of the SBF. As expected, MCBF reconstructions were insensitive to underlying source correlations. MCBF source localization maps and time-course reconstructions were found to be a major improvement over their SBF counterparts. Furthermore, combining MCBF together with the iterative approach resulted in substantial minimization of the signal leakage artifacts and solution bias towards the center of the brain that occur with the SBF. The proposed MCBF solution ultimately provided voxel-by-voxel source activity estimates thereby enabling whole-brain functional connectivity analyses of MEG evoked and spontaneous data (allowing the characterization of MEG resting-state networks).

Lastly, in Chapter 4 we applied the MCBF approach to the experimental results from Chapter 1 to compare its performance with the SBF. We found that from a global perspective both techniques indicate a similar reduction in connectivity. However, we note that significant individual (i.e. for a given ROI pair) changes in connectivity were slightly reduced for MCBF (potentially reflecting less signal leakage), suggesting that SBF measures should be treated cautiously when interpreting the significance of local changes. Preliminary research into resting-state network characterization using temporal ICA was also conducted. Initial observations indicate better spatial definition for the MCBF RSN maps when compared with the SBF maps, but further work is needed to demonstrate the potential advantages of the MCBF approach over SBF for studies of resting-state networks.

References

Brookes, M.J., Hale, J.R., Zumer, J.M., Stevenson, C.M., Francis, S.T., Barnes, G.R., Owen, J.P., Morris, P.G., Nagarajan, S.S., 2011a. Measuring functional connectivity using MEG: methodology and comparison with fcMRI. Neuroimage 56, 1082-1104.

Brookes, M.J., Stevenson, C.M., Barnes, G.R., Hillebrand, A., Simpson, M.I., Francis, S.T., Morris, P.G., 2007. Beamformer reconstruction of correlated sources using a modified source model. Neuroimage 34, 1454-1465.

Brookes, M.J., Woolrich, M., Luckhoo, H., Price, D., Hale, J.R., Stephenson, M.C., Barnes, G.R., Smith, S.M., Morris, P.G., 2011b. Investigating the electrophysiological basis of resting state networks using magnetoencephalography. Proc Natl Acad Sci U S A 108, 16783-16788.

Dalal, S.S., Sekihara, K., Nagarajan, S.S., 2006. Modified beamformers for coherent source region suppression. IEEE Trans Biomed Eng 53, 1357-1363.

Diwakar, M., Huang, M.X., Srinivasan, R., Harrington, D.L., Robb, A., Angeles, A., Muzzatti, L., Pakdaman, R., Song, T., Theilmann, R.J., Lee, R.R., 2011a. Dual-Core Beamformer for obtaining highly correlated neuronal networks in MEG. Neuroimage 54, 253-263.

Diwakar, M., Tal, O., Liu, T.T., Harrington, D.L., Srinivasan, R., Muzzatti, L., Song, T., Theilmann, R.J., Lee, R.R., Huang, M.X., 2011b. Accurate reconstruction of temporal correlation for neuronal sources using the enhanced dual-core MEG beamformer. Neuroimage 56, 1918-1928.

Hall, E.L., Woolrich, M.W., Thomaz, C.E., Morris, P.G., Brookes, M.J., 2013. Using variance information in magnetoencephalography measures of functional connectivity. Neuroimage 67, 203-212.

Hillebrand, A., Barnes, G.R., Bosboom, J.L., Berendse, H.W., Stam, C.J., 2012. Frequency-dependent functional connectivity within resting-state networks: an atlas-based MEG beamformer solution. Neuroimage 59, 3909-3921.

Hipp, J.F., Hawellek, D.J., Corbetta, M., Siegel, M., Engel, A.K., 2012. Large-scale cortical correlation structure of spontaneous oscillatory activity. Nat Neurosci 15, 884-890.

Hui, H.B., Leahy, R.M., 2006. Linearly constrained MEG beamformers for MVAR modeling of cortical interactions. 3rd IEEE International Symposium on Biomedical Imaging: Nano to Macro, pp. 237–240.

Hui, H.B., Pantazis, D., Bressler, S.L., Leahy, R.M., 2010. Identifying true cortical interactions in MEG using the nulling beamformer. Neuroimage 49, 3161-3174.

Luckhoo, H., Hale, J.R., Stokes, M.G., Nobre, A.C., Morris, P.G., Brookes, M.J., Woolrich, M.W., 2012. Inferring task-related networks using independent component analysis in magnetoencephalography. Neuroimage 62, 530-541.

Mantini, D., Della Penna, S., Marzetti, L., de Pasquale, F., Pizzella, V., Corbetta, M., Romani, G.L., 2011. A signal-processing pipeline for magnetoencephalography resting-state networks. Brain Connect 1, 49-59.

Moiseev, A., Gaspar, J.M., Schneider, J.A., Herdman, A.T., 2011. Application of multi-source minimum variance beamformers for reconstruction of correlated neural activity. Neuroimage 58, 481-496.

Quraan, M.A., Cheyne, D., 2010. Reconstruction of correlated brain activity with adaptive spatial filters in MEG. Neuroimage 49, 2387-2400.

Rack-Gomer, A.L., Liau, J., Liu, T.T., 2009. Caffeine reduces resting-state BOLD functional connectivity in the motor cortex. Neuroimage 46, 56-63.

Sekihara, K., Nagarajan, S.S., Poeppel, D., Marantz, A., 2002. Performance of an MEG adaptive-beamformer technique in the presence of correlated neural activities: effects on signal intensity and time-course estimates. IEEE Trans Biomed Eng 49, 1534-1546.

Singer, W., 1999. Neuronal synchrony: a versatile code for the definition of relations? Neuron 24, 49-65, 111-125.

Tal, O., Diwakar, M., Wong, C.W., Olafsson, V., Lee, R., Huang, M.X., Liu, T.T., 2013. Caffeine-Induced Global Reductions in Resting-State BOLD Connectivity Reflect Widespread Decreases in MEG Connectivity. Front Hum Neurosci 7, 63.